Modelling and design of an eddy current coupling for slip-synchronous permanent magnet wind generators

by
Zac Mouton

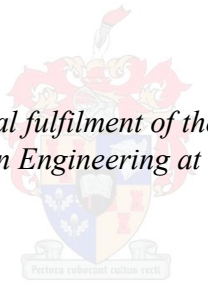

Thesis presented in partial fulfilment of the requirements for the degree Master of Science in Engineering at Stellenbosch University

Supervisor: Prof M J Kamper
Department of Electrical & Electronic Engineering

March 2013

Declaration

By submitting this thesis electronically, I declare that the work contained therein is my own, original work, that I am the sole author thereof (save to the extent clearly otherwise stated), that reproduction and publication thereof by Stellenbosch University will not infringe any third party rights and that I have not previously in its entirety or in part submitted it for obtaining any qualification

Date: March 2013

Summary

Slip-synchronous permanent magnet generators (SS-PMG) is a recently proposed direct-grid connected direct-drive generator topology for wind power applications. It combines a permanent magnet synchronous generator and a slip permanent magnet generator through a common permanent magnet rotor. In this study the possibility of using an eddy current coupling as the slip permanent magnet generator is investigated. The eddy current coupling has the attractive advantage of completely removing cogging and load torque ripple, which are known problems in the SS-PMG. However, the analytical modelling of the eddy current coupling is complex. Three different topologies are considered for the eddy current coupling.

A finite element model is presented for the eddy current coupling. It is shown that 2D finite element methods are inaccurate compared to 3D finite element methods when solving eddy currents in eddy current couplings. In order to test the accuracy of the finite element modelling of a large eddy current coupling a prototype slip rotor is designed to operate with an existing permanent magnet rotor. Two topologies are optimally designed and compared for the slip rotor, using 3D finite element transient simulations. One of the designed topologies is used for the construction of the prototype slip rotor. The manufactured eddy current coupling allows for comparison between the 3D finite element simulations and measured results, which shows an excellent correlation.

Based on observations of the 3D finite element simulations an analytical approximation of the eddy current coupling is proposed for low slip frequencies. It is shown that the analytical model is very dependent on the accurate modelling of the eddy current paths in the slip rotor, something that is difficult to determine accurately. An approximation is made, again based on 3D finite element simulations, which allows the accurate modelling of the current paths for different axial lengths. The analytical model is used for rapid design optimisation of both the slip rotor and permanent magnet rotor of the eddy current coupling, for two different eddy current coupling topologies. The optimised eddy current coupling design with the best results is compared to existing slip permanent magnet generator technologies.

The eddy current coupling is shown to have the potential to be a feasible alternative to existing slip permanent magnet generator topologies for application in slip-synchronous permanent magnet generators. It has excellent torque versus slip behaviour, and no cogging or load torque ripple. However, the manufacturing and assembly process of the proposed slip rotor has to be improved for the eddy current coupling to be a realistic competitor to the existing slip permanent magnet generator technologies.

Opsomming

Die glip-sinkroon permanente magneet generator is 'n direk-aangedrewe wind generator wat direk aan die krag netwerk gekoppel kan word. Dit kombineer 'n permanente magneet sinkroon generator en 'n permanente magneet glip generator deur middel van 'n gemeenskaplike permanente magneet rotor. In hierdie studie word die moontlike gebruik van 'n werwelstroom skakel as plaasvervanger vir die permanente magneet glip generator ondersoek. Die werwelstroom skakel het geen vertandings of las draaimoment rimpeling nie, wat bekende probleme vir die glip-sinkroon permanente magneet generator is. Die analitiese modellering van die werwelstroom skakel is egter nie eenvoudig nie. Daar word drie verskillende topologieë oorweeg vir die werwelstroom skakel.

'n Eindige element model word ontwikkel vir die werwelstroom skakel. Dit word bevind dat 2D eindige element analise onvoldoende is vir die berekening van werwelstrome in die werwelstroom skakel, en gevolglik word 3D eindige element modelle gebruik in hierdie studie. Om die akkuraatheid van die eindige element model te beproef word 'n prototipe glip rotor optimaal ontwerp deur middel van eindige element analise. Die glip rotor vorm saam met 'n bestaande permanente magneet rotor 'n werwelstroom skakel. Vir hierdie ontwerp word twee werwelstroom skakel topologieë gebruik, en met mekaar vergelyk. Die topologie wat beter presteer word gebruik vir die vervaardiging van die glip rotor. 'n Vergelyking van die gemete waardes van die vervaardigde werwelstroom skakel en die resultate van die 3D eindige element simulasies dui daarop dat die 3D eindige element modellering 'n baie goeie voorspelling van die werklikheid is.

'n Analitiese model vir die werwelstroom skakel onder lae glip toestande is ontwikkel deur gebruik te maak van observasies uit die 3D eindige element simulasies. Die analitiese model is baie afhangklik van die modellering van die werwelstrome se stroompaaie, iets wat moeilik is om akkuraat te bepaal. 'n Benadering word gemaak wat die akkurate modulering van die stroompaaie moontlik maak vir verskillende aksiale lengtes. Die analitiese model word dan gebruik vir vinnige optimering van die werwelstroom skakel se ontwerp vir twee verskillende werwelstroom skakel topologieë. Die geoptimeerde ontwerp wat die beste resultate toon word vergelyk met bestaande permanente magneet glip generators.

Dit word gewys dat die werwelstroom skakel die potensiaal het om 'n uitvoerbare alternatief tot die permanente magneet glip generator te wees, vir gebruik in glip-sinkroon permanente magneet generators. Die werwelstroom skakel toon baie goeie draaimoment teenoor glip gedrag, en het geen vertandings of las draaimoment rimpeling nie. Voordat die werwelstroom generator 'n realistiese kompeteerder teenoor die bestaande glip-sinkroon tegnologie is, moet daar verbeterde vervaardigings maniere gevind word vir die voorgestelde glip rotor.

Acknowledgements

There are many people whom have earned my gratitude throughout the course of this study, too many to name them all.

I would like to thank my fellow students and the technical staff of the Electrical Machines Laboratory, the staff of the Electrical Engineering Workshop, and other lecturers of the electrical engineering department. Their advice, assistance, and valuable experience contributed greatly to this project.

I especially thank Professor Maarten Kamper, my study supervisor, for his insight, guidance, support and patience. It is a great privilege to learn from him.

I also thank my family for their continued support through all the years of my education.

Above all I thank God, and give all the glory to Him. His immeasurable grace made this project possible.

List of publications

Conference Proceedings

Z. Mouton and M. J. Kamper, "Design of an Eddy-Current Coupling for Slip-Synchronous Permanent Magnet Wind Generators," *XXth International Conference on Electrical Machines (ICEM)*, Marseille, France, September 2012, pp. 631-637

Table of Contents

List of Figures

List of Tables

Nomenclature

Abbreviations

Abbreviation	Description
2D	2-dimensional
3D	3-dimensional
Cu	Copper (used to describe conductive material)
DFIG	doubly-fed induction generator
FE	finite element
Fe	Iron (used to describe steel yoke material)
IG	induction generator
MMFD	Modified Method of Feasible Directions
NdFeB	Neodymium Iron Boron (PM material)
PM	permanent magnet
PMIG	permanent magnet induction generator
PMIM	permanent magnet induction machine
PMSG	permanent magnet synchronous generator
PSO	Particle Swarm Optimisation
S-PMG	slip permanent magnet generator
SS-PMG	slip-synchronous permanent magnet generator
WTG	wind turbine generator

Symbols

Symbol	Description
A	area
B	flux density
b	ratio of the actual air gap flux density (B_{ag}) to its fundamental harmonic (B_{g1})
B_{ag}	actual air gap flux density
B_{g1}	fundamental harmonic of the actual flux density in the air gap
B_p	peak flux density
B_r	residual magnetization
C	vertical axis offset for the approximation of α_k
dx	tangential length of an element
dy	axial length of an element
e	induced voltage
F	force
f	frequency
$f(\mathbf{X})$	objective function for optimisation
g	radial length of air in the air gap (different from l_g)
$g(\mathbf{X})$	inequality constraint function
h	height dimension
H	magnetic field strength
H_c	coercive magnetic field strength
i	current
k	constant real value
K_y	axial length of current path before eddy currents start turning in tangential direction
l	axial or tangential length dimension
l_c	circumference of eddy current loop
l_g	effective radial length of the air gap
l_{ipg}	tangential length in air gap between two adjacent permanent magnets
m	gradient of the approximation for α_k
M_{cu}	total active conductor material mass
M_{pm}	total active permanent magnet material mass
M_s	total active steel mass
$m_x(\Delta)$	number of elements in tangential length Δ
$m_y(\Delta)$	number of elements in the axial length of a current path with tangential length of 2Δ
N	number of turns in a coil

n_{sync}	synchronous speed
p	number of poles
r	radius
R	resistance
r_{out}	outer radius
s	slip (pu)
T	Torque
t	time
T_1	Torque due to fundamental harmonic values
u	tangential velocity
w	weighing factor
x	tangential length
$\boldsymbol{X}$	multidimensional vector of design parameters
x_{max}	half the tangential length of a pole pitch
y	axial length
α_k	ratio of K_y to the permanent magnet axial length
α_τ	ratio of a pole pitch to the permanent magnet axial length
Δ	tangential distance between a specific current loop and the centre between two adjacent magnetic poles
δ_c	skin depth
η	efficiency
λ	flux linkage
μ_0	permeability of air
μ_r	relative permeability
ρ	material resistance
τ_p	tangential length of a pole pitch
τ_{pm}	ratio of the pole pitch to the permanent magnet pitch
ϕ	magnetic flux
ω	rotational velocity

The subscripts used with symbols refer to the following, unless stated differently.

Subscript	Description
subscript 'a'	refers to dimension inside the active axial length of the magnetic field
subscript 'cu'	refers to dimension of the conductive material of the slip rotor
subscript 'elm'	element
subscript 'g'	refers to dimension of or parameter in the air gap
subscript 'ind'	induced
subscript 'loop'	refers to value for a single current loop
subscript 'm'	refers to dimension of a permanent magnet
subscript 'pm'	refers to dimension of a permanent magnet
subscript 'pp'	per pole
subscript 're'	electrical frequency in the slip rotor
subscript 's'	refers to dimension of or parameter in the inner yoke
subscript 'tot'	total
subscript 'y'	refers to dimension of or parameter in the outer yoke

1 Introduction

1.1 Background

Over the course of the past 130 years humanity has become very dependent on electricity. It is well known that there is great demand for clean renewable energy. Wind power is the most used renewable energy source and its technologies are continuously being improved. Harnessing wind energy is expensive, particularly due to high initial capital cost and maintenance expenses. Research is widely done in search of methods to increase the efficiency and reliability of harnessing wind energy, while simultaneously decreasing the cost.

A variety of generator systems are used to convert wind energy to electricity. The most typical systems either use a gearbox between the turbine and the generator, or a frequency converter between the generator and the grid, or both [**1**]. An example of a system using a gearbox and direct-online generator is a fixed speed system using a standard robust squirrel cage induction generator (IG), as shown in Fig. 1.1. In Fig. 1.2 the permanent magnet synchronous generator (PMSG) is shown as an example of a generator topology used in a variable speed system without a gearbox but with a full-scale power electronic converter. The doubly fed induction generator (DFIG) is a generator used in a variable speed system where both a gearbox and partial-scale power electronic converter is necessary, as shown in Fig. 1.3.

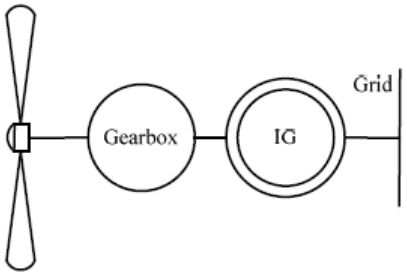

Fig. 1.1 Gearbox and direct-online drive train layout for an IG.

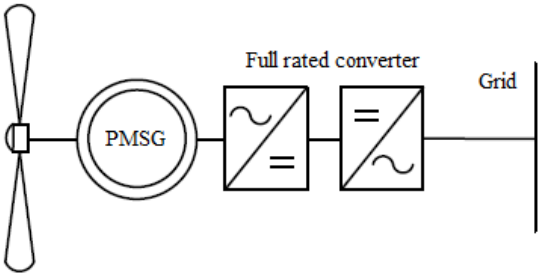

Fig. 1.2 Direct-drive and full rated converter drive train layout for a PMSG.

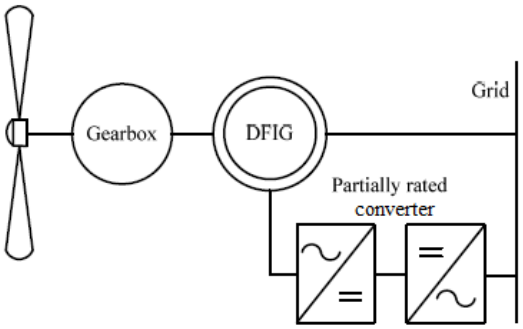

Fig. 1.3 Gearbox and partial rated converter drive train layout for a DFIG.

1.1.1 Permanent magnet induction generators

One of the innovative generator topologies designed for use in wind turbine generators (WTG) is a permanent magnet induction generator (PMIG). The PMIG utilises a free-rotating permanent magnet (PM) rotor in addition to the conventional stator and rotor of an induction machine [**2**]. An example of

a typical PMIG topology is shown in Fig. 1.4, though other topologies with the PM rotor on the outside of the stator or inside the rotor are also possible [**3**].

The PM rotor provides additional flux in the air gap, which reduces the magnetising current and thus the reactive power demand of the machine [**3**]. Therefore the PMIG has an improved power factor in comparison to conventional IG's [**4**]. The effect may be modelled in its electrical circuit as an additional voltage source in series with the magnetising reactance, as shown in Fig. 1.5. The electrical circuit of the PMIG is analysed, amongst others, in [**5**]. The lower reactive power requirements allows for a larger diameter machine with a higher number of poles [**6**], which enables the PMIG to be used as a direct-drive generator and removes the need for a gearbox. The asynchronous operation of the PMIG allows for a soft grid connection, which removes the need for a frequency converter. In removing the gearbox and the frequency converter some significant reliability and cost issues with wind turbine generators (WTG) are addressed [**7**]. The PMIG can therefore be a direct-drive, direct-online system.

While the complexity and cost of the drive train of the WTG is reduced, the PMIG itself is a complex generator. The fact that there are no examples of installed and tested wind generators of this type in practice is likely due to the difficult construction of the PMIG [**8**]. Cogging torque can also be a significant problem in the PMIG, since it influences the start-up of the PMIG and the stability of the free-rotating PM rotor [**9**]. The most significant disadvantage of the PMIG throughout literature remains its constructional complexity [**2**] [**3**] [**6**] [**9**].

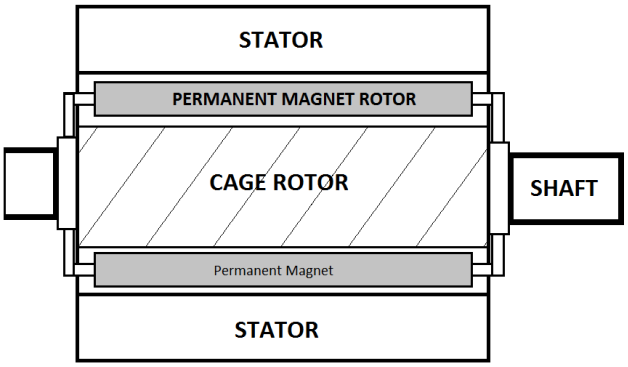

Fig. 1.4 Typical topology of a PMIG.

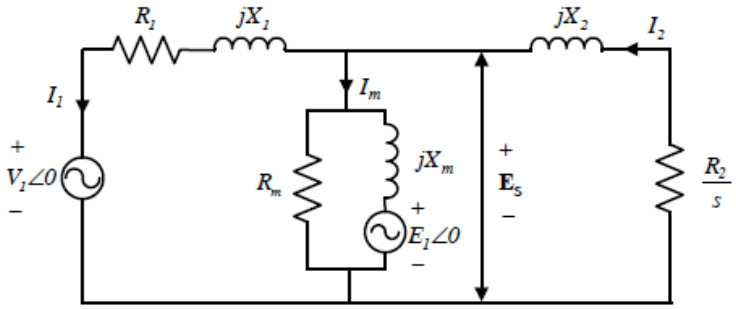

Fig. 1.5 Equivalent circuit of a PMIG .

1.1.2 Slip-synchronous permanent magnet generators

In [**9**] a new concept direct-drive direct-online generator is developed based on the PMIG, namely the slip-synchronous permanent magnet generator (SS-PMG) [**8**]. The SS-PMG alleviates many of the constructional issues associated with PMIG's.

The SS-PMG consists of two magnetically decoupled PM machines, as shown in Fig. 1.6. The one machine consists of the grid-connected stator with the free rotating PM rotor operating at synchronous speed in relation to the stator's rotating field, like a normal PMSG. The second machine consists of the short-circuited slip rotor operating at slip speed relative to the common PM rotor, creating the slip permanent magnet generator (S-PMG). The slip-rotor is mechanically connected directly to the wind turbine. Therefore power transfer in the SS-PMG type WTG takes place from the turbine to the slip-rotor and then via the PM rotor to the stator and the grid [**10**]. Like the PMIG, the SS-PMG does not need a gearbox or power electronic converter.

There are significant advantages to magnetically separating the synchronous and asynchronous operation of the system. The number of poles and size of the two machine units can differ, which means that each machine can be optimally designed independently from the other. This allows for certain design aspects that can reduce cogging torque and torque ripple in the system, such as using non-overlap windings in both machine units [**8**]. A disadvantage, particularly in WTG's, is that the SS-PMG is heavier than the conventional PMIG.

In [**11**] it is shown that the SS-PMG can make a direct grid connection in a stable automated manner throughout the usable wind range, and offers grid voltage support. A transient model was developed for the SS-PMG in [**10**]. It is shown that the SS-PMG handles transient turbine torque well, in that no voltage flickering occurs due to, for example, tower shadow or yaw error. Similarly to the PMIG, torque quality in the SS-PMG is very important, especially on the low frequency IG-side. Torque ripples, particularly of low frequency and high amplitude, carried through the free-rotating PM rotor will influence the quality of the electrical power generated. No cogging torque and no load torque ripple is desired to ensure sustained internal stability [**8**] [**12**].

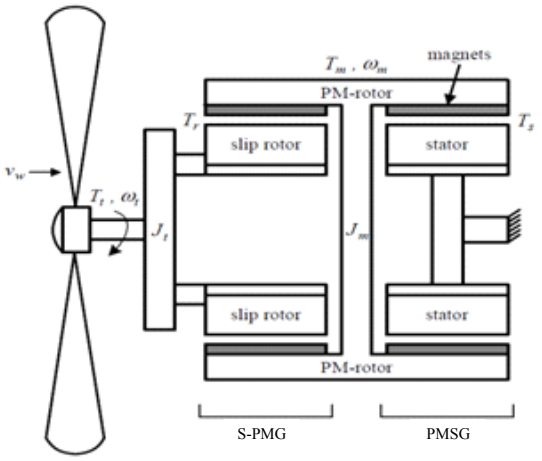

Fig. 1.6 Concept diagram of the SS-PMG [**10**].

1.1.3 Eddy current couplings

Eddy current couplings is an old concept. For decades it has been successfully implemented in industry for use in variable speed drives, electronic clutches, fluid control in power drives, and to mechanically isolate a motor from its load [**13**] [**14**]. It is also used as an eddy current brake [**15**] [**16**]. In this study it is proposed to use the eddy current coupling as the S-PMG in Fig. 1.6.

An eddy current coupling consists of a loss drum and a field member. It operates on the same principles as an induction machine. The field member provides the magnetic flux, either using PMs or an electrically induced magnetic field. The loss drum rotates relative to the magnetic field, inducing eddy currents in the loss drum. The magnitude of the induced eddy currents depends on machine

constants and the frequency of the magnetic field relative to the drum, as explained in [**15**]. Through action and reaction of the magnets and induced poles the same torque is common to both components, and power is transferred from the one to the other.

The eddy current coupling concept is a fairly simple design, but there are serious challenges to accurately modelling its behaviour. In nearly all eddy current couplings the loss drum consists of only a featureless ferromagnetic cylinder. The eddy currents are induced in the ferromagnetic material, which makes the current density distribution difficult to determine analytically, since iron saturation has to be taken into account [**17**]. In the literature of eddy current coupling modelling Maxwell's' laws are usually used along with the diffusion equation. This leads to complex analytical models which are usually simplified with assumptions [**15**] [**17**] [**18**] [**19**]. One common assumption is that the eddy currents flow purely in an axial direction, which is very unlikely [**15**] [**18**].

1.1.4 Torque ripple

Torque quality is a very important consideration during direct-drive permanent magnet generator design, and thus also for the SS-PMG design of Fig. 1.6. Torque ripple generates unwanted noise and vibrations, and high cogging torque can prevent start-up due to low torque generation at low turbine speeds [**12**]. The torque ripple is mainly generated by the slotted stator and by the placing of windings and permanent magnets [**20**]. Under no-load conditions the slotted air gap and permanent magnets produce cogging torque due to the variation of the magnetic permeance.

There are many techniques to reduce cogging torque and torque ripple, both through the physical design of the machine and through some control techniques. Physical techniques such as discussed in [**21**], [**22**] and [**23**] increase machine complexity and manufacturing cost. Similarly control methods such as discussed in [**24**], [**25**] and [**26**] often require accurate knowledge of the torque characteristics and accurate measuring methods that also increases cost.

1.2 Purpose of this study

In [**27**] three machines with different winding configurations and two brushless DC topologies are evaluated as S-PMG units for a 15 kW SS-PMG. An alternative is the use of an eddy current coupling as S-PMG, since the eddy current coupling also operates on the same induction and slip principles as the slip permanent magnet generator. However, due to the different topology a different modelling and design approach is followed from [**27**]. The purpose of this study is the modelling, design and evaluation of an eddy current coupling for use as an S-PMG.

1.2.1 Proposed eddy current coupling as S-PMG

The attractive advantages of the eddy current coupling topology is its simple functioning and that there is no cogging or load torque ripple. Therefore use of the expensive and complex torque minimisation methods of section 1.1.4 can be avoided. However, to meet the high torque requirements of an S-PMG at a sensible efficiency, it is necessary to use a good conductor for the eddy currents. The use of a conventional purely ferromagnetic loss drum is insufficient. Therefore a featureless and solid conductive ring is to be used as part of the loss drum of the eddy current coupling. By featureless it is meant that the conductive ring is to have no coils, slots or bars, or any physical feature other than a uniformly smooth surface.

A typical topology of the suggested solution is shown in Fig. 1.7, though different topologies are considered. On the outside is the field member and on the inside is the loss drum consisting of a conductive, non-ferromagnetic material and a second yoke. The eddy current coupling loss drum serves as slip rotor in the S-PMG, and the field member is the PM rotor. The vast majority of eddy

currents will be induced in the low resistance conductive ring of the slip rotor. The second ferromagnetic yoke serves as the magnetic flux return path. Depending on the topology of the eddy current coupling used in the S-PMG it may also be considered as an air-cored machine, with the same advantages [**28**]. However, throughout this project it is referred to as an eddy current coupling.

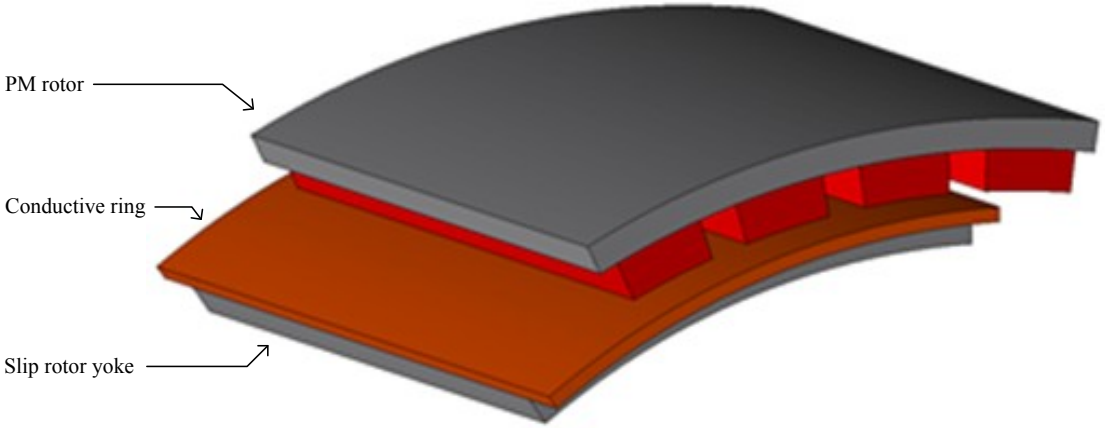

Fig. 1.7 Typical topology of the eddy current coupling for the SS-PMG.

1.2.2 Design specifications

For a fair comparison to the machines evaluated in [**27**] the same design specifications are to be used. In [**27**] the S-PMGs are designed for minimum mass, subject to the constraints in Table 1.1. Since there is no torque ripple in an eddy current coupling, it is not considered during the design. The eddy current coupling is designed for use in a 15 kW SS-PMG, in which it has to provide 1000 Nm torque at the rated slip of 3%. The 3% rated slip corresponds to the specified high efficiency of 97%, since efficiency for an eddy current coupling is calculated as [**15**] [**27**]

$$\eta = 1 - s \ . \tag{1.1}$$

The outside diameter of the eddy current coupling is to remain as specified in Table 1.1, to enable it to be connected to the existing 15 kW PMSG.

Different pole numbers are considered for the eddy current coupling, without changing the PMSG side of the PM rotor. Therefore the synchronous speed of the PMSG remains the same, which means the mechanical speed of the eddy current coupling side of the PM rotor remains the same. Thus the S-PMG synchronous speed, n_{sync}, is independent of the number of poles on the PM rotor. Since the rated slip also remains the same, only the electrical frequency of the induced currents varies with pole number. This is shown by

$$\omega_{re} = 2\pi \frac{psn_{sync}}{120} \ , \tag{1.2}$$

where ω_{re} is the electrical frequency of the induced currents on the slip rotor, p is the number of poles and s is the slip.

Parameter	Value
Rated torque (Nm)	1000
Rated efficiency (%)	97
Rated slip (%)	3
Breakdown torque (pu)	≥ 2.0
No load torque ripple (%)	≤ 2.5
Full load torque ripple (%)	≤ 4.0
Synchronous speed (rpm)	150
Electrical output power (kW)	15
Outside diameter (mm)	653.5

Table 1.1 Design constraints of the S-PMG.

1.2.3 Approach to determining the analytical model

The design of the eddy current coupling is to be optimised, and an optimisation algorithm needs to use a model of the eddy current coupling. There are three possible approaches to determining such a model.

The first is to use finite element (FE) solutions in conjunction with the optimisation algorithm. In this approach the FE model is modified based on output from the optimisation algorithm. The FE model is solved and the results returned to the optimisation algorithm, which then uses the results to determine new values for the design variables. The process is repeated until the optimal values have been determined. The major drawback of this approach is the computational intensity and time consumption a large number of FE solutions require.

The second possible approach is to use an analytical model based on Maxwell's laws. Accurately determining such a model is extremely complex due to the current distribution being unknown, the varying permeabilities of the materials in the eddy current coupling, and the 3D behaviour that has to be modelled [**15**] [**18**] [**29**]. There are a few examples in literature of 3D analytical models for eddy currents couplings, however dubious assumptions are made regarding the behaviour of the eddy currents [**15**] [**18**].

The third possible approach is to determine an accurate analytical model based on common electrical laws, such as those of Faraday and Ohm. The challenge with this approach is that there are no specifically defined current paths, due to the featureless conductive material of the slip rotor. However, through observations made using modern 3D FE simulation technology, a model for the current path can be developed.

Using an analytical model during optimisation is significantly faster than using a 3D FE model for optimisation iterations. The second approach, using already complex 3D mathematical modelling, is further complicated by the addition of the conductive ring. In this study the third approach is followed, due to it being faster than the first approach and simpler than the second approach.

1.3 Thesis layout

The SS-PMG with its associated advantages and challenges has been discussed. The proposal is to investigate the feasibility of using an eddy current coupling as a possible alternative to existing S-PMG technologies. To that end the eddy current coupling has to be modelled and designed. Three

different topologies for the eddy current coupling are considered through the course of this study. The different topologies are introduced in chapter 2.

For the modelling and design of an eddy current coupling, FE simulation is necessary. In chapter 3 the 2D and 3D FE modelling and solving of an eddy current coupling is investigated using an existing small prototype eddy current coupling.

In chapter 4 a 15 kW prototype eddy current coupling slip rotor is designed using 3D FE, manufactured and tested. As a preliminary investigation of the eddy current coupling concept it shows the accuracy of the 3D FE modelling for a large machine.

3D FE simulations are used in chapters 5 and 6 for the development of the analytical model of the eddy current coupling. In chapter 7 the analytical model is used for the optimal design of eddy current couplings of two topologies and a variety of pole numbers.

2 Considered topologies

Throughout this project three topologies are considered for the eddy current coupling. The purpose of this chapter is to describe and compare the three topologies before the performance analysis of the topologies is done.

2.1 First topology

The first topology is a double sided PM rotor topology with magnets on only one side, as shown in Fig. 2.1. It has two air gaps, one on each side of the conductive material. The second yoke is placed on the inside of the inside air gap to complete the path of the magnetic flux, as shown in Fig. 2.2. It is mechanically connected in the axial direction to the base plate of the PM rotor. The inner yoke thus forms part of the PM rotor, and not the slip rotor.

An advantage of this topology is evident when considering the final assembly of the machine. With the outside and inside yokes of the PM rotor fixed relative to each other and forming one single machine component, it allows the slip rotor to consist entirely of non-ferrous materials. This means that during assembly the slip rotor can easily be slid into position in between the two yokes, with no attractive forces influencing it. To construct the PM rotor with both yokes may still present some challenges, but once it is done it may remain fixed while the slip rotor may be removed and reinserted without the difficulty of magnetic attraction forces.

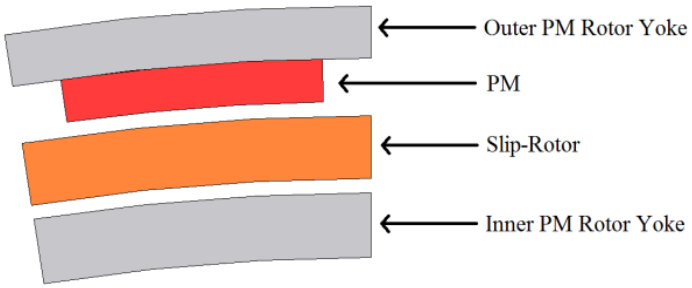

Fig. 2.1 Diagram of the first topology.

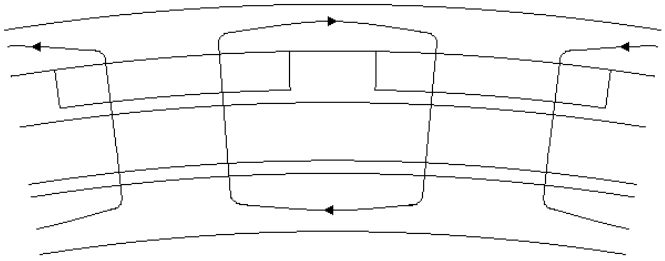

Fig. 2.2 Typical magnetic flux path of the first topology.

2.2 Second topology

The second topology considered has only one air gap. In this topology a second yoke is placed directly on the inside of the conductive material, as is shown in Fig. 2.3. Note that there is no air gap between the conductive material and the second yoke. The second yoke is fixed to the slip rotor and not the PM rotor, and therefore it rotates synchronously with the slip rotor. Thus, the PM rotor is only on the outside of the slip rotor, making this a single sided PM rotor topology.

The advantage of this topology is that it creates a smaller effective air gap with a lower magnetic reluctance. The lower reluctance is expected to lead to a higher flux density in the air gap and possibly to a better torque performance than the first topology. The construction of a single sided PM rotor is also simpler than that of a double sided PM rotor.

Some difficulty may be expected when constructing the slip rotor with the conductive material and yoke fixed to each other, but such challenges can be overcome. Unlike the first topology, assembly may cause trouble due to the attractive forces between the PM rotor and the yoke of the slip rotor.

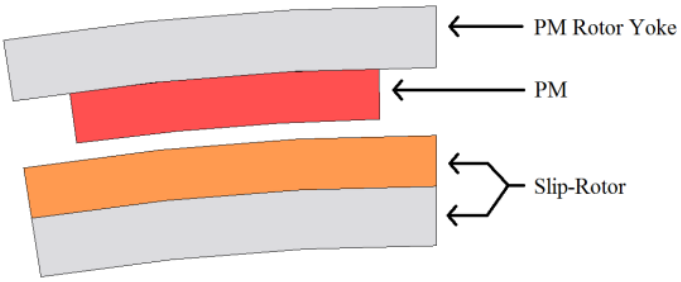

Fig. 2.3 Diagram of the second topology

2.3 Third topology

The final topology considered in this study is also a double sided PM rotor topology, but with magnets on both sides of the slip rotor. It is shown in Fig. 2.4. The outer and inner PM rotor yokes and magnets form one machine component rotating as a unit. The permanent magnets have the same magnetic orientation, so that the flux follows the flux path as indicated in Fig. 2.5. This topology uses the same total magnet material as the first two topologies to generate a specific flux, but it effectively halves the thickness of each magnet and doubles the number of magnets.

The advantage of placing the magnets on both sides of the slip rotor is that the constraints to limit stray flux in the air gap may be reduced, potentially allowing for a thicker conductive material in the air gap. Since there is no longer a yoke on the slip rotor the assembly is made easier because there are no attractive forces between the slip rotor and the PM rotor. The construction of the double sided PM rotor is complex, particularly due to the attractive forces between the magnets on both PM yokes. However, once the PM rotor's construction is done, the assembly and disassembly of the eddy current coupling is significantly simpler than for the single sided topology of section 2.2. Aside from the complexity of its construction, the manufacturing of the PM rotor is more labour intensive due to the increased number of magnets.

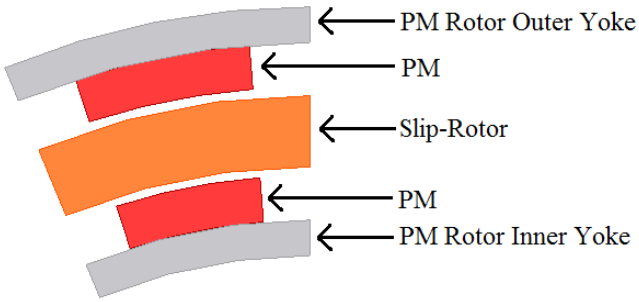

Fig. 2.4 Diagram of the third topology

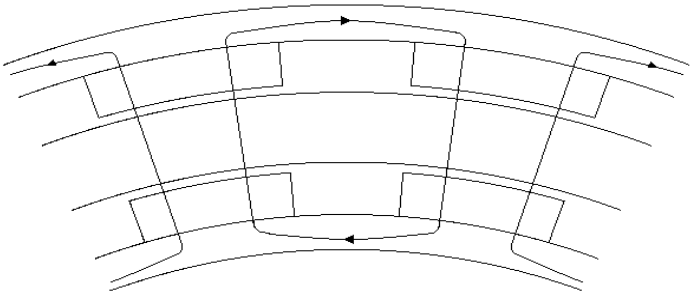

Fig. 2.5 Typical magnetic flux path of the third topology

3 Identifying the finite element model

In order to design the eddy current coupling it is necessary to know how it will perform under certain conditions, and how changes in dimensions will influence its performance. For this purpose it is preferable to use finite element simulations to predict the coupling's performance. Since the eddy current coupling is a rather unusual machine, the results given by FE packages cannot simply be taken as the reality. This chapter aims to find an accurate FE model for machines such as the eddy current coupling, and verify those results with practical measurements.

3.1 FE analysis

A small prototype PM rotor and slip rotor of the third topology (Fig. 2.4) was used in a previous project. That machine is again tested to allow comparison to FE results. First a 2D FE model is compared to the measured values, and then a 3D FE model is investigated for the small prototype.

Modelling the prototype using 3D FE was first attempted in Magnet version 7.2. However, due to strict boundary and coil requirements it was not possible to create a functioning 3D FE model for the eddy current coupling. As an alternative the 3D FE modelling was successfully done in JMAG Designer version 10.5. It was found that JMAG delivers accurate results, but is very time consuming in its simulation solving time. The 3D FE model and all other FE simulations presented in this study is done using JMAG Designer version 10.5.

Finite element simulations have various properties to be set. The mesh and simulation step size are two properties that can have a significant influence and are sometimes difficult to set correctly. For both the 2D and 3D simulations numerous simulations were done to determine a mesh fine enough that further increase in the number of elements has no effect on the results. It is a process repeated after any large changes are made to the FE models throughout this project. The size of the simulation steps has an influence on the 'smoothness' of the simulation result. It is important to set the step size fine enough to note any torque ripple in the simulation results, even though no ripple is expected.

The eddy current coupling functions on induction principles, where the movement of the electrical field relative to the conductive material induces eddy currents. Since the distribution of the eddy currents is unknown, transient solving of the FE model is a necessity.

3.2 The prototype

The machine to be modelled is a double-sided PM rotor topology with magnets on both sides, as described in section 2.3 and shown in Fig. 2.4. Each side of the PM rotor consists of 16 Neodymium Iron Boron (NdFeB) grade N35 magnets fixed to mild steel yokes, as is shown in Fig. 3.1. The magnet to pole pitch ratio of the PM rotor is 0.593. The slip rotor is a simple Aluminium Alloy 6082 cylinder that rotates in between the two sides of the PM rotor. It is shown in Fig. 3.2. The dimensions of the prototype are shown in Fig. 3.3 and Fig. 3.4. The lengths of the slip rotor on either side of the PMs of the PM rotor are known as the end-lengths. Note that the end-lengths of this rotor are not the same on both sides.

To test the performance of this prototype the torque is measured using a Lorenz Messtechnik type DR-3000 torque sensor. The slip-rotor is locked in position and the PM rotor is driven at the slip speed by a 0.37 kW induction motor through a 60:1 gearbox. The test setup is shown in Fig. 3.5. The induction motor is controlled and powered by a Danfoss variable speed drive. Measurements of the torque is taken at various slip speeds, in order to gain a torque versus slip characteristic plot for the machine.

In [**30**] two slip rotor's are tested and compared. One is a featureless aluminium rotor, such as is used in the eddy current coupling proposed in this project, and the other is a slotted aluminium rotor. The advantages of the slotted rotor are that it is simpler to model analytically and somewhat lighter than the solid rotor. It is found in [**30**] that the solid rotor performed better than the slotted rotor. In this study only the solid slip rotor shown in Fig. 3.2 is tested.

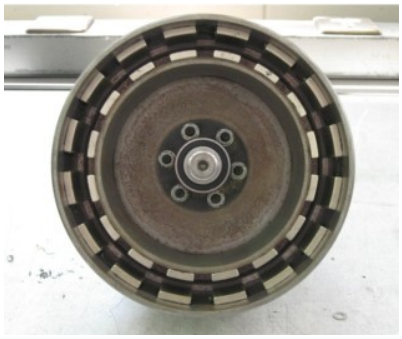

Fig. 3.1 Small prototype double sided PM rotor.

Fig. 3.2 Small prototype solid aluminium slip rotor.

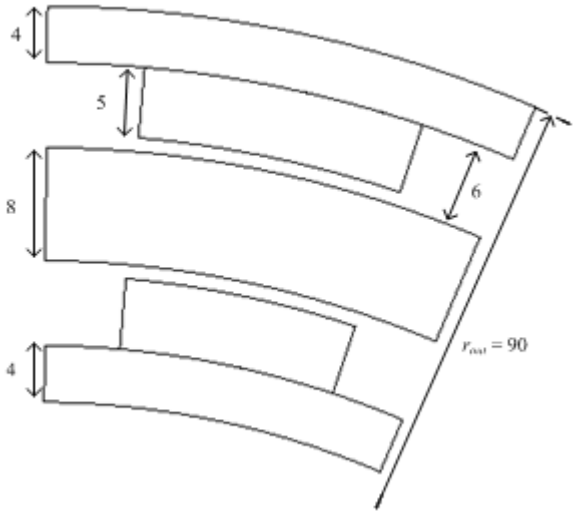

Fig. 3.3 The radial direction dimensions of the eddy current coupling, in mm.

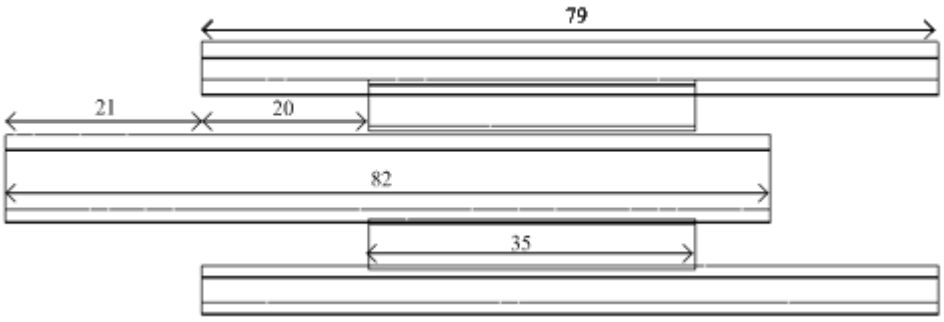

Fig. 3.4 The axial direction dimensions of the eddy current coupling, in mm.

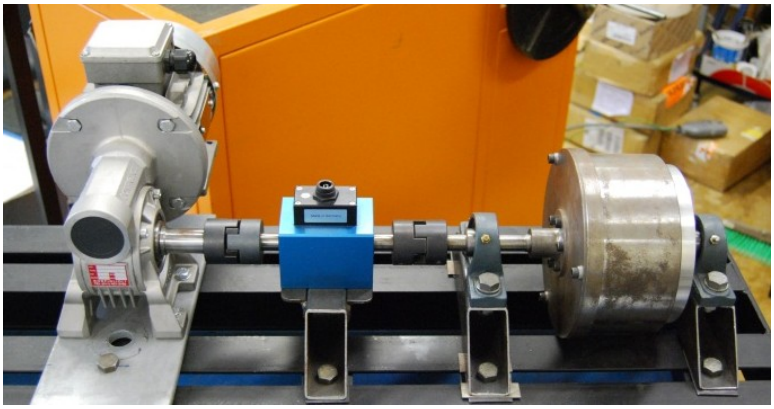

Fig. 3.5 Test setup with the eddy current coupling on the right, the torque sensor in the centre and the induction motor with its gearbox on the left.

3.3 2D FE model

In most literature where similar machines are analysed the assumption is made that all induced current flow only in the axial direction of the machine, which simplifies the modelling to a 2D space [**15**] [**16**] [**19**]. Some compensation may then be included for end-effects in the simulation package; however that is not possible in the case of the eddy-current coupling with a featureless loss drum, since there are no specified coils or conductor paths.

A 2D FE model of one pole of the machine was modelled. The model and its different components are shown in Fig. 3.6. The material properties and component dimensions used in the simulation were matched to the dimensions and properties of the materials of the prototype. However, since this is a 2D model, the axial lengths of all components are equal to the magnet length in the simulation model, whereas in reality the components have different axial lengths.

The 2D transient FE simulation took 10 seconds to solve the model for a simulated time period of 0.15 seconds. The simulation was repeated for various slip speeds in order to determine the machine's torque versus slip behaviour. In Fig. 3.7 the torque versus time behaviour is shown as predicted by the simulation for a 16% slip. Note that the torque is very smooth, without any torque ripple. The first 0.02 seconds of the simulation shown in Fig. 3.7 is the time it takes for the transient solution to reach steady state values.

In Fig. 3.8 the torque versus slip behaviour of the 2D FE simulation and the measured values are shown. It is clear that there is a significant difference between the simulated and measured results. Due to this discrepancy a 3D FE simulation is also investigated.

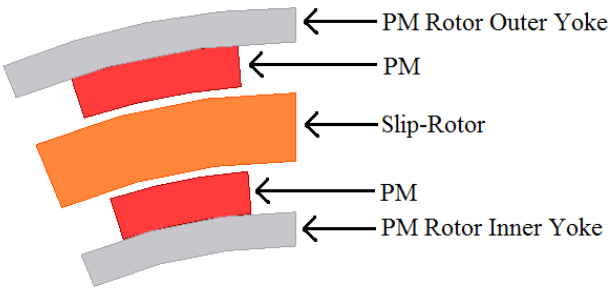

Fig. 3.6 Components of the 2D FE model in JMAG viewed in the *r-Θ* plane.

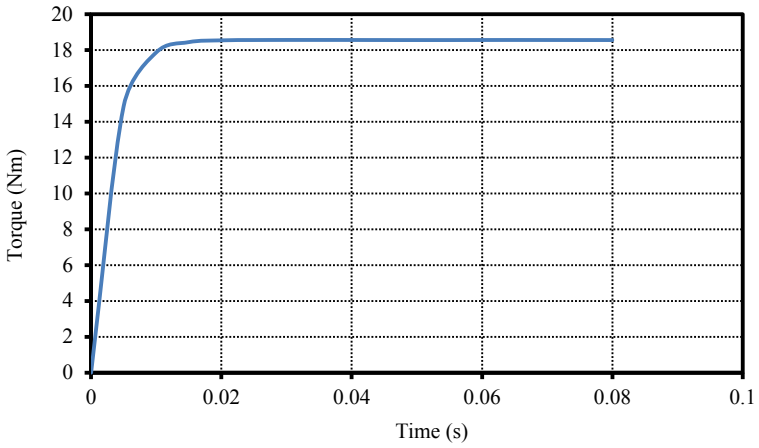

Fig. 3.7 2D FE transient simulation results of torque versus time for the small prototype at a 16 % slip.

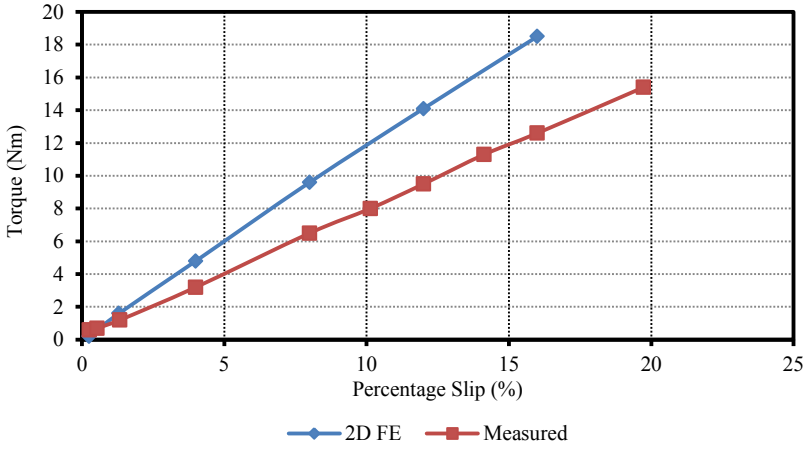

Fig. 3.8 2D transient FE simulated and measured results of torque versus slip of the small prototype.

3.4 3D FE model

In [**16**] an axial flux eddy current brake was simulated using a 3D FE package. The difficulties of 3D FE simulation is also stated, the most significant of which is the accurate solving of transient eddy currents in ferromagnetic materials. In all the eddy current couplings considered in this study the majority of the eddy currents are solved in a non-ferromagnetic material, which should considerably improve the accuracy. The limited publications available that compare 3D FE results to measured values where eddy currents are a predominant factor, is an indication of the difficulty involved with accurate 3D FE simulation [**16**]. It was found in this study that JMAG performed very well for the particular concept used.

The lengths of the components, additional to the magnet's active length, is expected to have a significant effect on the current, since it influences the available path for the current. In turn the generated torque is proportional to the induced current. The effect of the different axial lengths, particularly the longer axial length of the conductive material, was not included in the 2D FE model and contributes to the discrepancy between measured and simulated results.

A 3D FE model does allow for the different axial lengths of the different components in the prototype, as is shown in Fig. 3.9. In Fig. 3.9 the model is shown from its side. Its frontal view is the same as in Fig. 3.6. The dimensions and material properties used in the simulation were matched to the dimensions and material properties of the prototype.

The transient 3D FE simulation took 64 minutes to solve the model for 30 simulated time steps of 5 milliseconds each, 384 times longer than the 2D FE model. The torque versus time behaviour shown in Fig. 3.10 for 16% slip is again smooth without a torque ripple. The first 0.02 seconds shown in Fig. 3.10 is the time it takes for the transient solution to reach steady state values. The torque versus slip behaviour of the 3D FE simulation is shown with the results of the 2D FE simulation and the measured values in Fig. 3.11. It is clear that the results calculated by the 3D FE simulation is a very close comparison to the measured values, significantly closer than the results of the 2D FE simulation.

Even though the 3D FE simulation is significantly more time consuming than the 2D FE simulation, the 2D simulation does not give an acceptable prediction of reality for this kind of machine. One of the reasons is the different axial lengths of the components. A current density plot of the 3D FE model of Fig. 3.9 is shown in Fig. 3.12, where it is evident that the currents flowing in the axial length is not limited to the magnet length. This confirms that the axial length of the conductive material has a significant effect on the induced currents, and therefore the induced torque. It is also clear that the current path is not limited to a purely axial direction, but eddy currents flow in a direction tangential to the direction of the magnetic field rotation. In a 2D FE simulation the direction of current flow is limited to the axial direction.

Due to the unacceptable accuracy of the 2D FE simulation, and the excellent prediction of 3D FE simulation, it is decided that the 3D FE model is a good design tool for machines of this kind of topology. In this thesis, all further simulation studies of the eddy current coupling are done by means of JMAG's transient 3D FE solutions.

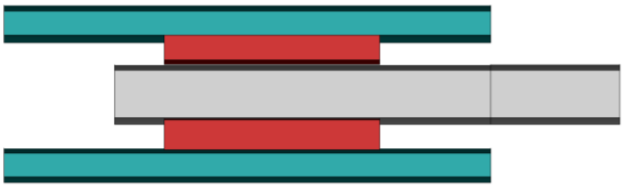

Fig. 3.9 Side view of 3D FE simulation model (*r-z* plane).

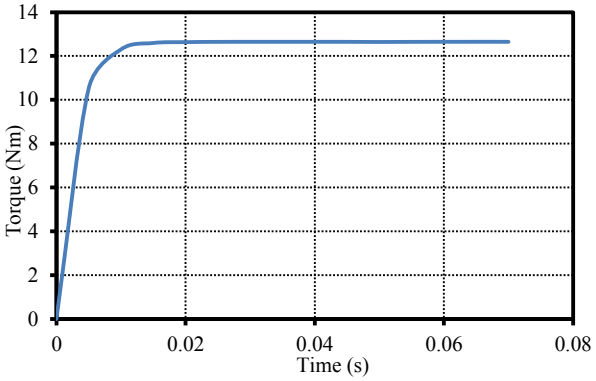

Fig. 3.10 3D FE transient simulation results of torque versus time for the small prototype at a 16 % slip.

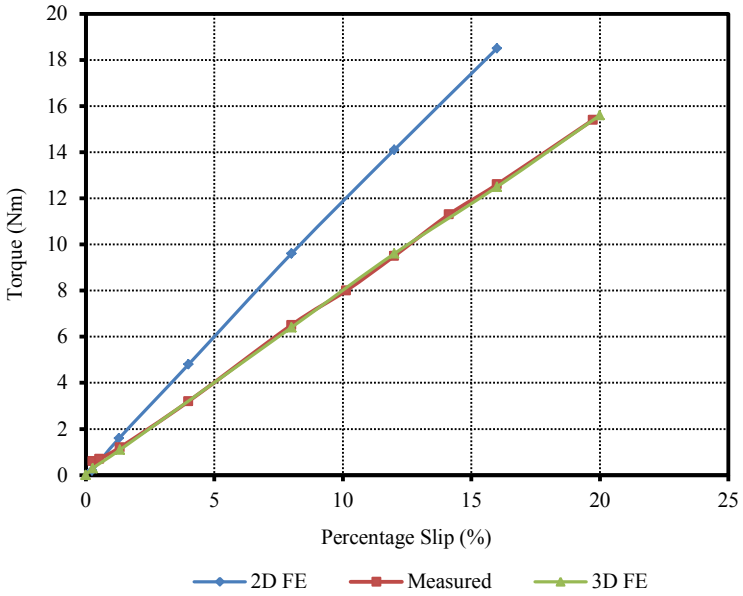

Fig. 3.11 Torque versus slip comparison of the 2D FE and 3D FE transient simulations and measured results.

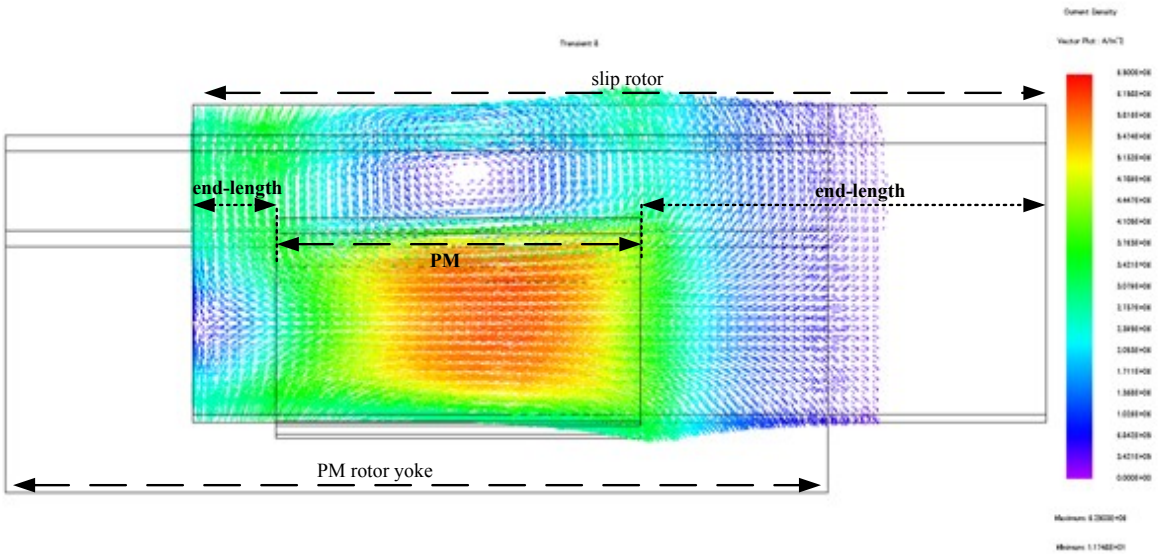

Fig. 3.12 Current density plot of the small prototype's 3D FE model in JMAG viewed in the Θ-z plane. Note the difference in axial end-lengths of the slip rotor.

4 Design of first prototype eddy current coupling for S-PMG

In order to test the eddy current coupling concept a prototype is to be built. In order to simplify this initial investigation it is decided to use an existing PM rotor from a previous study [**12**]. Therefore only the slip rotor needs to be designed and built. Two topologies of the eddy current coupling are to be designed using 3D FE simulations, and the better design is to be manufactured. This new prototype will allow for comparison of the FE prediction with measured results for a large scale machine, as well as indicate possible problems and considerations for constructing the slip rotor.

The existing PM rotor has a single-sided topology. Its dimensions and material properties are given in Table 4.1, and it is shown in Fig. 4.1.

Property	Value
PM material	N48H NdFeB
Yoke material	M470 non-oriented silicon steel
Outer diameter (mm)	653.5
Yoke thickness (mm)	7.25
PM height (mm)	6
PM axial length (mm)	100
Number of poles	40
Magnet to pole pitch ratio	0.73

Table 4.1 Dimensions and material properties of the existing prototype PM rotor.

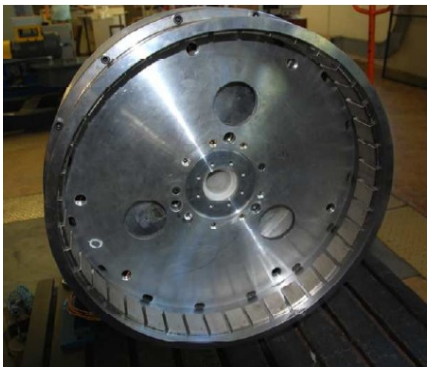

Fig. 4.1 The existing prototype PM rotor.

4.1 Considered topologies

Two slip rotor topologies are considered for use with the PM rotor. Both topologies must create a return path for the magnetic flux on the inside of the conductive material of the slip rotor. This means that both topologies have the existing PM rotor on the outside of the slip rotor, with the conductive material of the slip rotor in between the existing PM rotor and a second yoke to complete the magnetic flux's return path.

The topologies considered are the first and second topologies as described in sections 2.1 and 2.2 respectively. The first topology is again shown in Fig. 4.2 with the double sided PM rotor and the air gaps on both sides of the slip rotor. Similarly the second topology is shown in Fig. 4.3 with the single sided PM rotor and the slip rotor consisting of both the conductive material and second yoke.

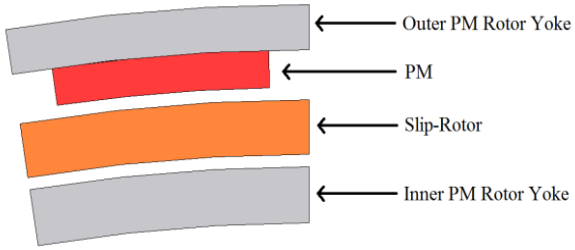

Fig. 4.2 Diagram of the first topology.

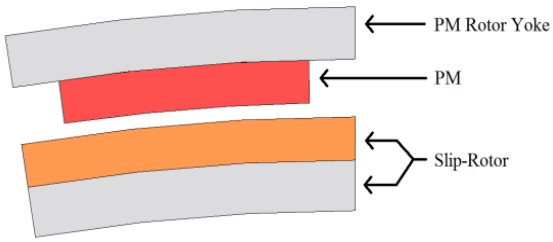

Fig. 4.3 Diagram of the second topology.

4.2 Design approach

4.2.1 Design specifications for the prototype eddy current coupling

Due to the use of an existing PM rotor, the design specifications of the S-PMG are adjusted from that given in section 1.2.2. The performance requirements for which the prototype is to be designed are as follows:

1. Minimum torque ripple;
2. Operating torque of 1000 Nm;
3. Maximum efficiency;
4. Minimum mass.

In points 1-4 the specifications are listed in descending priority. The torque ripple has to be as small and smooth as possible. If that is achieved the machine has to be able to operate at a rated torque of at least 1000 Nm. This means that the efficiency has to be maximised, subject to the operating torque remaining above 1000 Nm. Lastly the machine has to be as light as possible, since it is intended for operation in a wind turbine generator.

Torque ripple is removed by the decision to use an eddy current coupling with a featureless slip rotor. The efficiency is dependent on the slip speed, as shown by (1.1) and repeated here:

$$\eta = 1 - s \ . \tag{4.1}$$

Two materials are initially considered for the conductive material, namely aluminium and copper. Initial 3D FE simulations show that it is not possible to reach the torque requirement for acceptable low slip values using aluminium as the conductive material. It could be possible with a different PM rotor that could create a higher flux density in the air gap, but for the existing PM rotor the flux density in the air gap does not induce sufficient current to reach the torque requirement. Copper is a denser and heavier material, and it is more expensive than aluminium, but it has a higher conductivity. The higher conductivity means that for the same flux density and same efficiency as in the case of aluminium a higher torque is reached which does meet the requirement. In Fig. 4.4 the simulated torque performance at different slip values are shown for two machines. The two machines have the same dimensions and same flux density in the air gap. The only difference is that one machine has aluminium as the conductive material and the other machine uses copper. Due to the insufficient torque performance of aluminium it is decided to use copper as the conductive material of the slip rotor for this prototype.

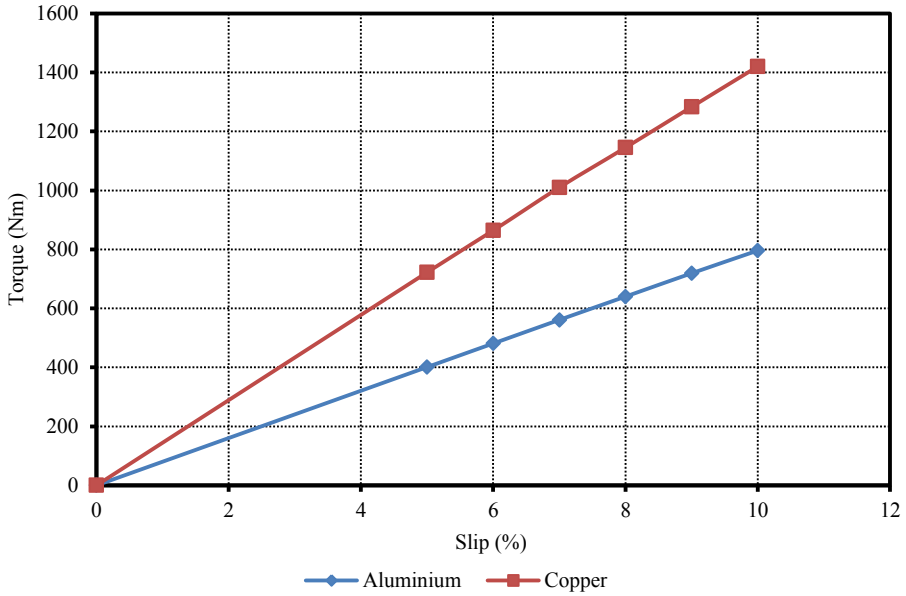

Fig. 4.4 Torque versus slip comparison of aluminium and copper slip rotors using 3D FE transient simulations.

4.2.2 Dimensions considered in the design

To simplify the analysis and design of the topologies two parameters are initially chosen as constants. The axial length of the copper component of the slip-rotor is chosen to be 140 mm, leaving 20 mm additional conductive material on either side of the 100 mm active length of the magnets. The second parameter to be kept constant is the slip at which the topologies are to be compared. Initial simulations indicated that 10% slip is necessary for the first topology to meet the second requirement of 1000 Nm operating torque if the copper length is 140 mm. The 10% slip corresponds to an efficiency of 90%. These parameters, the end-length and slip, are deemed to have the same influence on both topologies, and therefore have little influence on a fair comparison of the topologies if they are kept the same in the design of both topologies.

In order to minimise construction and assembly difficulties all radial air gaps are to remain the same as the original air gap for which the existing PM rotor was designed, namely 2 mm. The remaining dimensions that have to be determined for both topologies are the copper thickness of the slip rotor and the yoke thickness of the second yoke. Afterwards the axial length of the copper will be reconsidered.

4.2.3 Determining dimensions for maximum torque

In focusing the design of the eddy current coupling on maximum torque at 10% slip, the machine will be able to meet rated torque at a lower slip, which means efficiency is maximised. Therefore the output considered is the torque. Mass is a design specification, but it has a lower priority than efficiency. Therefore the machine is designed for maximum torque, and thus maximum efficiency, without needlessly increasing the mass of the machine.

If all parameters are kept constant and only the copper thickness is varied, the torque varies smoothly as a function of the copper thickness. At some point a maximum torque is reached, after which further increase in copper thickness leads to a decrease in torque. This behaviour allows for the bracketing of the peak torque using the simulation results of three different copper thicknesses.

The three copper thickness and their corresponding torque values may then be used to determine a curve approximating the second degree polynomial that describes the relation between the torque and

copper thickness. From this curve approximation the copper thickness for the maximum torque may be determined, corresponding to the other dimensions that were kept constant. This method has to be repeated for various yoke thicknesses.

The behaviour of the torque for varying copper thickness is to be expected. The torque is a combined effect of the flux density in the air gap and the induced currents. If copper thickness is increased the resistance of the current path decreases, but at the same time the reluctance of the flux path through the air gap is increased.

After the copper thickness corresponding to maximum torque has been determined, one may determine the most effective yoke thickness. The yoke thickness has an effect on the flux density in the air gap. If the yoke is too thin, the flux return path has a high reluctance, which limits the flux and corresponding flux density. However, if one increases the yoke thickness too much it no longer has any effect on the flux density as the yoke is no longer in saturation. This means that further increase in yoke thickness has no significant effect other than needlessly increasing the mass and cost of the machine. An easy way to find the yoke thickness corresponding to maximum torque is simply finding the yoke thickness for which further increase in thickness has negligible effect on the torque.

4.3 Design of the first topology

In this section the first topology (single PM, double air gap), as described in section 2.1, is to be designed for the prototype. As described in the previous section three 3D FE simulations are done, each with a different copper thickness and the rest of the parameters kept constant. This process is then repeated for different yoke thicknesses.

In Fig. 4.5 three torque versus copper thickness points of the first machine topology are shown for different yoke thicknesses of the second yoke. The second order polynomial line approximations are fitted over those points in Fig. 4.5. One can clearly see that the maximum torque is bracketed. It is also evident that with a thicker yoke thickness a higher torque is achieved. Using a line maximisation method for the second order polynomial line approximation the copper thickness corresponding to the maximum torque is determined to be 8.7 mm for thicker yokes.

Additional simulations were run to determine the yoke thickness corresponding to maximum torque for a copper thickness of 8.7 mm, as described in the previous section. The results are shown in Fig. 4.6. The point where the yoke is no longer saturated is 4.5 mm. For this topology, thus, it is decided to use a copper thickness of 8.7 mm and a yoke thickness of 5 mm. Using these dimensions the eddy current coupling generates 1023 Nm torque at 10% slip.

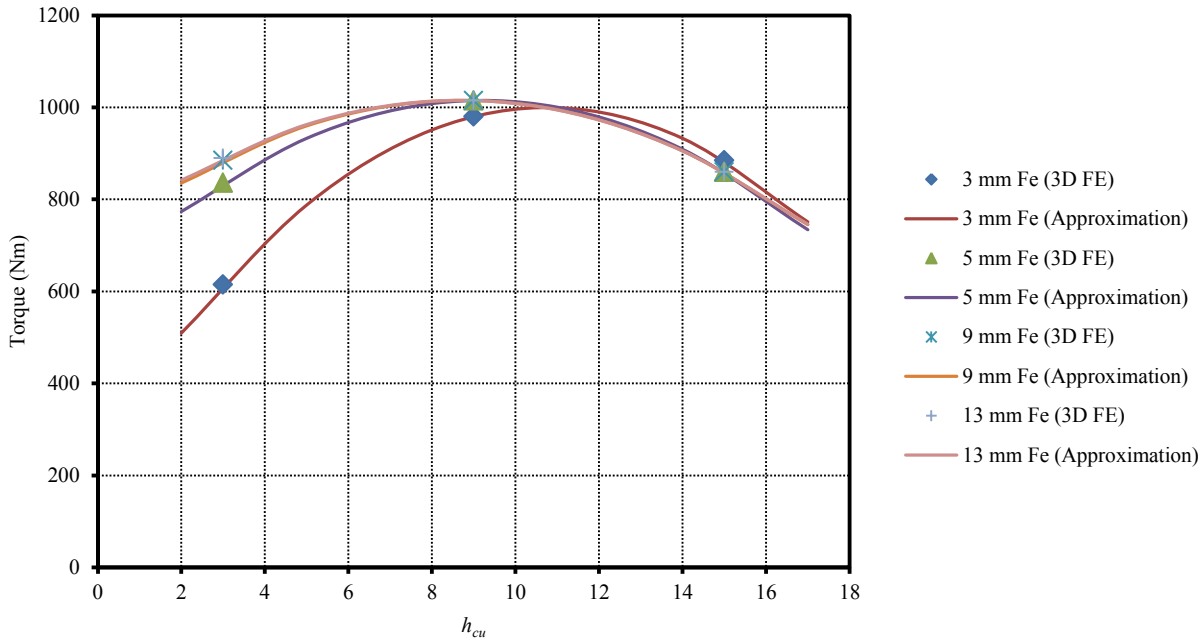

Fig. 4.5 Torque versus copper thickness with yoke thickness a parameter, using 3D FE transient simulations.

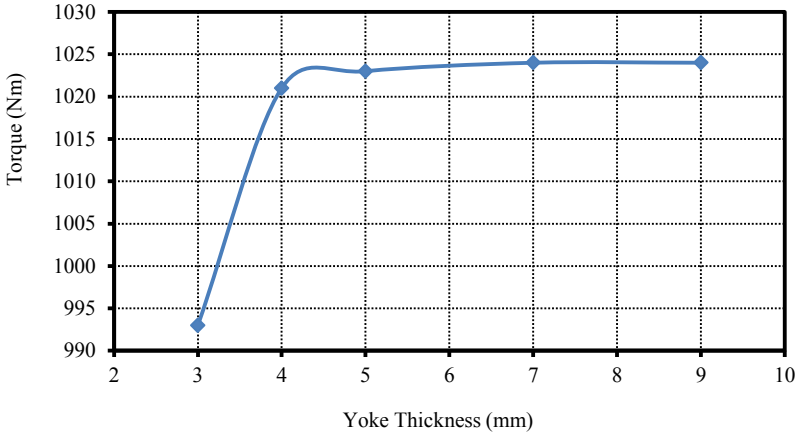

Fig. 4.6 Torque versus yoke thickness with 8.7 mm copper thickness, using 3D FE transient simulations.

4.4 Design of the second topology

The same design method, to determine the copper thickness that maximise the torque, is used for the second topology (single PM, single air gap) of Fig. 2.3 as was used for the first topology. The results are shown in Fig. 4.7. It is clear that with a thicker slip-rotor yoke a higher torque is achieved. Applying the line maximisation method to a second degree polynomial approximation of the torque versus copper thickness behaviour for thicker slip rotor yokes, it is determined that the optimal copper thickness tends to be 6 mm for the second topology.

Additional simulations are run to determine the best yoke thickness for a constant copper thickness of 6 mm. From the results in Fig. 4.8 it is clear that the yoke thickness has little influence on the torque for thicknesses of more than 6 mm. The desired thicknesses of the copper and the yoke for the second topology are 6 mm and 6 mm respectively. The torque generated using these dimensions is 1375 Nm at 10 % slip. Since this torque is significantly higher than the specified 1000 Nm, the second topology eddy current coupling can operate at a higher efficiency at rated torque.

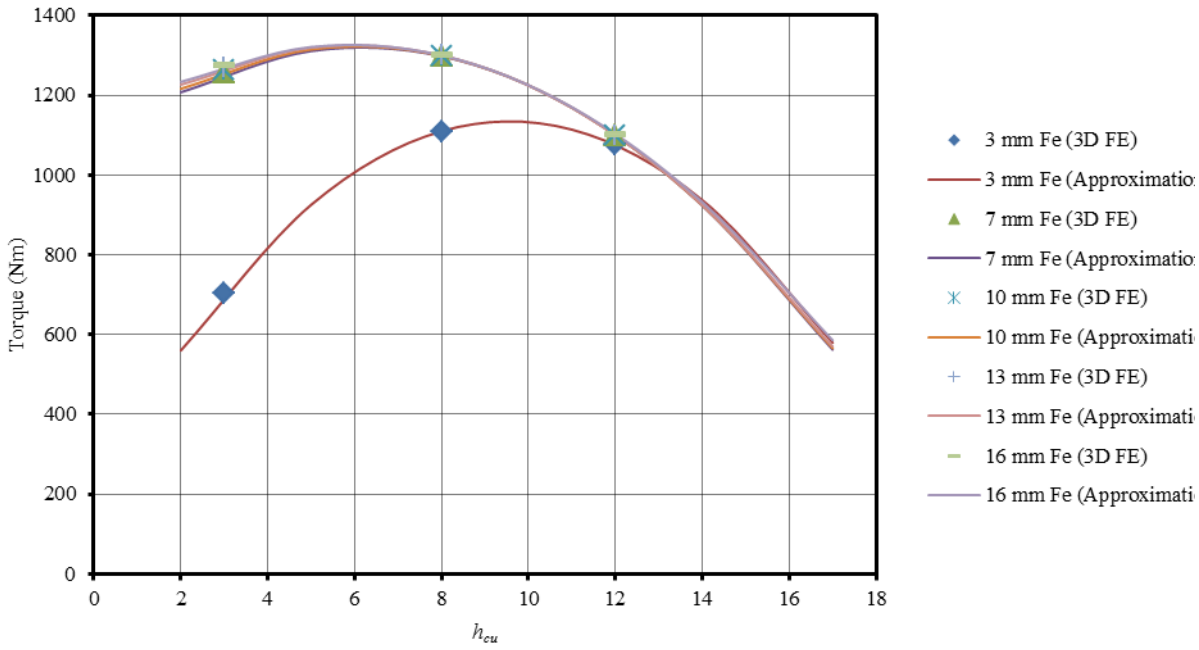

Fig. 4.7 Torque versus copper thickness with yoke thickness a parameter, using 3D FE transient simulations.

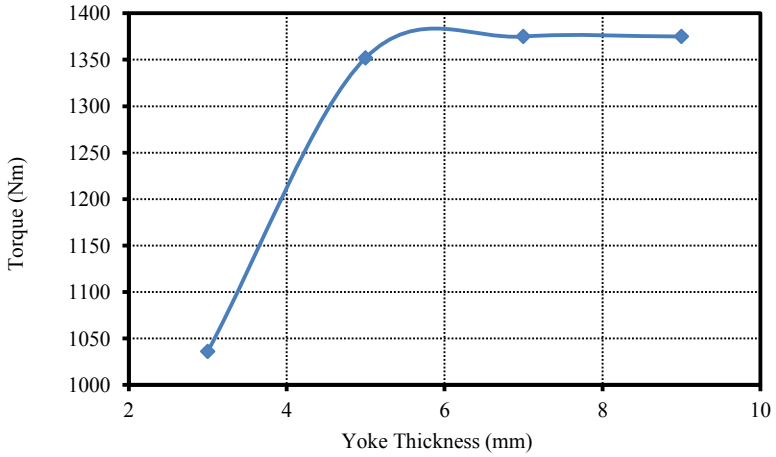

Fig. 4.8 Torque versus yoke thickness with 6 mm copper thickness, using 3D FE transient simulations.

4.5 Comparison of topologies

In the previous two sections two eddy current coupling topologies were designed for maximum torque at the same efficiency of 90%. From the results it is evident that at the same efficiency, and using the same amount of PM material, the second topology generates 34.4 % more torque than the first topology. When considering that the second topology also uses less copper it is a remarkable result. The difference in performance can be ascribed to the additional air gap necessary for the first topology, which increases the reluctance of the path of the magnetic flux and decreases the flux density in the effective air gap, thus reducing the induced currents and accordingly also the induced torque. The relevant information of the two machines is compared in Table 4.2.

Even though the first topology had significant constructional advantages, the difference in performance cannot be ignored. Due to the superior performance of the second topology for a lower mass than the first topology, further analysis of the first topology for the eddy current coupling is considered unnecessary.

Property	First Topology (Fig. 2.1)	Second Topology (Fig. 2.3)
h_{cu} (mm)	8.7	6
h_s (mm)	5	6
PM mass (kg)	6.58	6.58
Cu mass (kg)	22.30	14.47
Fe mass (kg)	18.43	19.98
Total active mass (kg)	47.31	42.03
T (Nm)	1 023	1 375
η (%)	90	90

Table 4.2 Design and performance comparison of the first and second topologies.

4.6 Conductor end-lengths

Since the PM rotor used is an existing rotor, its dimensions cannot be changed. The optimum copper thickness as well as the thickness of the second yoke are determined earlier in this chapter. The only other dimension on the slip rotor that can be changed is the axial length of the copper.

To determine the optimum axial length of the copper, with the active length of the copper fixed to be the same as the magnet axial length, the axial copper end-lengths are varied and the other dimensions are kept constant and the same as in Table 4.2 for the second topology. The end-lengths are the axial lengths of the copper on the outside of the magnet axial length. They are kept equal on both sides of the magnets. The results are shown in Fig. 4.9. The torque increases as a function of end-length up to a certain point, after which it basically remains constant.

It is interesting to note that this end-length corresponds to approximately 50% of a pole pitch. This can be understood from the JMAG-drawn current density plot in Fig. 4.10, where the end-lengths provide the same cross sectional area for the current to flow as the cross sectional area under the magnet, perpendicular to the direction of the current. This observation justifies the assumption that in all similar topologies the axial end-lengths of the conductive path may be taken as half a pole pitch.

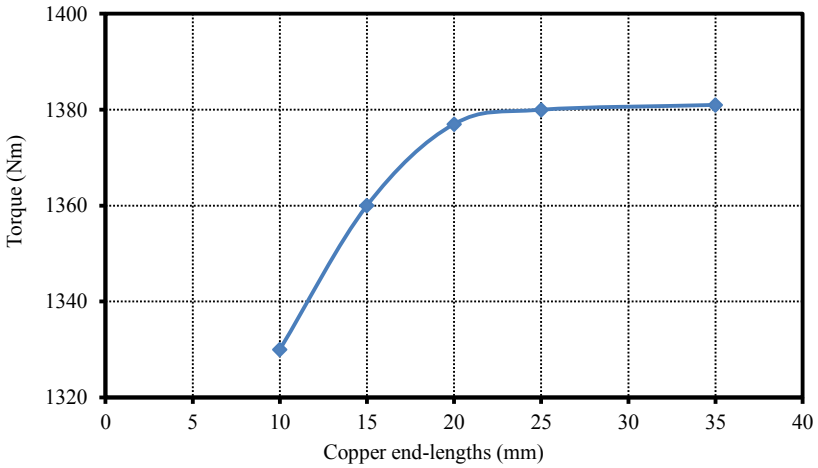

Fig. 4.9 3D FE calculated torque versus end-length of copper slip-rotor (active length constant).

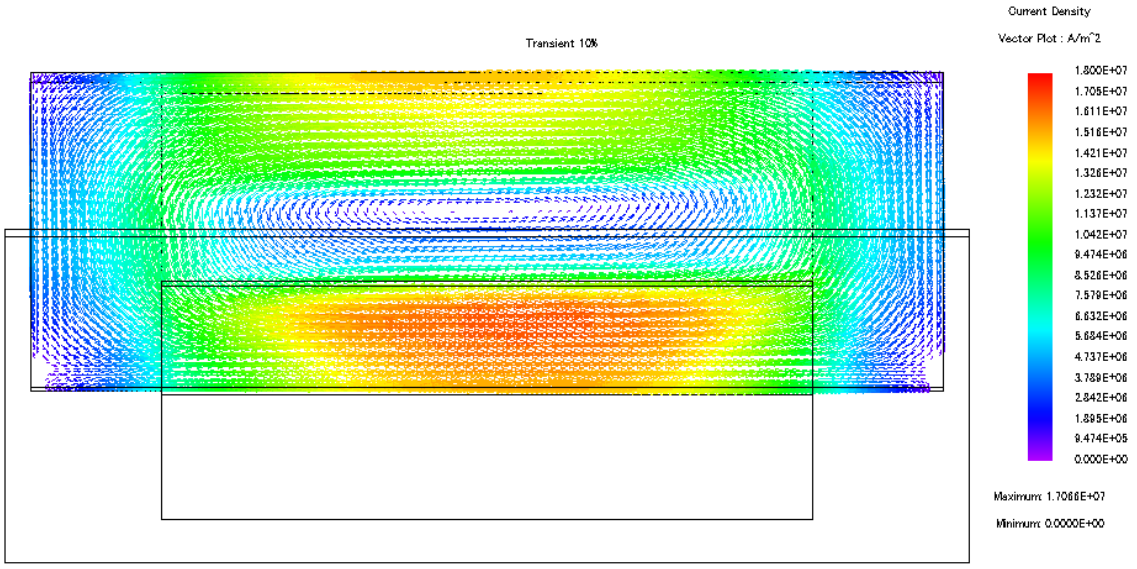

Fig. 4.10 JMAG 3D FE transient generated current density plot of second topology at 10% slip, viewed in the Θ-z plane.

4.7 Designed prototype slip rotor

The prototype designed in this chapter has the dimensions as described in Table 4.3, and is of the second topology, as shown in Fig. 4.3. The simulated performance of the prototype is shown in Fig. 4.11 as torque versus slip. It is expected to reach the designed 1000 Nm operating torque at approximately 6.24 % slip, which corresponds to an efficiency of 93.76 % as shown by (4.1).

Dimension	Value
d_{out}	653.5 mm
h_y	7.25 mm
h_m	6 mm
h_{cu}	6 mm
h_s	6 mm
p	40
τ_{pm}	0.7
l_{cu}	148 mm

Table 4.3 Designed prototype dimensions.

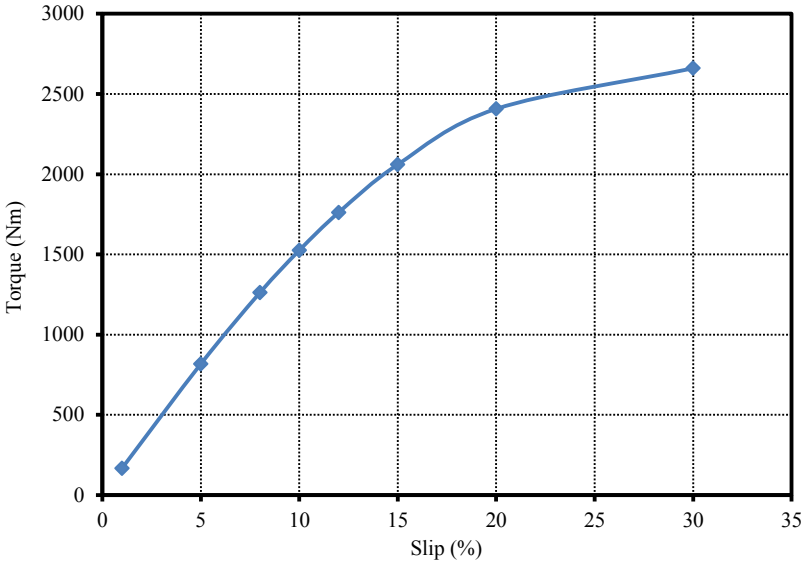

Fig. 4.11 3D FE simulated torque versus slip behaviour of designed prototype.

4.8 Prototype slip rotor construction

Construction of the slip rotor entails manufacturing of the copper ring, fixing the copper ring to the slip rotor yoke, and then fixing the yoke to the back plate, which is to be fixed relative to the remainder of the machine. It presents some constructional challenges.

The copper ring is created by rolling a flat copper plate of the appropriate dimensions into a ring as round as possible. The two ends then have to welded together. Copper is a very good conductor of heat, which means that it is difficult to braze or weld. It also expands with heat. It was calculated that for the designed machine the copper component of the slip rotor's diameter should increase by 1 mm for every 120°C increase in temperature. Even though the 2 mm air gap on both sides of the diameter allows this to happen to some extent, the prototype is expected not to reach such temperatures.

It was decided to manufacture the yoke from laminations. This ensured that the yoke was round within fairly strict tolerances. Using the laminations a circular stack can be assembled on a back plate, over which a copper ring fits. The copper ring is tooled on the inside to fit the yoke stack. The fitting has to be carefully spaced in order to make sure that the axial end-lengths are equal on both sides of the active yoke length. The outside diameter of the copper ring is to be machined to the appropriate diameter once the yoke, copper ring and back plate have been assembled into a manageable unit. Fig. 4.12 shows a cutaway diagram of the assembly of the different components of the eddy current coupling. It consists of the back plate, the shaft, the slip rotor yoke and the copper ring.

Small grooves are machined in the axial direction on the inside of the copper ring to match with ridges protruding out on the yoke. These grooves are expected to prevent the copper ring from moving in the tangential direction on the yoke. The forces experienced by the copper ring will be mainly in the tangential direction. Because it is a non-ferrous material the only forces it should experience in the radial direction is due to momentum and forces from the yoke on which it is fitted.

During manufacturing of the copper ring some difficulties were experienced. The copper plate proved difficult to roll to an accurate degree of roundness. It was also very difficult to braze the two ends of the rolled plate to form a ring. Copper is a fairly soft metal, which makes it difficult to machine, which presented additional problems with the initial tooling of the inside of the ring. The rolled copper ring is shown in Fig. 4.13 before its two ends were welded together.

Fig. 4.14 shows the laminated yoke in the centre of the copper ring and connected to the back plate using spacers. Due to the inaccurate manufacture of the copper ring there were small air gaps between the inside of the copper ring and the stack in some places. The largest of these gaps are shown in Fig. 4.15. Fig. 4.15 also clearly shows the groove in the copper ring with its matching ridge on the yoke. To prevent vibrations and help fix the copper to the stack, resin was poured into the gaps. Machining the outside diameter of the copper once the ring was fixed to the stack and the stack was fixed to the back plate proved easy considering the earlier difficulties.

Further trouble was experienced though. The existing PM rotor's true dimensions were slightly different from its original design specifications. Though the PM rotor was measured beforehand, it is difficult to do so to an accurate degree and evidently some small errors were made. To compensate for this difference the outside of the copper ring was machined to a slightly smaller dimension, and the air gap in the final assembled eddy current coupling was also smaller than 2 mm.

The final dimensions of the constructed prototype are given in Table 4.4 and the constructed prototype slip rotor is shown in Fig. 4.16.

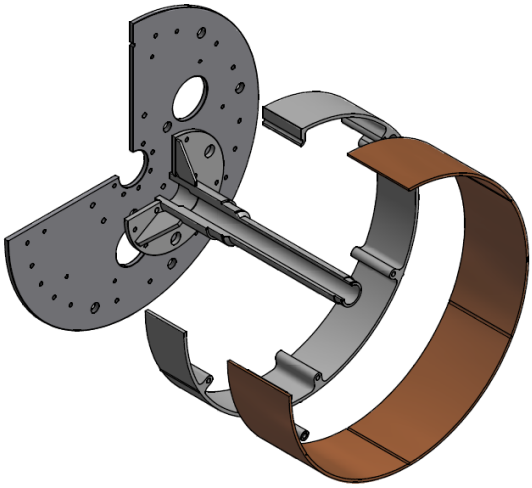

Fig. 4.12 Cutaway diagram of the assembly of the prototype slip rotor components, including the shaft and back plate.

Fig. 4.13 Rolled copper ring during slip rotor manufacture process.

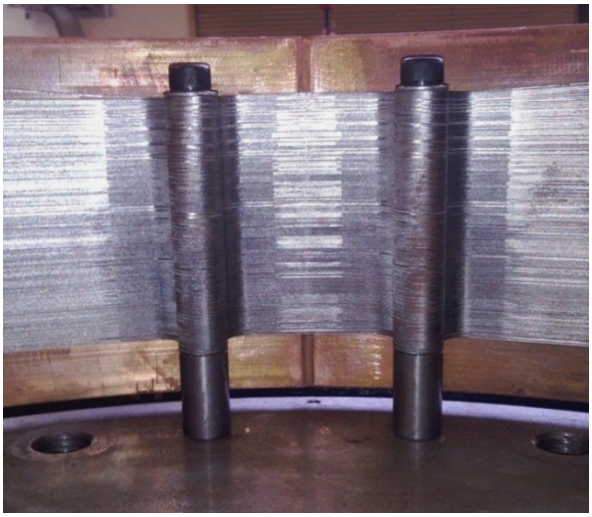

Fig. 4.14 Slip rotor viewed from the inside.

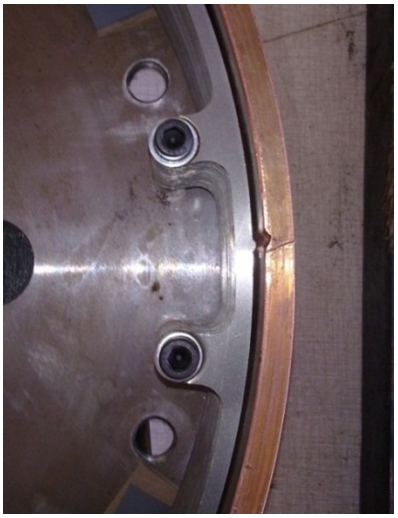

Fig. 4.15 Slip rotor viewed from the axial direction.

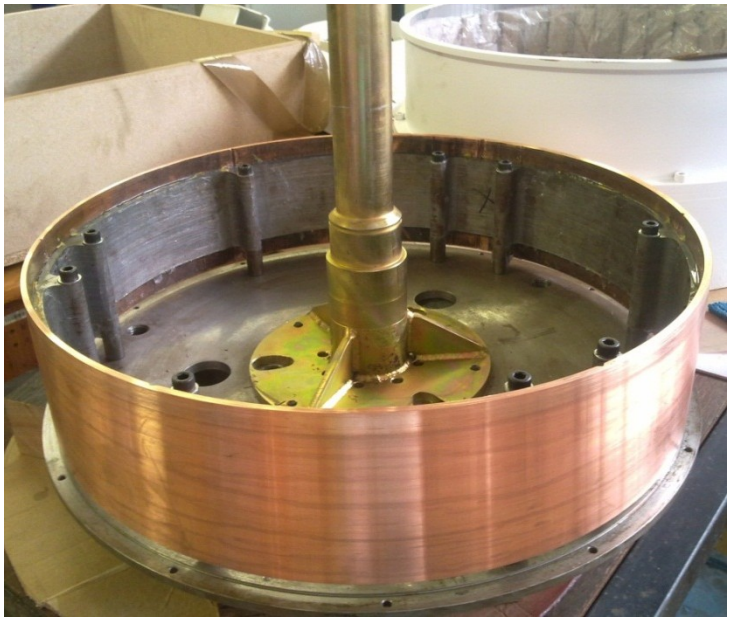

Fig. 4.16 Manufactured and assembled slip rotor, including shaft and back plate

Dimension	Value
g	≈0.75 mm
h_{cu}	≈5.35 mm
h_s	7 mm
p	40
τ_{pm}	0.73
l_{cu}	148 mm

Table 4.4 Manufactured prototype dimensions

4.9 Comparison of calculated and measured results

The assembled eddy current coupling is tested by keeping the PM rotor locked in a stationary position, and rotating the slip rotor at slip speed. The slip rotor is connected to a Lorenz Messtechnik DR-2212 torque sensor by means of a prop shaft. The torque sensor is in turn connected to a 67:10 gearbox, which is used to transfer power from a 4-pole 45 kW induction motor, which is used to simulate a wind turbine. An Allen-Bradley Powerflex 700 drive is used to apply speed control to power the induction motor.

The torque is measured for various slip values, up to the maximum rating of the torque sensor, namely 2000 Nm. The results are shown in Fig. 4.17. Rated torque was achieved at 8% slip, which corresponds to 92% efficiency. The measured torque has very linear behaviour with varying slip for low slip values.

It should be noted that due to the increased flux density in the air gap, and the very small air gap, the eddy current coupling's temperature increased rapidly. Since temperature has in influence on the measured results, the tests are repeated several times. Each time the machine is operated up to approximately 80°C, measurements of slip versus torque are taken, and the machine is allowed to cool before further tests are done.

Since the constructed prototype has different dimensions from the designed prototype one expects a difference in its performance. 3D FE simulations were done with the actual machine dimensions and material properties to be able to make a fair comparison between the constructed machine and the FE prediction. The results of the simulations are also shown in Fig. 4.17. Though breakdown torque was not measured, from the simulation results it is approximately 2900 Nm, well within the specifications of Table 1.1. It is evident that the simulated values are a good match to the measured values throughout the range of the measurements, with the largest error being less than 4.5%.

Due to the small air gap it is not possible to measure the flux density in the air gap using a Gauss meter, however according to the matched 3D FE simulation the flux density is 0.58 T.

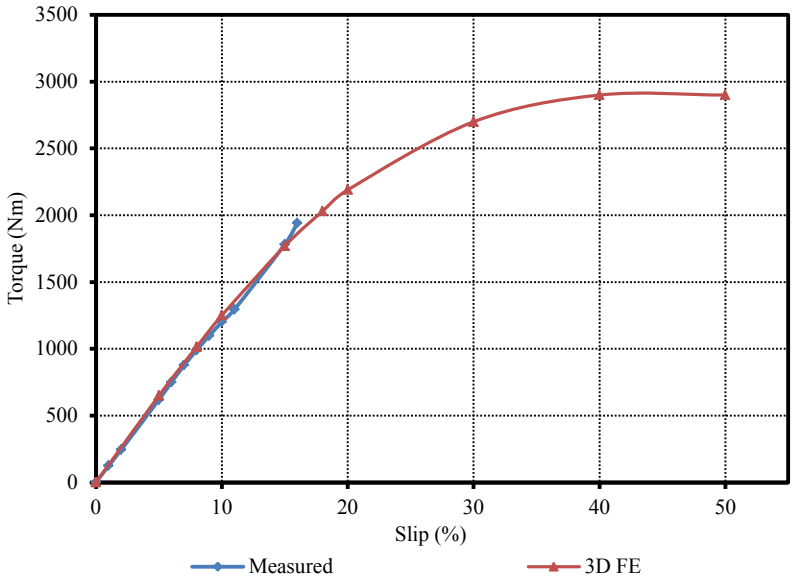

Fig. 4.17 3D FE simulated torque versus slip behaviour compared to measured results.

4.10 Summary of findings

The second topology (single PM, single air gap), as described in section 2.2, has a superior performance to that of the first topology (single PM, double air gap) from section 2.1. The difference is significant enough that further analysis of the first topology is considered unnecessary.

It is found that the end-lengths of the conductive material of the slip rotor may be designed as 50 % of a pole pitch. It is also shown that 3D FE simulations match very well to the measured results. Due to the good correlation between 3D FE results and reality it is assumed throughout the remainder of this project that comparison to the simulated values is as good as comparison to a real machine. Making this assumption removes the need for further expensive and time consuming prototype construction.

The construction of the eddy current coupling still presents some serious challenges, and should be investigated further. Construction methods that would lead to more accurate manufacturing of the eddy current coupling, particularly the slip rotor, has to be found to make economical production of the machine more practical.

Lastly it should be noted that accurately measuring transient torque ripple is very difficult, particularly if the torque sensor measures the torque between the turbine and the eddy current coupling. According to the FE simulations there is no torque ripple in the eddy current coupling.

5 Development of the analytical model

In order to do the full, optimal design of the eddy current coupling, meaning both the PM rotor and the slip rotor, many dimensions may be varied. Many variations mean that many iterations are necessary to truly optimise the machine. Due to 3D FE simulations being very time consuming and resource intensive, it is preferable to create an analytical model that can predict the performance of the machine mathematically.

In this chapter an analytical model of the eddy current coupling is proposed. The analytical model calculates the torque based on the eddy current coupling's dimensions, with the purpose of designing a machine according to the specifications of section 1.2.2.

5.1 Modelling approach

The analytical model is first determined for the second topology (single PM, single air gap) as described in section 2.2. In section 5.9 the necessary changes are made to the model in order to be able to use it for the third topology (double PM, double air gap) as described in section 2.3. Generally torque is calculated as

$$\boldsymbol{T} = \boldsymbol{r} \times \boldsymbol{F} \,, \tag{5.1}$$

with $\boldsymbol{T}$ the torque vector, $\boldsymbol{r}$ the displacement vector from the point where the torque is measured to the point where the force is applied, and $\boldsymbol{F}$ the force vector. It can be simplified to the calculation of the magnitude of the torque [**31**], T, as

$$T = rF\sin\theta \,, \tag{5.2}$$

where $F\sin\theta$ is the magnitude of the force perpendicular to the displacement vector $\boldsymbol{r}$ and r is the magnitude of that displacement vector.

In an electrical machine the force used in the torque calculation is the force due to electrical current in a magnetic field. Force experienced by a current-carrying conductor in a magnetic field is calculated using

$$\boldsymbol{F} = i(\boldsymbol{l} \times \boldsymbol{B}) \tag{5.3}$$

which has its origin in the Lorentz force law. $\boldsymbol{B}$ is the magnetic flux density vector, i the magnitude of the current in the conductor and $\boldsymbol{l}$ the length of the conductor in the magnetic field. The direction of $\boldsymbol{l}$ is defined to be in the direction of current flow. It can be simplified to

$$F = ilB\sin\theta \,, \tag{5.4}$$

if $l\sin\theta$ is taken as the length of the conductor in the field perpendicular to the direction of the force, and B the magnitude of the flux density vector.

In the eddy current coupling currents are induced in the slip rotor due to movement in the magnetic field created by the PM rotor. These induced currents induce a force according to (5.4) and a corresponding induced torque according to (5.2). In order to calculate the torque both the magnetic field and the induced currents have to be determined.

5.2 Flux density in the air gap

To calculate the induced currents and the induced force one needs the flux density of the magnetic field in the air gap. The approach followed here is closely based on the work done in [**28**]. The flux density in the air gap is calculated based on known material properties and dimensions.

The flux density in a material may be calculated as

$$B = \mu H = \mu_r \mu_0 H \ , \tag{5.5}$$

with H the magnetic field strength in A/m and μ the permeability.

Fig. 5.1 shows the flux path for one pole pair of the second topology eddy current coupling, with the separate poles indicated by the dashed lines. If one considers the magnetic circuit of one pole, the MMF equation is

$$\begin{aligned} H_c h_m &= 2H_y \frac{l_y}{2} + H_m h_m + H_g l_g + 2H_s \frac{l_s}{2} \\ &= H_y l_y + H_m h_m + H_g l_g + H_s l_s \ , \end{aligned} \tag{5.6}$$

with l_y the tangential length of a single pole pitch in the outer yoke, and l_s the tangential length of a single pole pitch in the inner yoke. l_g is the effective radial length of the air gap, the combination of the non-ferrous conductor radial thickness and the actual air gap radial length, as shown in (5.7). These dimensions are shown in Fig. 5.2 and Fig. 5.3, and may be calculated as

$$l_g = h_{cu} + g \ , \tag{5.7}$$

$$l_y = \frac{2\pi r_y}{p} \ , \tag{5.8}$$

$$l_s = \frac{2\pi r_s}{p} \ , \tag{5.9}$$

with h_{cu} the thickness of the conductive material, g the radial thickness of the air gap, r_y the effective radius of the outer yoke, r_s the effective radius of the inner yoke, and p the number of poles. Taking into consideration that the permeability of the magnet material may be calculated as $\mu_m = B_r/H_c$ in its linear region, and by making the assumption that the flux density in the air gap and the flux density in the magnet are equal, (5.6) becomes:

$$H_c h_m = H_y l_y + B_g \left(\frac{H_c}{B_r} \right) h_m + \left(\frac{B_g}{\mu_0} \right) l_g + H_s l_s \tag{5.10}$$

where H_c and B_r are constants dependent on the magnet material temperature, and H_y and H_s are dependent on the flux density in the steel. When making B_g the subject of (5.10), it becomes

$$B_g = \frac{H_c h_m - H_y l_y - H_s l_s}{\left(\frac{H_c}{B_r} \right) h_m + \frac{l_g}{\mu_0}} \ . \tag{5.11}$$

Equation (5.11) is the analytical calculation of the flux density in the air gap, based on material properties and machine dimensions.

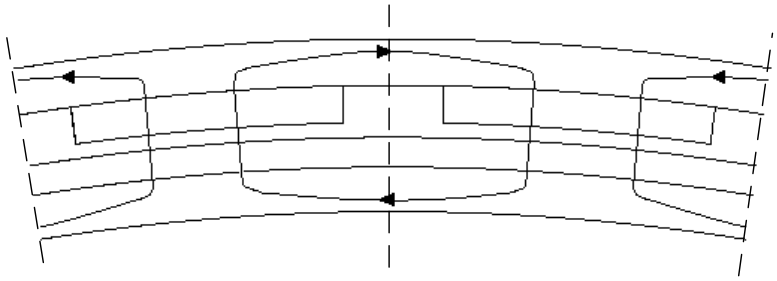

Fig. 5.1 Typical magnetic flux path diagram for the second topology.

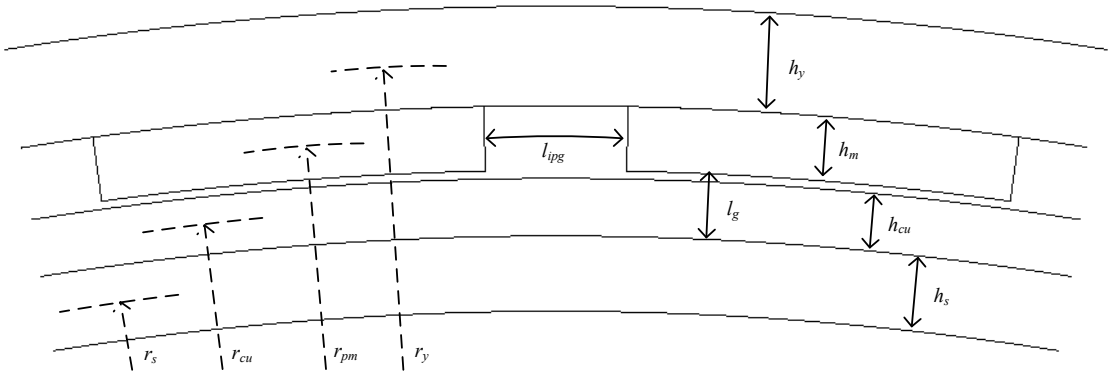

Fig. 5.2 Dimension symbols for the second topology.

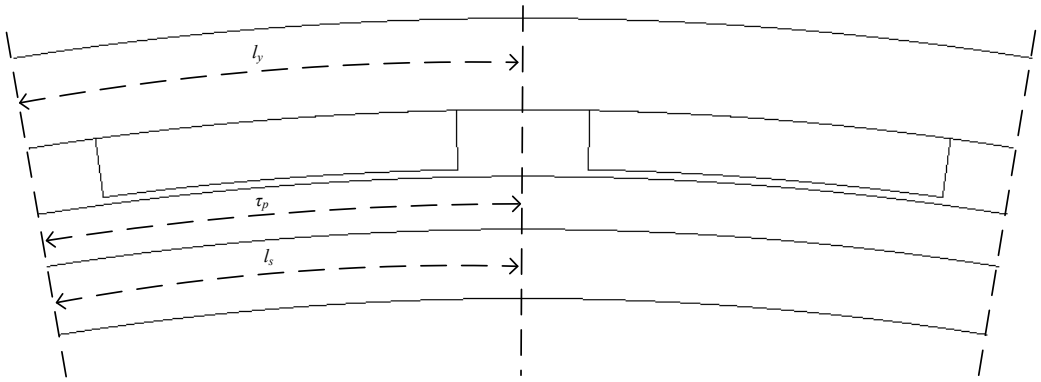

Fig. 5.3 Additional dimension symbols for the second topology.

5.2.1 Properties and dimensions determined during flux density calculation

To use (5.11) it is necessary to determine some of the material properties and dimensions used in the machine. The dimensions to be determined are h_m, h_{cu}, h_y, and h_s. These four thicknesses have an influence on the radii used in (5.7) - (5.9). We consider the number of poles and the air gap radial length, g in (5.7), constant for the time being.

The material properties to be chosen include the properties that are sensitive to temperature. In Fig. 5.4 the B-H characteristic curve of grade N48H NdFeB magnets are given for different temperatures. H_c in (5.11) is the coercive magnetic field strength, describing the force necessary to demagnetise the

magnet in A/m. B_r is the residual magnetization of the magnet, describing the magnetization of the magnet after an external magnetic field has been removed. H_c and B_r are shown in Fig. 5.4 for different temperatures.

It is important to note that temperature has a significant effect on the properties of some materials. Based on the measurement taken during the tests done on the prototype in chapter 4, it is estimated that the eddy current coupling will operate at a temperature of approximately 60°C if the manufactured dimensions are as designed.

Fig. 5.5 shows the B-H behaviour of M470-50A steel. The flux density in the steel varies with the yoke thicknesses of the machine. Consequently the yoke thicknesses may be determined by choosing a fixed flux density in the steel, which ensures that the field strength in the steel in (5.11) is constant. The yoke thicknesses may then be determined by

$$h_y = \frac{l_y \tau_{pm}}{2}\left(\frac{B_g}{B_y}\right), \tag{5.12}$$

$$h_s = \frac{l_s \tau_{pm}}{2}\left(\frac{B_g}{B_s}\right), \tag{5.13}$$

where τ_{pm} is the ratio of the magnet pitch in relation to the pole pitch, and B_y and B_s are the chosen flux densities in the steel of the outer and inner yokes respectively.

Since h_y and h_s are necessary for the calculation of r_y and r_s, the flux density in the air gap, the flux density in the steel, and the yoke thicknesses are dependent on each other, as shown by (5.8) - (5.13). Therefore it is necessary to make an initial assumption of the yoke thicknesses to calculate the air gap flux density. It was found that choosing the yoke thicknesses equal to the magnet height is a good first approximation. Using the newly calculated air gap flux density more accurate yoke thicknesses are calculated, and the process is repeated until there is no more change in either flux density or yoke thickness. It was found that five iterations are generally sufficient.

The flux densities in the yokes are chosen to be 1.4 T. As can be seen in Fig. 5.5 this flux density is the value just before the steel goes into saturation. It is therefore the desired flux density that allows for the most efficient use of the material. In choosing $B_y = B_s = 1.4$ T the corresponding magnetic fields are chosen as $H_y = H_s = 500$ A/m. The thicknesses h_y and h_s may now be calculated using (5.8) - (5.13), dependent on the remaining thickness dimensions h_{cu} and h_m.

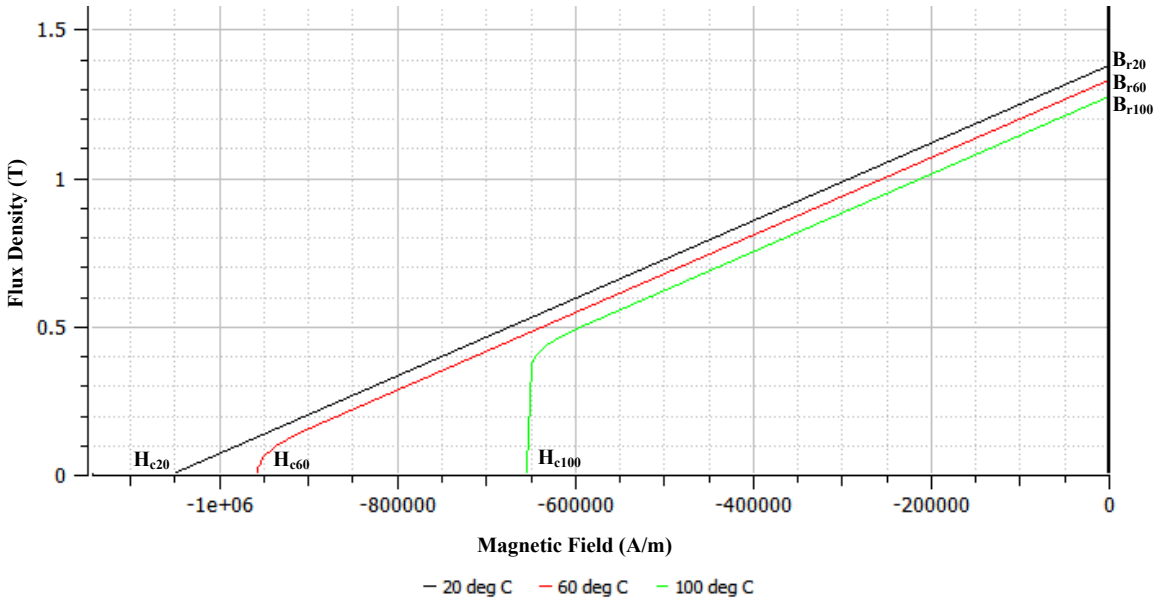

Fig. 5.4 B-H behaviour used in JMAG for N48H NdFeB magnetic material at different temperatures.

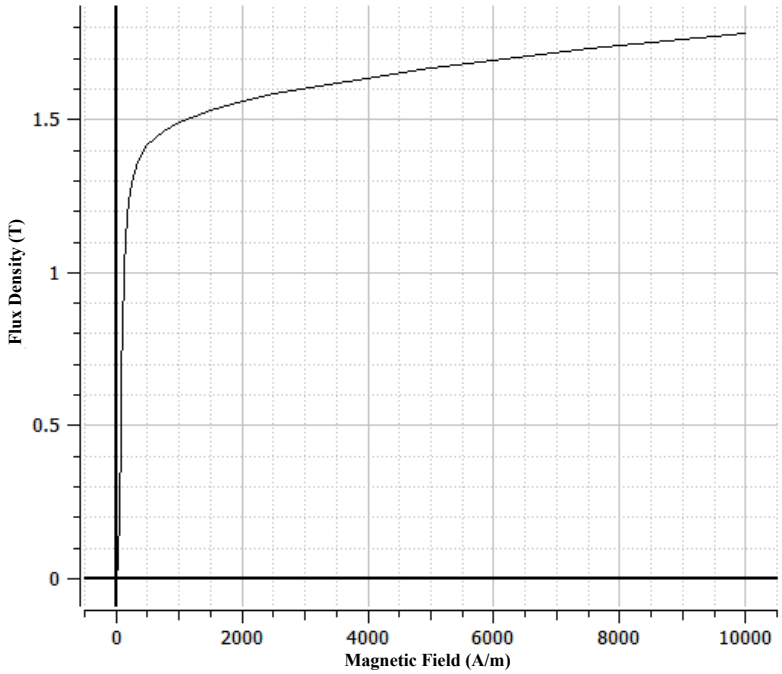

Fig. 5.5 B-H behaviour used in JMAG for M470-50A steel.

5.2.2 Flux density related constraints

The calculation of the flux density using the MMF equation (5.6) is done assuming no losses due to stray flux. To limit stray flux, and thus allow the use of (5.11), some constraints have to be implemented on the dimensions. The first constraint is to prevent stray flux between the magnet and the yoke to which it is attached, that is

$$h_m > l_g \ . \tag{5.14}$$

If the magnet height is larger than the length of the air gap the reluctance path between the magnet and the second yoke is lower than the reluctance path between the magnets radial face and the outer yoke.

The second constraint is to prevent stray flux between two adjacent magnets:

$$l_{ipg} = \frac{2\pi r_{pm}}{p}(1-\tau_{pm}) > 2l_g \ , \tag{5.15}$$

with l_{ipg} the arc length between two adjacent magnets, as shown in Fig. 5.2. Equation (5.15) ensures that the reluctance path through the air between two adjacent magnets is higher than the reluctance path from one magnet to the opposite yoke and back to the adjacent magnet. These constraints are specific to the second topology, and are significantly different from those for the third topology.

5.2.3 Harmonic and fundamental flux densities in the air gap

It should be noted that the flux density calculation done in this chapter is for the amplitude of the fundamental harmonic of the air gap flux density. The per unit air gap flux density of a 60 pole eddy current coupling of the second topology is shown in Fig. 5.6, as calculated from the results of a 3D FE simulation. The flux density plot shown is calculated for one pole pair of the PM rotor. Fig. 5.7 is the result of using Fourier analyses on the flux density waveform. It shows the per unit amplitude of each harmonic of the flux density wave.

Also shown in Fig. 5.6 are some of the harmonic waves with amplitudes as shown in Fig. 5.7. The approximation of the flux density used in the analytical model is the fundamental harmonic, namely $B_{g1}\sin(\omega_1 t)$. However, it is clear that the actual flux density waveform is not exactly sinusoidal, but rather the sum of its harmonics. The dominant harmonic is the fundamental harmonic, with only the 5th and 7th harmonics having notable amplitudes. Since the amplitudes of the 5th and 7th harmonics are more than 14 times smaller than the fundamental, it is easy to consider them as negligible and simplify the analytical model to using only the 1st harmonic.

In [**28**] the flux density in the air gap is closely approximated as a flat-topped trapezoidal wave. Using that approximation it can be shown that the ratio, b, between the actual flux density in the air gap, B_{ag}, and the amplitude of its fundamental harmonic, B_{g1}, is:

$$b = \frac{B_{ag}}{B_{g1}} \approx 0.937 \tag{5.16}$$

The ratio changes with the magnet to pole pitch ratio, τ_{pm}. It was found in [**32**] that an optimal value for τ_{pm} is 0.7, which is what will be used in this eddy current coupling. The same value for b may be used in this analytical approximation as was used in [**28**], because the same magnet to pole pitch ratio is used and the air gap flux density has the same behaviour.

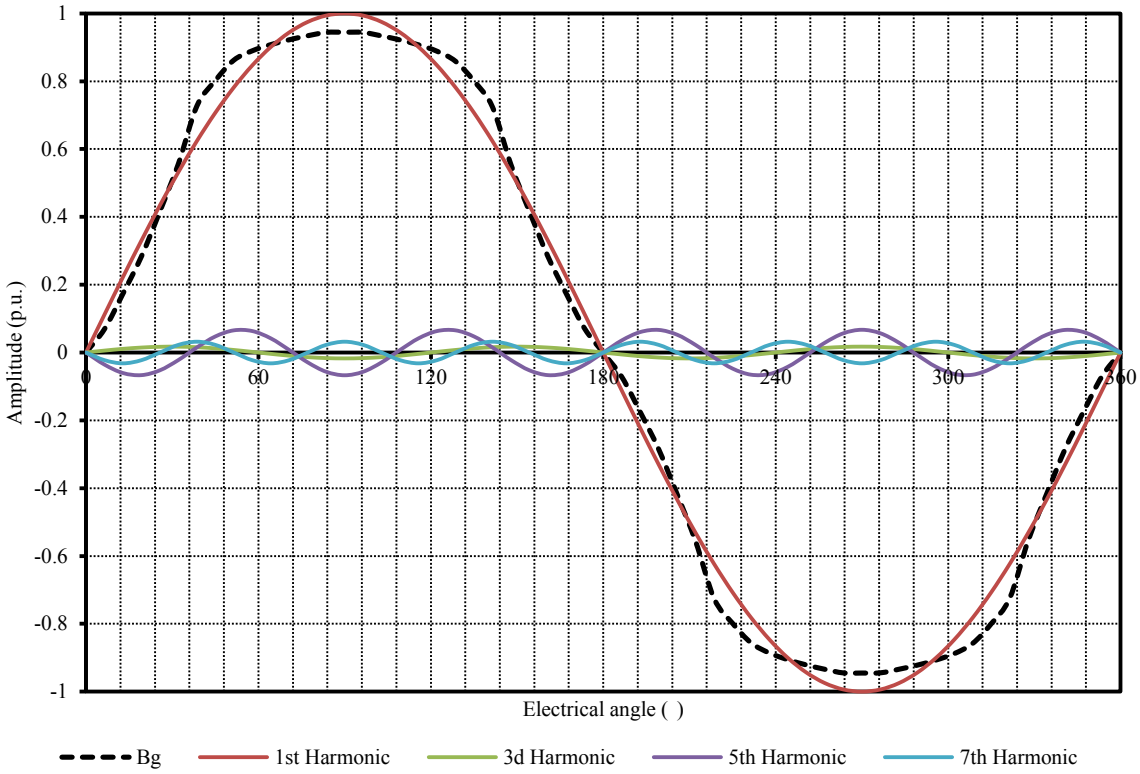

Fig. 5.6 Air gap flux density and its harmonics for one electrical cycle.

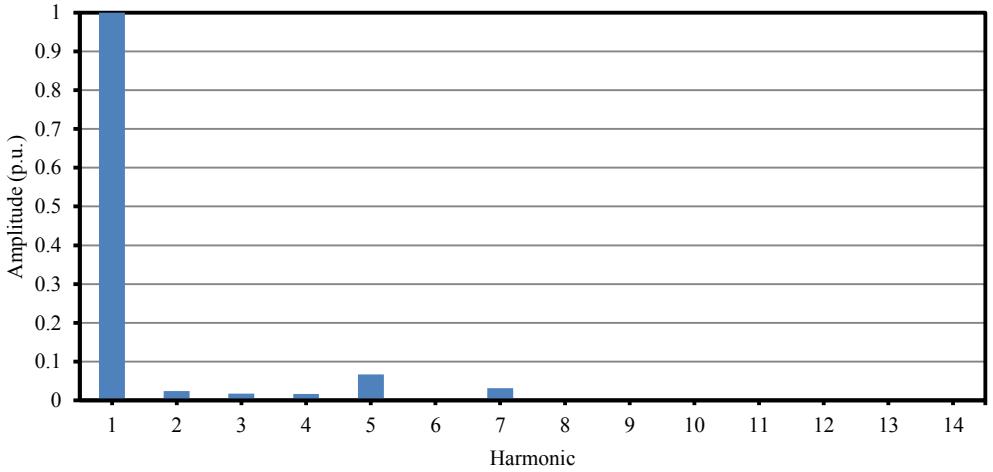

Fig. 5.7 Harmonic analysis of air gap flux density.

5.2.4 Diffusion effect in the eddy current coupling

The diffusion effect describes how the magnetic flux changes direction as it moves in a material of a particular permeability. For a radial flux machine it describes how the flux changes direction from the radial to the tangential direction, especially in the yokes. In eddy current couplings that use a ferrous loss drum the effect can be significant, particularly where the active depth of the flux return path is greater than the eddy current penetration depth [**15**] [**17**].

The diffusion effect of the magnetic field in the air gap is not included in this analytical model. In all three topologies considered in this study the conductive material of the slip rotor is a non-ferrous

material, with a second yoke on the opposite side of the conductive material as the field magnets. The magnetic flux passes through the low permeability air gap, which includes the conductive material, before it passes into the higher permeability yoke. The diffusion taking place in the yoke is limited due to the yoke being designed for a specific flux density, and has negligible effect on the induced currents in the conductive material. Additionally, the low permeability in the air gap and the constraints of (5.14) and (5.15) ensures that the diffusion taking place in the air gap itself is negligible. Therefore it is assumed in this model that the flux passes perpendicularly through the conductive material into the second yoke before significant diffusion takes places.

5.3 Modelling of the current path

5.3.1 Background of eddy current modelling in eddy current couplings

It was shown in section 5.1 that to calculate the torque it is necessary to calculate the currents in the slip rotor. In order to calculate the currents it is necessary to determine where the currents flow relative to the magnetic field. One of the main differences between modelling an eddy current coupling and a PMIM when using electrical circuit equations is that the current path is not as easily defined for the eddy current coupling. In a PMIM the current paths are defined according to the coils or squirrel cage of the rotor, but in an eddy current coupling the currents are induced in a uniform conductive material without features that directly limit the current path or its direction.

In most literature the loss drum of an eddy current coupling is a solid ferromagnetic material where the diffusion of the magnetic flux has a significant influence on the current distribution [**15**] [**18**] , and the eddy currents are often assumed to flow in a purely axial direction with the end-effects ignored [**15**] [**17**]. Due to the unspecified current path the approach followed for the analytical modelling of an eddy current coupling is often based on Maxwell's laws [**15**] [**16**] [**33**]. However, it was decided in section 1.2.3 to base the analytical model in this study on electrical circuit theory.

5.3.2 Current path model

In this section the eddy current paths for low slip frequencies are modelled based on observations from the 3D FE simulation's current density plots. Fig. 5.8 shows a current density plot of the copper component of the slip rotor, as simulated in JMAG for a slip of 3%. It is evident that the eddy currents tend to follow a circulating path, with the currents flowing in the axial direction under the magnets and in the tangential direction in the end-lengths. These current paths may be modelled as simple consecutive rectangles, as shown in Fig. 5.9. It is assumed that the eddy current coupling will be a high pole number machine with a large diameter. Therefore curvature effects are ignored, and a Cartesian coordinate system is used, as indicated in Fig. 5.9. The y-axis is in the axial direction and the x-axis is in the tangential direction.

The total length of the current path of a single modelled loop is

$$l_c = 4x + 2y \ , \tag{5.17}$$

where $2x$ represents the tangential length of the current path between two magnetic poles, with the maximum length, $2x_{max}$, being from the middle of one magnet to the middle of the next. Variable y represents the length of the current path in the axial direction, with the maximum length being the axial length of the conducting material.

Each current loop is divided into smaller elements of axial length dy, tangential length dx, and depth h_{cu}. A single element is shown in its loop in Fig. 5.10. It is clear in Fig. 5.9 that the current loops typically have longer axial than tangential lengths. Therefore the axial length of an individual loop at

$x = \Delta$ is modelled as a function of its tangential distance from the centre between two poles with an offset, that is

$$y(\Delta) = K_y + 2m_x(\Delta)dy \quad . \tag{5.18}$$

The result is that all the concentric loops together cover the entire surface of the slip-rotor. In (5.18) $y(\Delta)$ is the axial length of the loop specific to the discreet tangential distance Δ from the centre between two poles, and $m_x(\Delta)$ is the number of elements between Δ and the centre between two poles. The offset of the axial length of the current path, K_y, is a modelled physical dimension as shown in Fig. 5.9. It is used to model the axial length at which the majority of the eddy currents start turning from the axial to the tangential direction, and is considered as constant for each eddy current coupling. This offset has a significant effect on the accuracy of the analytical model, and is therefore discussed separately in chapter 6.

The tangential length of the outer current path corresponding to $\Delta = x_{max}$ is the same as the arc length of a pole pitch. Therefore one should note that:

$$2x_{max} = \tau_p$$

$$\therefore x_{max} = \frac{\tau_p}{2} \tag{5.19}$$

where τ_p is the arc length of a single pole pitch.

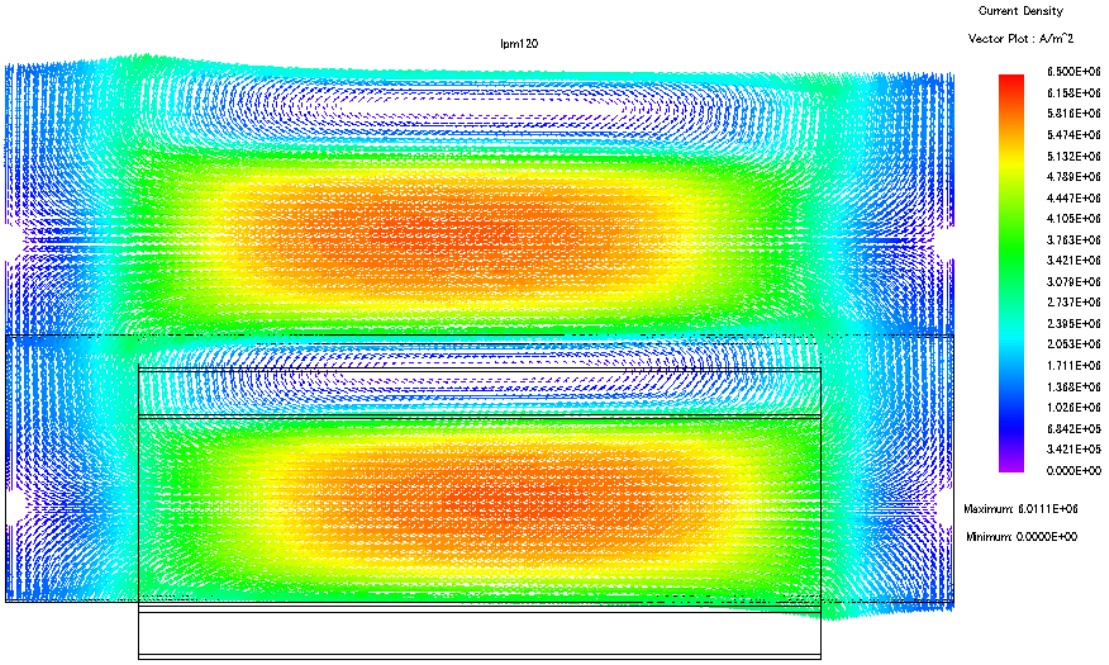

Fig. 5.8 JMAG current density plot of 3D FE eddy current coupling of the second topology, simulated at a 3% slip and viewed in the *Θ-z* plane.

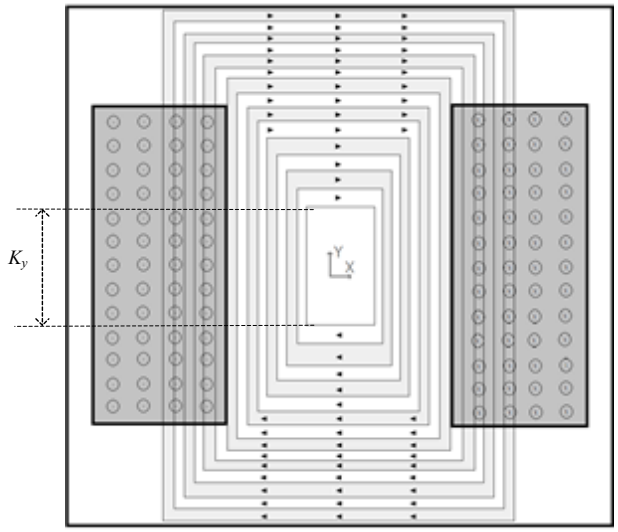

Fig. 5.9 Model of concentric current loops.

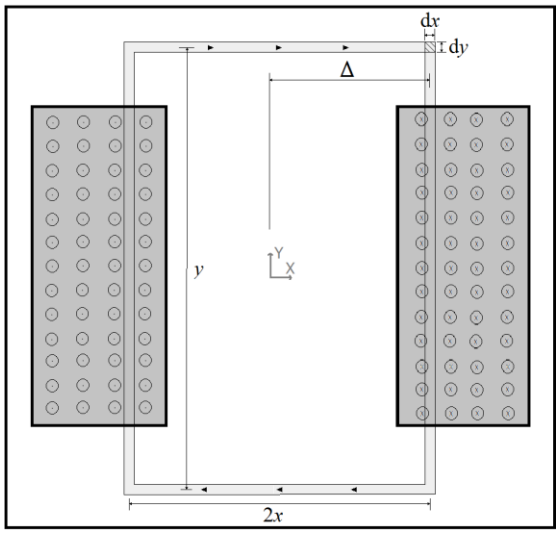

Fig. 5.10 Model of individual current loop.

5.4 Calculating the induced eddy current

5.4.1 Flux linkage calculation

In order to calculate the induced torque, the induced currents in the slip rotor have to be known. In this section the induced current of each current loop is calculated, starting at the flux linkage. The flux linkage calculation is based on work done in [**34**].

In general the flux linkage of a coil, λ, is calculated as the sum of the magnetic flux passing through consecutive turns in the coil [**31**], as in

$$\lambda = \sum_{i=1}^{N} \phi_i \ , \tag{5.20}$$

where N is the number turns and ϕ_i is the magnitude of the magnetic flux of coil-turn i. Consequently the flux linkage and the magnetic flux are equal for a single turn coil. Therefore the flux linkage of a single circular current path may be calculated by

$$\lambda = \phi = \int_A \boldsymbol{B} \cdot d\boldsymbol{A} \ , \tag{5.21}$$

from [**35**]. $\boldsymbol{B}$ is the flux density vector in the area A, and $d\boldsymbol{A}$ is a differential unit of area. It may be simplified to

$$\lambda = BA \ , \tag{5.22}$$

if the flux density has a constant magnitude B and the area A is perpendicular to the flux density vector. In the conductive material of the slip rotor the flux density varies with tangential position, which can be modelled for the fundamental harmonic as

$$B_g = B_{g1} \sin\left(\frac{px}{2r_{cu}}\right) , \tag{5.23}$$

with B_{g1} the magnitude of the fundamental harmonic of the flux density, and r_{cu} the effective radius of the conductive material as shown in Fig. 5.2. For the analytical model B_{g1} is calculated using (5.11).

The area of interest in (5.22) is the area inside a single current loop, with a tangential length of 2Δ and circumference as in (5.17) with $x = \Delta$. The area and a single area element can be specified as

$$A = 2\Delta y(\Delta) \ , \tag{5.24}$$

$$d\boldsymbol{A} = dxdy \ . \tag{5.25}$$

In Fig. 5.11 a single axial element of the eddy current loop is shown, as viewed from the axial direction. Also shown is a sinusoidal flux density wave. The axial length of the element is *dy,* into the page in Fig. 5.11. The current loop is at position x relative to the flux density wave, and has a maximum width of τ_p. For the eddy current coupling the whole of the pole pitch is considered, therefore from Fig. 5.11 :

$$0 \le \alpha \le \frac{\tau_p}{2} \ . \tag{5.26}$$

Thus α is used to indicate the width of the area for the specific current loop being considered, relative to the pitch of a single pole, τ_p. However, the width of the current loops are also defined according to Δ, therefore it can be shown that

$$\alpha = \frac{\tau_p}{2} - \Delta \ . \tag{5.27}$$

Using α, (5.23) and Fig. 5.11, the flux linkage calculation of (5.21) for an axial element of a current loop becomes [**34**]:

$$\lambda = \int_{x+\alpha}^{x+\tau_p-\alpha} B_{g1} \sin\left(\frac{px}{2r_{cu}}\right) dxdy \ . \tag{5.28}$$

Using (5.27), (5.28) can be shown to be

$$\lambda = \int_{x+\frac{\tau_p}{2}-\Delta}^{x+\frac{\tau_p}{2}+\Delta} B_{g1} \sin\left(\frac{px}{2r_{cu}}\right) dxdy \ , \tag{5.29}$$

for an axial element of a single current loop with width 2Δ.

When (5.29) is integrated in regard to x, the flux linkage for an axial element of a current loop becomes

$$\lambda = \frac{4}{p} B_{g1} r_{cu} dy \sin\left(\frac{p\Delta}{2r_{cu}}\right) \cos\left(\frac{px}{2r_{cu}}\right) \ . \tag{5.30}$$

The tangential speed u at which the conductive material of the slip rotor moves relative to the magnetic field can be calculated by dividing the distance of from one pole pair to the next by the duration of one electrical cycle $\frac{1}{f_{re}}$ of the slip rotor, as in

$$u = \frac{2\tau_p}{1/f_{re}} = \frac{4\pi r_{cu}}{p} f_{re} \ . \tag{5.31}$$

Considering that the tangential distance x is equal to the speed multiplied by time, it can be shown that

$$\frac{px}{2r_{cu}} = \frac{put}{2r_{cu}} = 2\pi f_{re} t = \omega_{re} t \ , \tag{5.32}$$

where ω_{re} is the electrical frequency in the conductive material of the slip rotor. The flux linkage equation of (5.30) for an axial element of a single turn current loop may now be simplified to:

$$\lambda = \frac{4}{p} B_{g1} \, r_{cu} \, dy \sin\left(\frac{p\Delta}{2r_{cu}}\right) \cos\left(\omega_{re} t\right) \ . \tag{5.33}$$

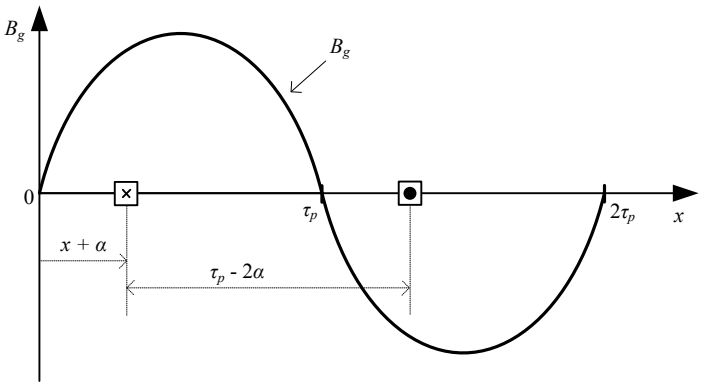

Fig. 5.11 Axial element of a current loop in a sinusoidal flux density wave.

5.4.2 Induced voltage calculation

The voltage induced in a single axial element of a current path, e_{elm}, is calculated using Faraday's law in terms of flux linkage [**31**] and the analytical calculation of the flux linkage in (5.33). Therefore

$$e_{elm} = -\frac{d\lambda}{dt} = -\frac{4}{p} B_{g1} \, \omega_{re} \, r_{cu} \, dy \sin\left(\frac{p\Delta}{2r_{cu}}\right) \sin\left(\omega_{re} t\right) \ . \tag{5.34}$$

In (5.34) $\sin(\omega_{re}t)$ describes the change in magnitude of the induced element voltage as the slip rotor moves relative to the PM rotor over time. However, since only steady-state values are calculated in the analytical model, only the relative position of the element to the magnetic field is considered. Change in the voltage over time is not used, therefore $\sin(\omega_{re}t)$ is taken as 1 in order to simplify the remaining equations. Should anything other than a static solution of the analytical model be considered, time transient effects such as $\sin(\omega_{re}t)$ has to be included in the remaining equations as well.

In a current loop l_c every element moving in the magnetic field will induce a voltage. The induced voltage will be orientated to generate a current perpendicular to the direction of movement, as shown in [**31**] with

$$e_{ind} = (\boldsymbol{v} \times \boldsymbol{B}) \cdot \boldsymbol{l} \ . \tag{5.35}$$

In (5.35) $\boldsymbol{v}$ is the velocity of the conductor relative to the magnetic field, $\boldsymbol{B}$ is the magnetic flux density vector and $\boldsymbol{l}$ is the length of the conductor in the magnetic field. It is important to note that only the component of the current path that is both perpendicular to the direction of motion and inside the magnetic field will contribute to the voltage. The current is still serial for the entire loop, which means the resistance of the entire loop has to be taken into consideration. An equivalent circuit of a single current loop is shown in Fig. 5.12.

In a current loop as described in section 5.3 the total induced voltage in the loop, e_{loop}, may be calculated using (5.34) along with certain dimensional conditions

$$e_{loop} = 2m_{ya}(\Delta)\frac{4}{p}B_{g1}\omega_{re}r_{cu}dy\sin\left(\frac{\mathrm{p}\Delta}{2r_{cu}}\right) . \tag{5.36}$$

In (5.36) e_{loop} is the sum of the induced element voltages in a specific current loop. The number of elements to be included in the sum is chosen by the function $m_{ya}(\Delta)$. $m_{ya}(\Delta)$ is the number of elements in the axial direction of one side of the current loop inside the magnetic field. The magnetic field is considered constant in the axial direction for the length of the permanent magnet, l_{pm}, and is distributed in the tangential direction according to (5.23). In (5.36) $y_a\ \Delta$ is the axial length of one side of the current path that is both perpendicular to the direction of motion and inside the magnetic field, as described by

$$m_{ya}(\Delta) = \frac{y_a(\Delta)}{dy} \ , \tag{5.37}$$

$$y_a(\Delta) = \begin{cases} K_y + 2m_x(\Delta)dy & for \quad y(\Delta) \le l_{pm} \\ l_{pm} & for \quad y(\Delta) > l_{pm} \end{cases} , \tag{5.38}$$

with the number of elements in the arc length of the current loop, $m_x(\Delta)$, calculated as:

$$m_x(\Delta) = \frac{\Delta}{dx} \ . \tag{5.39}$$

5.4.3 Calculation of the resistance of the current path

The total resistance of the current loop is the sum of the series resistances. In general the electrical resistance for any length of current carrying material is

$$R = \frac{\rho l}{A} \ , \tag{5.40}$$

with l the length of the material, A the crossectional area perpendicular to the direction of currentflow, and ρ the material resistivity. When applied to the current loop the total electrical resistance of the loop may be calculated as

$$R_{loop} = 4m_x(\Delta)R_x + 2m_y(\Delta)R_y = 4m_x(\Delta)\frac{\rho_{cu}\,dx}{h_{cu}\,dy} + 2m_y(\Delta)\frac{\rho_{cu}\,dy}{h_{cu}\,dx}, \qquad (5.41)$$

where R_{loop} is the resistance of the current loop with tangential length 2Δ, h_{cu} is the thickness of the conductive material and ρ_{cu} is the resistivity of the conductive material. It should be noted that the material resistivity is a material property that varies with temperature. The resistance of copper is shown for varying temperature in Fig. 5.13.

At low frequencies the resistance is assumed to be independent of whether or not the conductive path is in the magnetic field. Therefore while $m_x(\Delta)$ in (5.41) remains the same as in (5.39), the axial length, $y\ \Delta$, for the $m_y(\Delta)$ calculation of (5.41) becomes as originally described in (5.18):

$$y(\Delta) = K_y + 2m_x(\Delta)dy \ . \qquad (5.42)$$

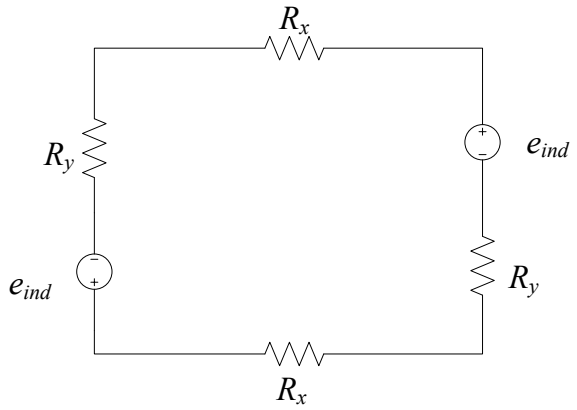

Fig. 5.12 Electrical circuit of the modelled current path.

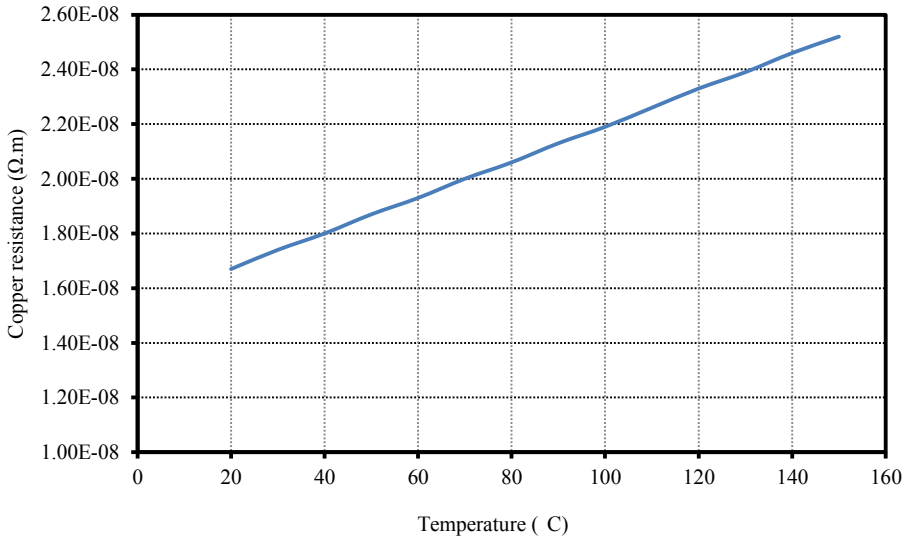

Fig. 5.13 Resistance of copper versus temperature.

5.4.4 Induced current calculation

The series current in the loop, i_{loop}, is calculated for low frequencies by applying (5.36) and (5.41) to Ohm's law:

$$i_{loop} = \frac{e_{loop}}{R_{loop}} \tag{5.43}$$

where i_{loop} is the induced current in a single current path. It is this current that will be used to calculate the induced torque.

5.5 Calculation of the torque

The basics of the approach to the torque calculation is described in section 5.1. The force tangential to the direction of rotation, due to current in the active length of conductive material in a changing magnetic field, is calculated as

$$\boldsymbol{F} = i(\boldsymbol{l} \times \boldsymbol{B}) \ . \tag{5.44}$$

In (5.44) $\boldsymbol{l}$ is the length of the conductive material perpendicular to the direction of motion of the magnetic field, and i is the current it conducts.

Applying (5.44) to the analytical model, the force generated by a particular loop is calculated as

$$F_{loop}(\Delta) = B_{g1} \sin\left(\frac{p\Delta}{2r}\right) 2y_a(\Delta)\ i_{loop} \ , \tag{5.45}$$

where $y_a\ \Delta$ is the same as in (5.38), namely the axial length of the conductive material in the magnetic field. Every concentric loop contributes to the force generated per pole, from which the torque may be calculated. Therefore the force generated per pole is:

$$F_{pp} = \sum_{n=1}^{m_x(x_{\max})} F_{loop}(\Delta_n) \ . \tag{5.46}$$

The total torque generated in the eddy-current slip coupling is calculated using (5.1):

$$T_{tot} = F_{pp} p r_{cu} \ . \tag{5.47}$$

5.6 Comparison to FE prediction

To test the analytical model, it is compared to the prototype constructed in chapter 4. In Fig. 5.14 the measured results as well as the analytical model and 3D FE results are shown. Note that the analytical model used an accurately determined value for K_y.

The comparison between the three is accurate for low slip values. There is less than 4% error between the measured and analytically predicted values throughout the measured range (up to 16% slip), and less than 1.4% error for slip values lower than 10%, or 5 Hz. At higher slip values the electrical frequency in the rotor is higher, and reactance impedance begins to have a significant effect. The analytical model is designed for low slip values, and therefore does not take reactance into consideration.

The fundamental flux density in the air gap as calculated using (5.11) is 0.61 T. Using (5.15) the flux density in the air gap is 0.572 T, which is an acceptable 1.4% lower than the 0.58 T calculated by the 3D FE simulation. Since both the flux density calculation and the remainder of the analytical model provide results with sufficiently small errors it is considered as a valuable and usable design tool.

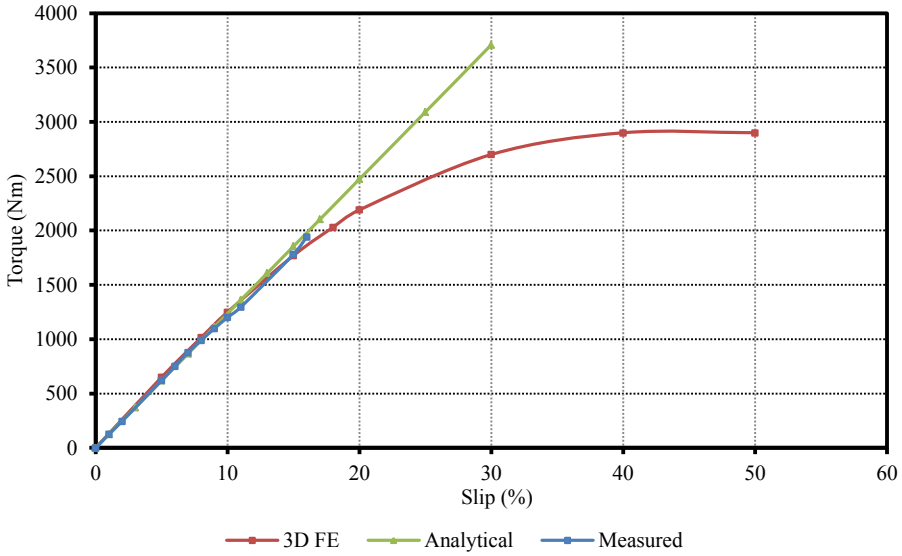

Fig. 5.14 Comparison of analytical model to 3D FE and measured results.

5.7 Effect of harmonics on the calculated torque

The analytical model uses only the fundamental flux density harmonic, and only calculates the induced eddy currents operating at the fundamental harmonic's frequency. In section 5.2.3 the harmonics of the flux density in the air gap are shown. Although the flux density harmonics have small amplitudes, with the exception of the fundamental harmonic, the small harmonics may yet have a small but significant effect on the torque. To model each harmonic's effect on the induced voltage in (5.36), both the harmonic's higher frequency and its smaller amplitude has to be taken into account. However, the analytical model used in this study does not include reactance; therefore the torque calculation will calculate too high torque values for higher frequency currents.

Furthermore, since each harmonic operates at a different frequency, each harmonic will also affect a different current path. Identifying the specific current path for each harmonic is necessary in order to include it in the analytical model, but it presents a significant challenge. The 3D FE simulations include the harmonic effects, but it is not possible to separate the effect of the different harmonics from each other in the 3D FE simulation.

In this study a compromise is made. The offset of the axial length of the current path, K_y, is approximated in chapter 6. K_y is used to model the influence of a variety of parameters that influence the length of the current path, but it also compensates for the small error made by not including the harmonic effects in the analytical approximation. In order to make the approximation of K_y as accurate as possible it uses the torque results of two 3D FE simulations, as described in section 6.3.2. The value of K_y is approximated in such a way as to make the torque calculated using (5.47) equal to the 3D FE torque. Effectively the following approximation is made by using K_y:

$$T_1 \approx T \ , \tag{5.48}$$

where T_1 is the torque calculated in the analytical model using K_y and the fundamental harmonic of the flux density, and T is the actual torque as calculated in the 3D FE simulation. It is found in section 6.3.2 that this approximation is sufficiently accurate.

5.8 Skin effect in an eddy current coupling

When an alternating current flows in a conductor the current distribution is not necessarily uniform throughout the thickness of the conductor, as assumed in this analytical approximation. The current density tends to be higher closer to the surface of the conductor. This phenomenon is called the skin effect [**35**]. The skin depth is an attenuation constant for the skin effect that is applied to a conductor, subject to the current's frequency and the conducting materials' properties. It is calculated as

$$\delta_c = \sqrt{\frac{2\rho_{cu}}{\omega_{re}\mu}} \,, \tag{5.49}$$

where δ_c is the skin depth and μ is the magnetic permeability of the material. When applied to copper, and ω_{re} of a 40 pole eddy current coupling operating at 3% slip (9.425 rad/sec), the skin depth is 57 mm. This skin depth is significantly larger than the thickness of the copper considered for the eddy current coupling. Different low slip values with different pole numbers give similarly large results for the skin depth. It is therefore justified to ignore the skin effect in the analytical approximation.

The high skin depth is largely due to the low frequency of the currents in the slip rotor. The skin effect has a significant impact in conductors operating with currents at higher frequencies [**36**], and should therefore be included if the higher frequency harmonics are considered in the calculations.

5.9 Analytical model for the third topology

Due to the differences between the flux paths of the second and third topologies, there are some differences in the analytical models of the two topologies with regard to the air gap flux density calculation. The current paths and the torque calculation remain the same, but the calculation of the flux density has to be reconsidered. Since the third topology (double PM, double air gap) as described in section 2.3 is the same as the topology used in [**28**] for the calculation of the flux density in the air gap, the resulting equation is very similar. The flux paths of the third topology are shown in Fig. 5.15, from which the new MMF equation can be given as

$$2H_c h_m = 2H_y \frac{l_y}{2} + 2H_m h_m + H_g l_g + 2H_s \frac{l_s}{2} \,, \tag{5.50}$$

where h_m is the height of a single magnet. Also note that the radial length of the air gap for the third topology is:

$$l_g = g + h_{cu} + g = 2g + h_{cu} \tag{5.51}$$

Since the same flux density is chosen in the inner and outer yokes, $H_y = H_s = 1.4$ T, and considering that

$$r_{cu} = \frac{r_s + r_y}{2} \,, \tag{5.52}$$

it can be shown that

$$H_c h_m = H_y l_{cu} + H_m h_m + H_g \frac{l_g}{2} \,. \tag{5.53}$$

The resulting new equation for the flux density in the air gap is

$$B_g = \frac{H_c h_m - H_y l_{cu}}{\left(\frac{H_c}{B_r}\right) h_m + \frac{l_g}{2\mu_0}} \tag{5.54}$$

The second change in the model is the constraint regarding the prevention of stray flux between two adjacent magnets. Since the distance the flux has to travel between two consecutive magnets in the reluctance path has been reduced by using more magnets, the new constraint becomes the same as in [**28**]:

$$l_{ipg} = \frac{2\pi r_{pm}}{p}(1-\tau_{pm}) > l_g \tag{5.55}$$

Since the distance between the PMs on the inside yoke is the smallest, r_{pm} in (5.55) is taken as the effective radius of the inner magnets.

The effect of the new constraint is that the thickness of the conductor, h_{cu}, may be almost double what it was for the single sided topology while still using the same PM thickness. This should allow for a thicker and shorter machine, which may be lighter than a thinner and longer machine.

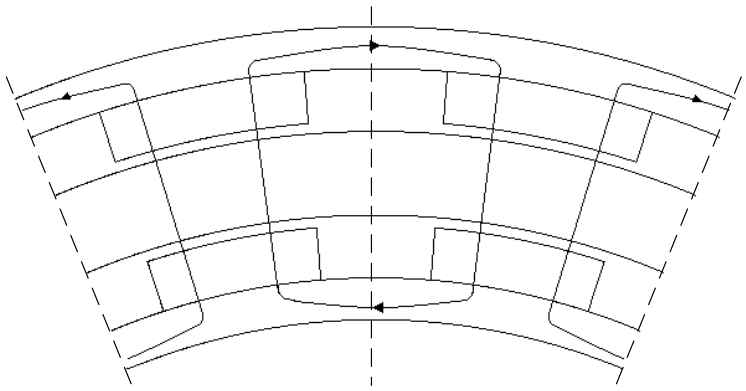

Fig. 5.15 Typical magnetic flux path diagram of the third topology.

6 Development of the approximation for K_y

K_y only has an influence on the modelling of the current path. The calculations in the remainder of the analytical approximation are accurate, but the results of those calculations are dependent on the current path, and therefore on K_y. It is of critical importance to determine K_y to within a reasonable degree of accuracy before accepting the analytical model's results as accurate. Once the approximation of an eddy current coupling's K_y value has been determined, the analytical model can be used in conjunction with optimising algorithms to optimise that machine. However, determining the exact length of K_y for an eddy current coupling is difficult.

In order to test the accuracy of the approximated K_y values it has to be compared to accurate values. The accurate values are determined by comparing the 3D FE predicted torque to the torque calculated by the analytical model of the same machine. K_y is adjusted until the analytically modelled torque is equal to the 3D FE simulated torque. In doing so the approximation of (5.48) is made, compensating for the small error in the torque calculation of the analytical model due to not including the harmonic effects.

6.1 Defining K_y

In section 5.3 the current paths are modelled based on the current density plots calculated by the FE package. As described, the axial length of the current path is a function of the distance from the centre between two poles, which ensures that each concentric current path fits exactly on the outside of the previous path. Included in the equation is a constant corresponding to where the current path turns from the axial direction to the tangential direction in the slip rotor. That constant is the axial length offset of the current path, K_y, measured in mm. Equation (5.18) that describes the axial length of the current path of a specific current loop is repeated here as

$$y(\Delta) = K_y + 2m_x(\Delta)dy \ . \tag{6.1}$$

6.2 Parameters influencing K_y

The challenge of predicting K_y is that it is different for every different current distribution. Therefore everything that has an influence on the current path has to be included in the prediction of K_y. The following shows the influences on the current, and therefore on K_y:

$$i \propto h_m, \frac{1}{h_{cu}^2}, \omega_{re}, p, l_{pm} \tag{6.2}$$

Note that the current varies from current path to current path, but that K_y is a constant value for a particular eddy current coupling operating at a specific speed with specific dimensions, as shown in (6.2). Therefore K_y does not change with the individual concentric current paths in a particular coupling, instead it has a different value for each different eddy current coupling design.

The eddy current coupling's design specifications in chapter 2 specify the slip at which it operates. Since ω_{re} in (6.2) varies only with slip and the number of poles, its influence on the approximation of K_y may be considered as constant for a particular number of poles.

Since K_y is part of the axial length of the current path it is expected to vary directly with the axial length of the eddy current coupling. In Fig. 6.1 current density plots are shown for three machines

with the same dimensions, but different axial lengths. The three plots are on scale with each other, and the differences in the axial length of the current paths between the three are clear. These significant changes in the current path are represented in the analytical model by K_y.

In Fig. 6.2 two current density plots are shown for two machines with the same dimensions, with the exception of the magnet thickness. Accordingly, one of the plots has a higher magnetic flux density, resulting in higher current densities. The effect of the higher magnitude currents on the torque is included in the analytical model calculations done in the previous chapter; however, the changes in the current paths are not. The difference in the current paths for the different flux densities is small, but still has a significant effect on the analytical calculations. These slight changes in the current paths are compensated for by using K_y. Similarly changes in the current path due to changes in copper thickness is also compensated for by K_y.

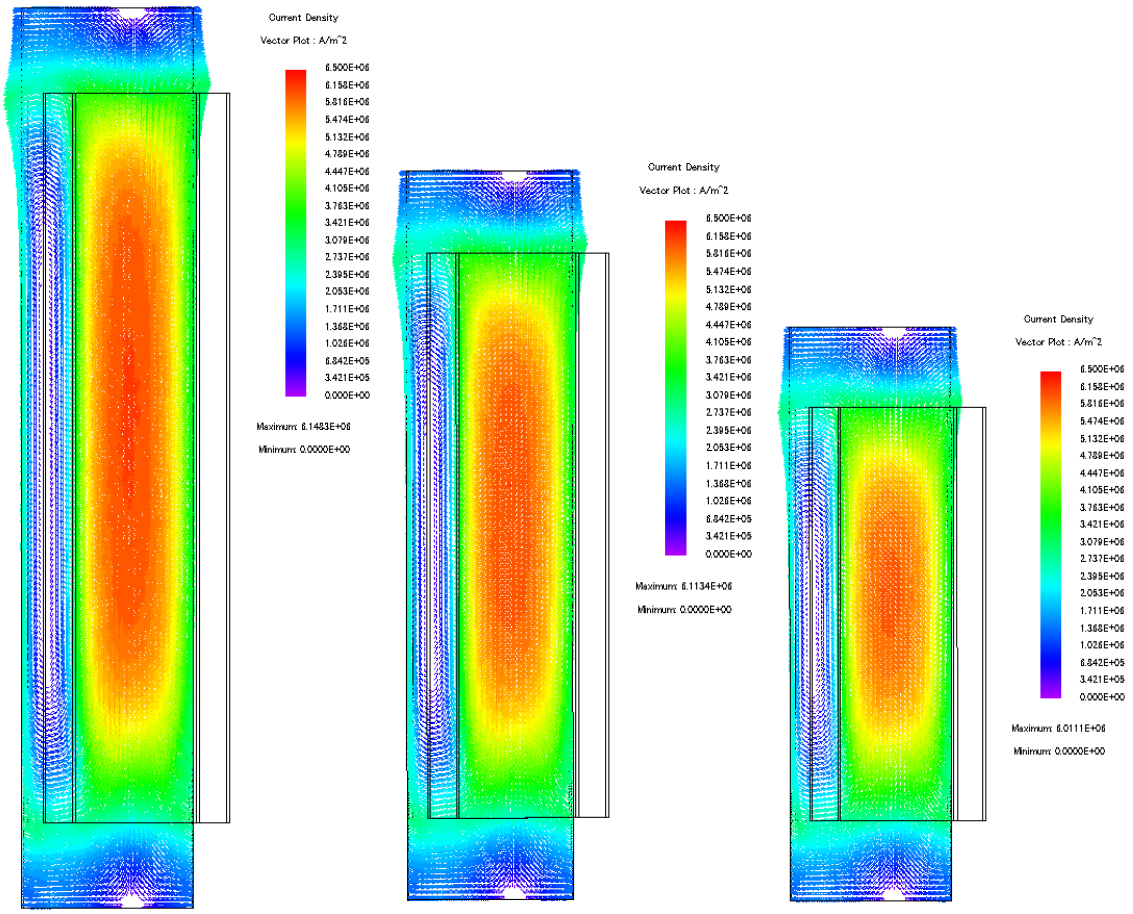

Fig. 6.1 JMAG current density plots of three identical eddy current couplings with different axial lengths, viewed in the *z*-Θ plane.

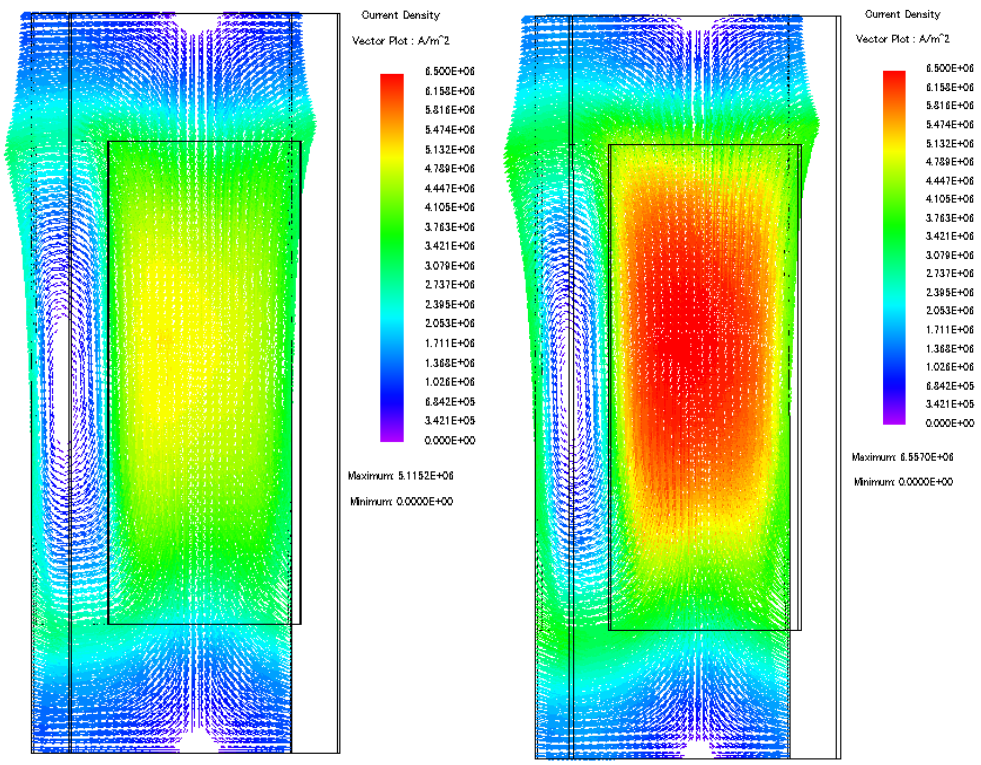

Fig. 6.2 JMAG current density plots of two identical eddy current couplings with different PM thicknesses viewed in the z-Θ plane.

6.3 The approximation of K_y

To calculate K_y an approximation is to be used, but K_y models the effect of many variables. Thus an approximation of K_y has the potential to become very complex, however studies of the preliminary optimisation lead to interesting observations regarding the eddy current coupling.

It is observed in section 7.3.1 that the thickness-related dimensions, h_{cu} and h_m, may be optimised for maximum torque independent of the length of the machine. The optimisation algorithm gives the same optimal values for the thickness-related dimensions of a particular eddy current coupling, independent of the accuracy of K_y in the analytical model. The optimal values of the thickness dimensions only change significantly with a change in the number of poles. The advantage of this observation is that K_y may now be approximated as a function of length alone, subject to specific thicknesses, leading to a different approximation for each set of thickness-related dimensions.

In the approximation the length of K_y and the tangential length of a pole pitch are to be considered as ratios of the axial length of the permanent magnets, as shown in (6.3) and (6.4):

$$\alpha_k = \frac{K_y}{l_{pm}} \tag{6.3}$$

$$\alpha_\tau = \frac{\tau_p}{l_{pm}} \tag{6.4}$$

where α_k is the ratio for the offset of the axial length of the current path and α_τ is the ratio for the pole pitch.

6.3.1 Constant approximation of α_k

When K_y is approximated as a function of the magnet length, the simplest approach is one where the offset and the magnet length have a constant ratio, i.e.:

$$\alpha_k = k \tag{6.5}$$

where k is some constant value. The result is a constant function where K_y changes linearly with the magnet length, as shown by applying (6.3) to (6.5) in

$$K_y = k l_{pm} \ . \tag{6.6}$$

An example of the constant approximation is shown in Fig. 6.3 for a 40 pole machine of the second topology. The value of k was determined accurately for a magnet length of 200 mm. Also shown in Fig. 6.3 are accurate values of α_k for the same machine with various magnet lengths. It is clear that the constant approximation gives greatly different values from the actual values for any length other than the one for which is was accurately determined. In Fig. 6.3 the greatest error in α_k is 28.5% for a magnet length of 120 mm. This leads to an error in the torque calculation of 12.7%, which is unacceptably high.

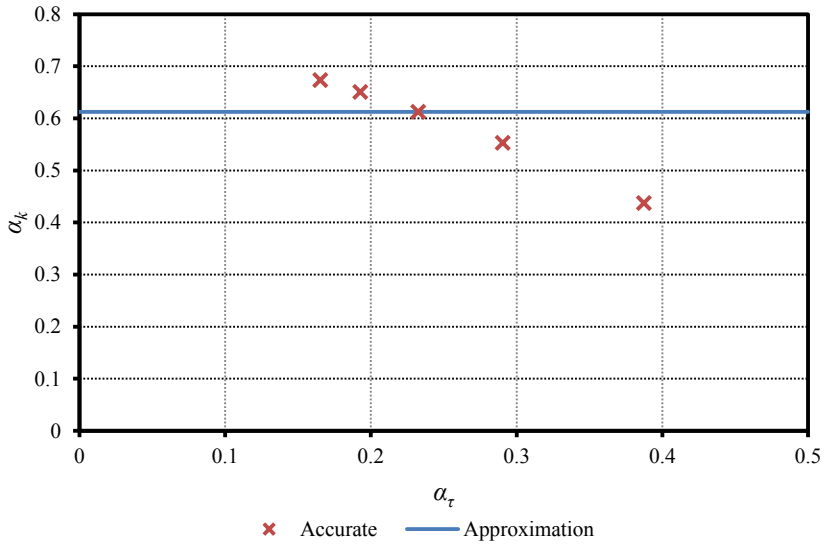

Fig. 6.3 Comparison of constant approximation and accurate values of α_k.

6.3.2 Gradient approximation for α_k

The second kind of approximation considered for α_k is a standard gradient line of the form:

$$\alpha_k = m\alpha_\tau + C \tag{6.7}$$

where m is the gradient of the line and C is the vertical axis offset. In order to determine m and C the α_k values for two different α_τ values are required for the same machine. In other words, K_y has to be known for the machine for two different lengths with all other dimensions kept constant. In Fig. 6.4 the gradient line approximation for α_k and the accurate values are shown for the same 40 pole machine simulated in section 6.3.1. The approximation is a good match to the accurate values of α_k, with the greatest error being 2.2% for α_k of the eddy current coupling with a magnet length of 280 mm. This small error leads to an acceptable 1.6% error in the torque calculation.

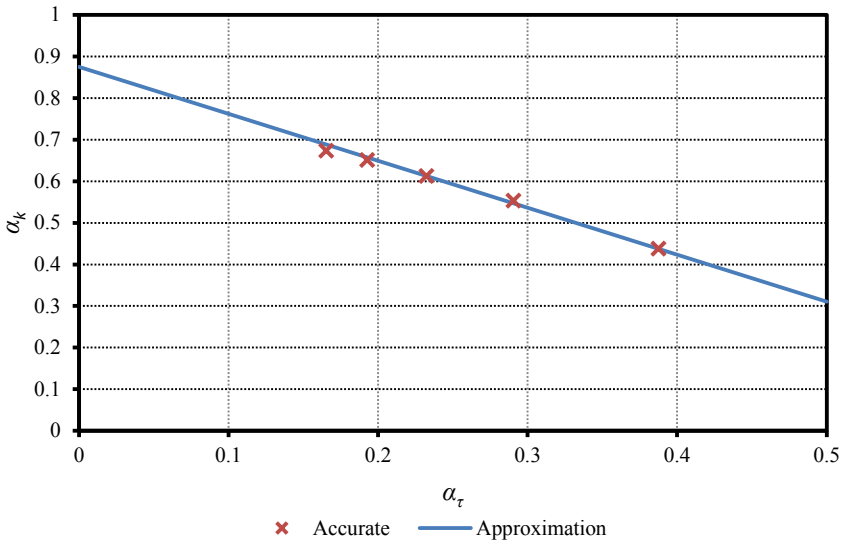

Fig. 6.4 Comparison of standard gradient line approximation and accurate values of α_k.

6.4 The process for determining the approximation of K_y

In order to use the approximation of (6.7) a specific process needs to be followed.

1. A preliminary optimisation iteration of the eddy current coupling has to be done to determine the optimal values of h_{cu} and h_m, independent of the accuracy of K_y used.
2. Two 3D FE simulations has to be done using two different magnet lengths and the determined values of h_{cu} and h_m.
3. K_y has to be determined accurately for two α_τ values. It is done by adjusting the K_y value used in the analytical model until the analytically calculated torque and the 3D FE simulated torque results agree. The accurate values of K_y are then used in (6.3) to calculate the two α_k for the corresponding α_τ values.
4. The accurate α_k and α_τ values give two coordinates on the line approximation of (6.7), which is used to determine m and C of (6.7).

With accurate values for m and C, (6.7) may be used to accurately approximate α_k, and thus K_y. By using (6.3) and (6.4) in (6.7) K_y is shown to be

$$K_y = m\tau_p + Cl_{pm} \tag{6.8}$$

in which it is clear that K_y varies only with a change in the axial length of the machine, if the pole number is kept constant.

7 Design of the optimal eddy current coupling

In order to find the dimensions for the eddy current coupling that best meets the specifications of section 1.2.2, optimisation is to be used. Both the second and third topologies are to be optimised and the optimal designs are to be compared. Additionally each topology is to be optimised for various pole numbers.

The program used for the optimisation in this study is VisualDOC 7.0. It allows the use of a variety of optimisation algorithms, and can facilitate interaction with other programs such as JMAG and MATLAB. The analytical model of chapter 5 is programmed in MATLAB R2010a and used by VisualDOC for the optimisation. Some trouble was experienced initiating communication between VisualDOC and MATLAB in the Windows 7 Professional operating system, which lead to the optimisation being done in the Ubuntu 11.04 operating system.

7.1 Optimisation methods

Optimisation algorithms can usually be classified as gradient-based or non-gradient based algorithms. Gradient-based algorithms are typically used to solve local optimisation problems, whereas non-gradient based or evolutionary algorithms are typically used for global optimisation problems [**37**].

As the name suggests gradient-based algorithms use the gradient information of the optimisation problem to find the direction in which the parameters should be changed. The problem may be constrained or unconstrained. For the eddy current coupling the problem is constrained by (5.14) and (5.15) in order to minimise stray flux. The Modified Method of Feasible Directions (MMFD) is considered to be a very robust gradient-based algorithm for constrained optimisation problems [**37**] [**38**], and therefore it is the one to be used for the eddy current coupling.

Since the eddy current coupling optimisation problem is supposed to be a local one, the same optimal values should be reached independent of the initial values used in the algorithm. It is good practise to check that different initial values give the same final result, since it is an easy way to notice if there are errors in the way the optimisation problem has been set up.

Evolutionary algorithms are better suited to solving global optimisation problems than gradient-based algorithms, but it can be used for the solving of local optimisation problems as well. The downside is that it is more computationally intensive than gradient-based algorithms and usually poor at handling constraints [**37**]. The Particle Swarm Optimisation (PSO) is an example of a non-gradient based optimising algorithm. In this study the PSO algorithm is used to confirm the results of the MMFD algorithm. Even though the PSO algorithm is not well suited to constrained problems [**39**], it is the better of the two options provided for non-gradient based algorithms in VisualDOC.

The PSO and MMFD optimisation algorithms are used with different initial values to ensure that the results are as close to the optimal as possible. Both methods typically give optimal values within 6% of each other. The dimensions calculated by the MMFD method is chosen as the optimal values due to it being better suited to the eddy current coupling's optimisation problem. Additionally, the calculated optimal values of the MMFD method are found to be slightly better than the results of the PSO method.

7.2 Optimisation approach for the eddy current coupling

The eddy current coupling is optimised for minimum mass, subject to the constraints mentioned in section 1.2.2. The constraints applicable to the eddy current coupling are given in Table 7.1. The breakdown torque is a design requirement, but is not to be included in the optimising algorithm. The outside diameter and the constraints of section 5.2.2 are dimensional constraints, and are therefore handled as side constraints [**37**] because they influence the upper and lower limits of the design parameters, as shown in (7.3). Only the minimum torque is considered as a constraint function, namely the inequality constraint $g(\boldsymbol{X})$. The objective function, $f(\boldsymbol{X})$, is the calculated active mass of the components of the eddy current coupling. Thus the design problem is defined as

$$f\left(\boldsymbol{X}\right) = w_1 M_s\left(\boldsymbol{X}\right) + w_2 M_{pm}\left(\boldsymbol{X}\right) + w_3 M_{cu}\left(\boldsymbol{X}\right) \ , \tag{7.1}$$

$$g\left(\boldsymbol{X}\right) = 1000 - T(\boldsymbol{X}) \le 0 \ , \tag{7.2}$$

$$\boldsymbol{X_L} \le \boldsymbol{X} \le \boldsymbol{X_U} \ , \tag{7.3}$$

with w_1, w_2 and w_3 weighing factors for mass of the steel (M_s), permanent magnet (M_{pm}) and conductive materials (M_{cu}) respectively. To minimise the active mass in the coupling all three weighing factors are considered equal during optimisation, as is suggested in [**28**]. In (7.2) $T(\boldsymbol{X})$ is the torque calculated by the analytical model for a specific set of dimensions. In (7.3) $\boldsymbol{X_U}$ and $\boldsymbol{X_L}$ respectively are the upper and lower limits of the design variables. $\boldsymbol{X}$ is the multidimensional vector of the different design parameters, the dimensions to be optimised. The only dimensions optimised by the algorithm are h_m, h_{cu}, and l_{pm}, since h_y, h_s and l_{cu} are determined in the analytical model using the first three dimensions. Therefore $\boldsymbol{X}$ is:

$$\boldsymbol{X} = \begin{bmatrix} h_m \\ h_{cu} \\ l_{pm} \end{bmatrix} \tag{7.4}$$

Since α_k in the analytical model has to be adjusted using two 3D FE simulations for every different pole count and topology, as explained in section 6.7, the topology and pole count are varied separately from the optimisation problem. Once the process described in section 6.7 has been followed, the analytical model may be used by the optimisation algorithm to determine $\boldsymbol{X}$ that leads to the minimum $f(\boldsymbol{X})$, subject to $g(\boldsymbol{X})$ and (7.3).

In [**28**] it is found that for air-cored radial flux permanent magnet machines the strongest magnet grade should be used, since it leads to a substantial decrease in mass without significantly increasing cost. Therefore the permanent magnets used for the design of this eddy current coupling are of the grade N48H NdFeB permanent magnet material. Copper is used as the conductive material, even though other materials such as aluminium are easy to implement in both the analytical model and the 3D FE simulations.

Parameter	Value
Rated torque (Nm)	1000
Rated slip (%)	3
Breakdown torque (pu)	≥ 2.0
Synchronous speed (rpm)	150
Outside diameter (mm)	653.5

Table 7.1 Design constraints of the eddy current coupling.

7.3 Optimisation results

7.3.1 Typical optimisation behaviour

The optimisation of a typical of 40-pole eddy current coupling of the second topology, as described in section 2.2, by the MMFD algorithm is discussed in this section. In Fig. 7.1 the changes in the Torque and mass are shown versus the optimisation iteration count, as presented in VisualDOC. In Fig. 7.2 the optimisation history plots of the dimensions in $\boldsymbol{X}$ are shown versus the optimisation iteration count.

It was observed that the optimisation algorithm gives the same optimal values for the thickness-related dimensions, independent of the accuracy of K_y in the analytical model. If the pole number is kept constant and different K_y values are used, the optimisation algorithm gives the same optimum values for h_m and h_{cu}, but with a different optimum l_{pm} value for each value of K_y.

The thickness of the conductive material, h_{cu}, has an upper limit due to the constraints of section 5.2.2. The magnet height, h_m, is not constrained, but according to (5.15) significantly increasing the magnet height decreases the upper limit for h_{cu}. During optimisation a balance is found between the two thicknesses, with the conductive material thickness large enough for a low resistance current path and small enough for limited magnetic reluctance, and the magnet thickness large enough for high air gap flux density. This means that should the machine be optimised for maximum torque rather than minimum mass, the thickness-related dimensions can be optimised independently of the length of the machine if the pole number is kept constant.

During optimisation for minimum mass the thickness-related dimensions always reach optimum values before or during the same iteration as the length does, never after the length. A single example of this can be observed in Fig. 7.2. A possible explanation is that the influence of the thickness-related dimensions on the power to weight ratio of the eddy current coupling is greater than the influence of the length, as shown in Table 7.2. In Table 7.2 typical changes in the power to weight ratio due to a change in a specific dimension are given. Note that the values are influenced by a variety of factors, and that these given changes are simply an indication of the behaviour. Since optimisation is done for minimum mass subject to a specified torque constraint, it can be argued that the thickness-related dimensions tend to reach values for maximum torque after which the length is adjusted to meet both the torque constraint for the minimum increase in mass. One of the conclusions one may make based on the values in Table 7.2 is that the eddy current coupling tends to be a thicker machine with a shorter axial length, rather than thinner and longer.

Dimension	Δh_{cu}	Δh_m	Δl_{pm}
$\frac{\Delta T}{\Delta m}$	29.47	17.65	11.58

Table 7.2 Change in power to weight ratio due to change in dimension

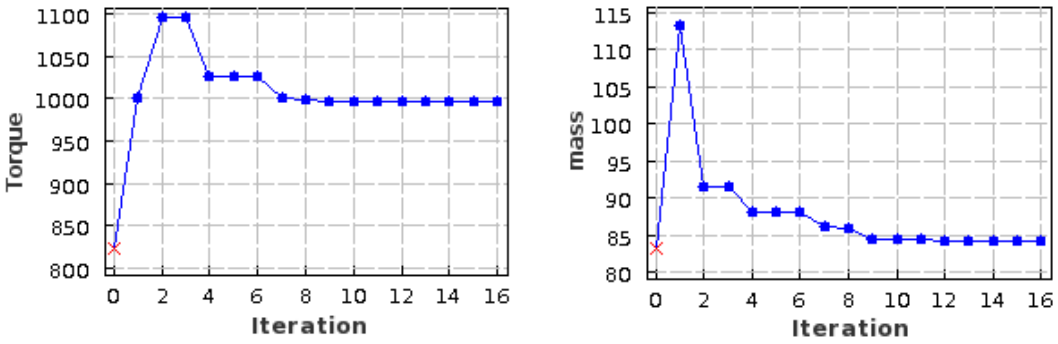

Fig. 7.1 Optimisation history plots of T in the constraint $g(\boldsymbol{X})$ and the total active mass of the objective function $f(\boldsymbol{X})$, for the optimisation of a 40-pole eddy current coupling of the second topology.

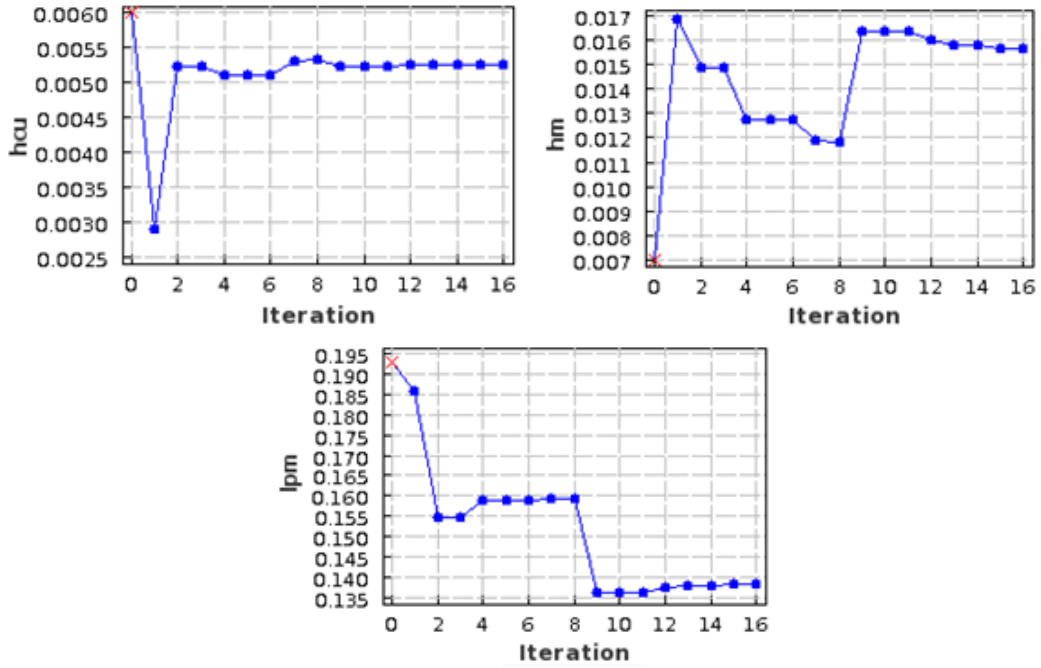

Fig. 7.2 Optimisation history plots of the dimensions in $\boldsymbol{X}$ versus iteration count for the optimisation of a 40-pole eddy current coupling of the second topology.

7.3.2 Typical optimisation time

In Fig. 7.1 and Fig. 7.2 it is shown that 16 optimisation iterations are necessary in that typical example. On average 14 solution iterations are used per optimisation iteration to find the search directions according to which $\boldsymbol{X}$ should be changed. The time required for the optimisation using an analytical model and the MMFD algorithm is 18.58 seconds. However, two 3D FE simulations are necessary before the optimisation to ensure that the analytical model provides accurate results. The duration of each FE simulation is approximately 50 minutes, effectively making the total time necessary for optimisation of the machine 100 minutes.

Consider the first approach suggested in section 1.2.2, where the optimisation algorithm uses 3D FE transient simulations rather than an analytical model. In total 269 solution iterations are used by the MMFD algorithm during the optimisation of the example used in Fig. 7.1 and Fig. 7.2. Therefore using this method for the optimisation of a single machine shall take approximately 13 450 minutes, which is slightly longer than 9 days. It is possible to shorten this time by using a rougher mesh or greater step size in the simulations, however additional iterations are then necessary to find the accurate optimum values.

In comparison to the MMFD algorithm the PSO algorithm typically uses 2800 solution iterations, and takes 127 seconds to complete. It also requires the two 3D FE simulations to ensure an accurate analytical model. Using the PSO algorithm directly with 3D FE transient simulations should be avoided if at all possible, due to the high number of iterations and the extremely long time it would take to solve such a high number of 3D FE transient simulations.

7.3.3 Optimisation of the second topology

Optimisation is done for eddy current couplings of the second topology, as described in section 2.2, for a selection of different pole numbers. In Table 7.3 the gradients and vertical axis offsets of the accurate approximations for α_k are given for the machines. Those approximations are shown in Fig. 7.3, along with the α_τ and α_k values corresponding to the optimal magnet length as calculated by the optimisation algorithm for each machine. It is interesting to note the large difference in the approximation for the lowest pole count of 20 poles in comparison to the other pole numbers. Since the number of poles is low the arc length of a pole pitch becomes large, which leads to large end-lengths. The large end-lengths along with the shorter magnet lengths lead to high α_k values.

In Table 7.4 the results of the optimisation of the selection of pole numbers are compared. The given dimensions are as calculated by the optimisation algorithm, and the given air gap flux density and torque are as determined by the 3D FE simulations done to confirm the results. From the results given in Table 7.4 it is evident that for a larger number of poles the machine is longer and thinner than for a smaller number of poles. The copper thickness is always near its upper limit, as determined by (5.14) and (5.15), and the magnet thickness is optimised for that particular copper thickness. It is interesting to note that the flux density for higher pole number optimised eddy current couplings remains fairly constant, independent of the pole number. The percentage error given in Table 7.4 is the error of the analytical model's torque compared to the 3D FE simulation's torque for the optimal machine. It is acceptably small in all cases.

In Fig. 7.4 the mass of the different components are compared for the different numbers of poles. The total PM mass increases with increasing pole counts, and similarly the copper mass decreases. The balance between copper and PM mass that leads to the lightest machine of the second topology is found to be for a 40-pole machine, which has a total active mass of 84.9 kg as given in Table 7.4. Note that while the total active mass for the 40 and 60 pole optimised eddy current couplings are very similar, the 60-pole eddy current coupling has a higher permanent magnet mass and lower copper mass. Differences such as the mass of the different materials is an important cost consideration for machine construction and large scale commercial implementation, but is not considered in this study.

p	20	30	40	60	80
m	-0.0626	-1.4625	-1.129	-0.848	-0.9412
C	1.0249	1.025	0.875	0.7588	0.7247

Table 7.3 Values used in the approximation of K_y for the second topology.

p	20	30	40	60	80
l_{pm} (mm)	105	119.7	139.6	211	337
h_y (mm)	20.5	14.58	11.36	7.85	5.96
h_{cu} (mm)	11.86	7.51	5.25	2.9	1.7
h_m (mm)	23.98	18.8	15.7	11.7	9.1
B_g (T) (3DFE)	0.82	0.845	0.86	0.87	0.86
T (Nm) (3DFE)	1013	1007	995	1005	1025
Mass (kg)	119.7	94.5	84.94	87.3	104
Error (%)	0.59	0.79	1.2	0.3	1.5

Table 7.4 Optimisation results for the second topology for a selection of pole numbers.

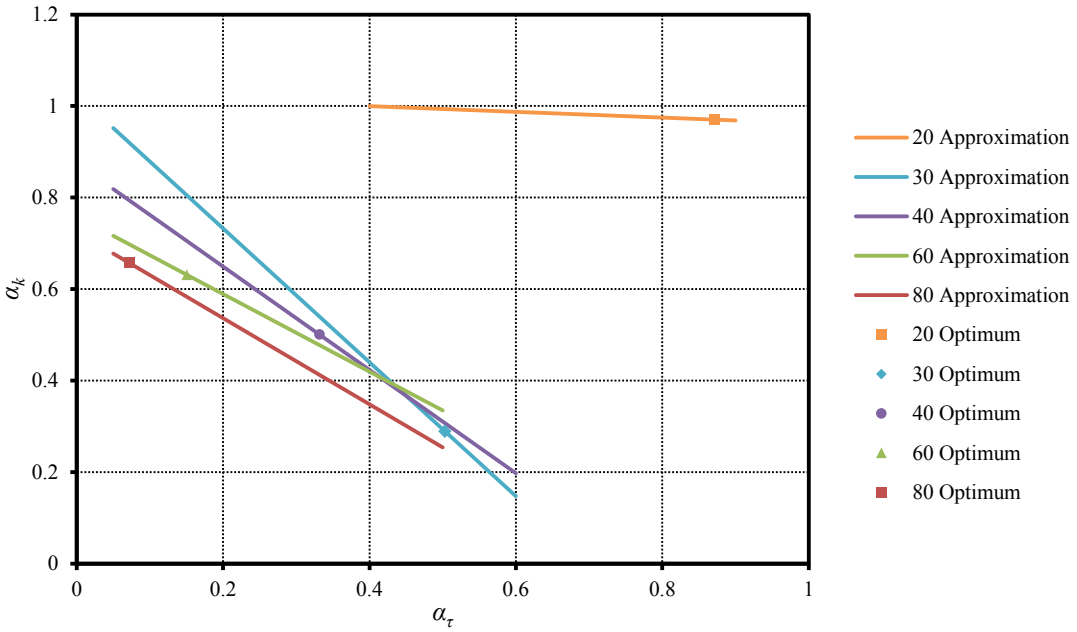

Fig. 7.3 Accurate approximations of α_k for eddy current couplings of the second topology, as determined for optimisation. Also shown is the coordinates of the optimised eddy current couplings.

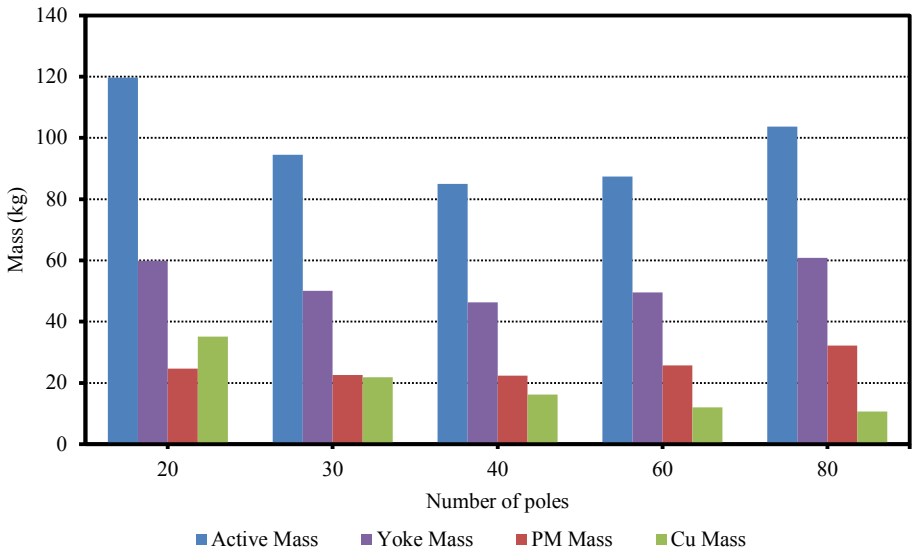

Fig. 7.4 Comparison of component and active mass for optimised eddy current couplings of the second topology.

7.3.4 Optimisation of the third topology

The same optimisation process is followed for the third topology (described in section 2.3) as for the second topology. In Table 7.5 the gradients and vertical axis offsets of the accurate approximations for α_k are given for a variety of eddy current couplings of the third topology, each with a different number of poles. Those approximations are shown in Fig. 7.5 along with the α_τ and α_k values corresponding to the optimal magnet length as calculated by the optimisation algorithm for each machine.

In Table 7.6 the results of the optimisation for the different numbers of poles are compared. Again the machine tends to become longer and thinner with increasing numbers of poles. The results of the 3D FE simulations done to confirm the accuracy of the analytical model is also included in Table 7.6. The errors are acceptably low, though notably higher than for the second topology. It is important to note that the error between the analytical model and the 3D FE model causes the optimised machine to have torque lower than the design specifications required. A possible solution is to do the final adjustments in the dimensions manually, for example by slightly increasing the length and then testing the result using 3D FE simulations. A potentially faster solution is to increase the torque requirement used in the optimisation to higher than the design specification.

In Fig. 7.6 the mass of the different components are compared for the different numbers of poles. The total PM mass remains fairly constant, though it increases for large numbers of poles. The copper mass decreases significantly with increasing numbers of poles. The lightest machine of the third topology is found to be a 60-pole machine, which has a total active mass of 65.3 kg.

p	**30**	**40**	**60**	**80**
m	-0.0832	-1.368	-0.8741	-0.5542
C	1.1499	0.9331	0.7997	0.7502

Table 7.5 Values used in the approximation of K_y for the third topology.

p	30	40	60	80
l_{pm} (mm)	80.9	87.5	123.8	190.4
h_y (mm)	14.6	11.3	7.6	5.69
h_{cu} (mm)	12.46	9.23	5.26	3.13
h_m (mm)	16.42	14.3	10.03	7.63
B_g (T) (3DFE)	0.82	0.83	0.83	0.82
T (Nm) (3DFE)	1021	985	985	990
Mass (kg)	83.75	71	65.32	72.6
Error (%)	1.4	2.2	2.3	1.7

Table 7.6 Comparison of optimisation results for the third topology.

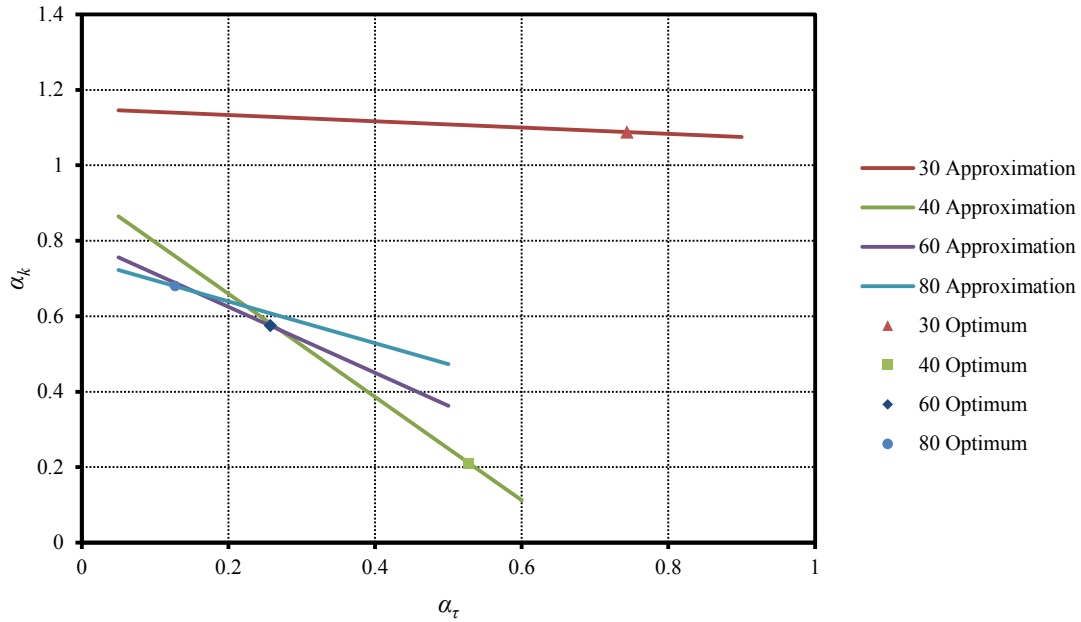

Fig. 7.5 Accurate approximations of α_k for eddy current couplings of the third topology, as determined for optimisation. Also shown is the coordinates of the optimised eddy current couplings.

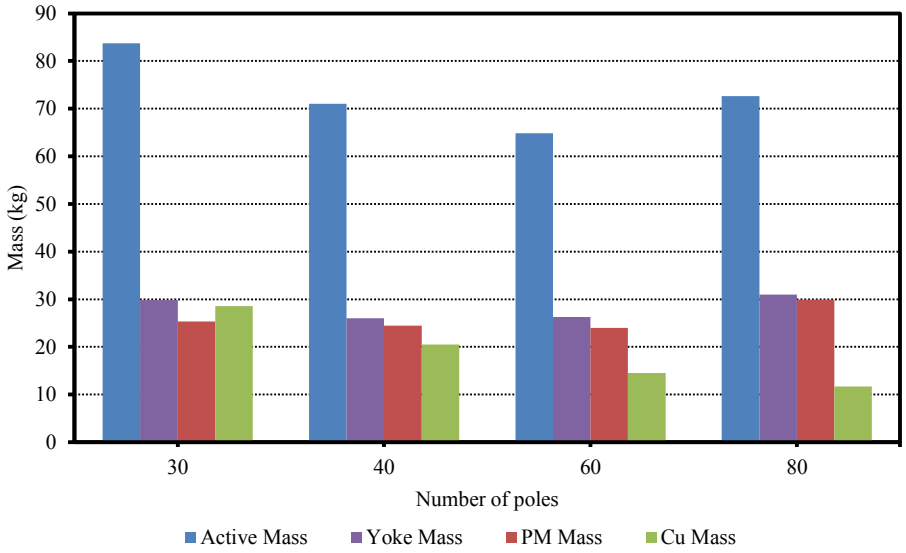

Fig. 7.6 Comparison of component and active mass for optimised eddy current couplings of the third topology.

7.4 Comparison of the topologies' optimisation results

In section 7.3.3 the optimum design for the second topology (single PM, single air gap) is shown to be a 40-pole machine. Similarly the optimum design for the third topology (double PM, double air gap) is a 60-pole machine as shown in section 7.3.4. Of the two topologies the double sided PM rotor options tends to be of significantly lower mass. Due to the permanent magnets on both sides of the copper, the constraints limiting the copper thickness allows a greater copper thickness for the same number of poles. Therefore an eddy current coupling of the third topology can be shorter and thicker than for the second topology, which leads to a coupling of lower mass.

The PM mass used in the eddy current couplings is very high, though that is expected for air-cored machines such as the eddy current coupling. It is interesting to note that the two topologies use approximately the same mass of permanent magnet material, but the second topology uses significantly more yoke mass. This is due to the second topology using a significantly larger magnet height on one yoke, which necessarily increases the yoke height. Additionally, optimised eddy current couplings of both topologies have similar flux densities in the air gap, particularly for higher pole counts, though the flux density is lower for the third topology than for the second topology.

The analytical model leads to slight errors when compared to 3D FE simulated values of the optimised machine. The error is lower for the second topology than for the third, but is still acceptable for both. It should be considered to adjust the torque constraint used in the optimisation to higher than the design specification in order to ensure that the torque design specification is met.

The third topologies' best optimised eddy current coupling is a remarkable 30% lighter than the best optimised eddy current coupling of the second topology. Considering the difference in optimised results between the second and third topologies' best machines it is clear that the third topology is the better choice from a mass perspective.

7.5 Comparison of the analytical and 3D FE results of the optimised topology

To investigate the optimised 60 pole eddy current coupling of the third topology, 3D FE transient simulations are done for higher slip values. The results are shown in Fig. 7.7 along with the analytical model's calculated results for the same slip values. Again there is a good correlation between the 3D FE and analytically calculated results for low slip values. For slip values lower than 11%, or

fundamental current frequencies lower than 8.25 Hz, the error of the analytical calculation is less than 4.5%, with an error of 2.3% at the rated slip. The breakdown torque of the eddy current coupling is very high at 8215 Nm, reached at a slip of 40%. It is significantly better than the 2.0 per unit minimum specification in Table 7.1. The torque versus time behaviour of the optimised eddy current coupling is shown in Fig. 7.8 at rated slip. The first 0.04 seconds is the time required for the transient solution to reach steady-state values. As expected the eddy current coupling generates no torque ripple.

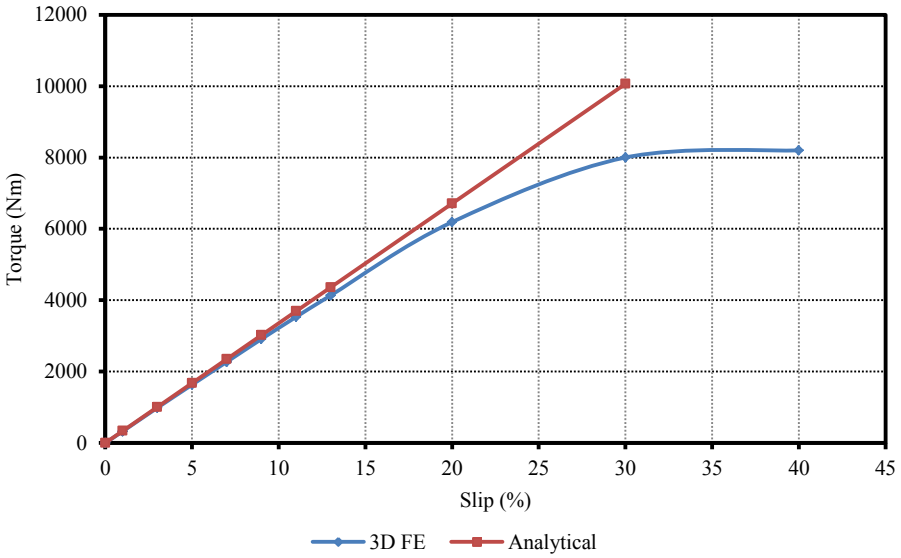

Fig. 7.7 Analytical and 3D FE torque versus slip behaviour for the optimised eddy current coupling of the third topology.

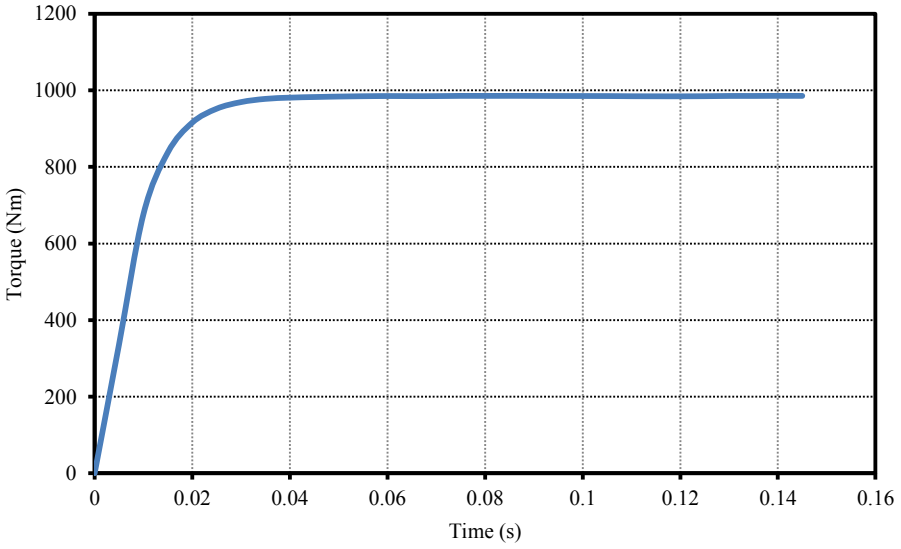

Fig. 7.8 3D FE transient simulated torque versus time behaviour of the optimised 60 pole eddy current coupling of the third topology, at 3% slip.

8 Conclusions

The focus of this study is on the modelling and design of an eddy current coupling for implementation in a SS-PMG. The eddy current coupling has the advantage of completely removing cogging and load torque ripple, which are known problems in the SS-PMG. The drawback of the eddy current coupling is the complex nature of its modelling.

Proposed eddy current coupling
Due to the high torque requirements of the SS-PMG and the difficult modelling of conventional eddy current couplings it is proposed to use a featureless non-ferromagnetic conductive material as the eddy current slip rotor. Three eddy current coupling topologies are suggested, investigated and compared. Two of these topologies have the important advantage of no attraction forces between the slip rotor and the PM rotor.

Finite element modelling of the eddy current coupling
A small prototype eddy current coupling is used for an initial investigation into the FE modelling of eddy current couplings. It is shown that transient 2D FE simulations are inaccurate in the performance prediction of the proposed eddy current couplings. This is mainly due to eddy currents not flowing in only one direction, but following circular-type patterns. Transient 3D FE simulations, however, show excellent correlation with measured results. FE simulation results confirm that the eddy current coupling has no cogging or load torque ripple.

Design and construction of a prototype slip rotor
A prototype slip rotor is designed to operate with an existing PM rotor, using 3D FE transient simulations. The first and second proposed eddy current coupling topologies are optimally designed and compared in terms of torque and efficiency per amount of magnet material. It is shown that using a reduced air gap by combining the inner rotor yoke and the copper slip rotor to create a mixed rotor as loss drum, produces 35 % more torque using the same amount of PM material. This topology, however, has the disadvantage of large attraction forces between the slip rotor and PM rotor.

Significant challenges were experienced during construction of the designed slip rotor prototype. The accurate manufacturing of a copper ring is very difficult, even though the slip rotor topology is a simple concept. Alternative methods for accurate manufacturing of large eddy current coupling slip rotors have to be investigated to make economical production of the machine more practical. Using alternative materials for the conductive ring should also be considered, as it can lead to easier manufacturing.

Close correlation between the measured results of the constructed eddy current coupling and 3D FE simulation results justifies the use of 3D FE simulation as an accurate representation of reality. Additionally, it is found that the end-lengths of the conductive material of the slip rotor may be designed as 50 % of a pole pitch.

Analytical model
An analytical model for the calculation of torque, based on dimensions and material properties, is developed. However, accurate knowledge of the eddy current paths is necessary, specifically the axial length offset K_y. It is shown that K_y may be approximated as a function of length alone, subject to specific thicknesses. A process to determine an accurate gradient line approximation of K_y by using two 3D FE transient simulations is presented.

It is shown that only the fundamental harmonic of the flux density in the air gap has to be used in the analytical model, due to the low frequency operation of the eddy current coupling. In using the approximation for K_y, there is compensated for the slight error made by not including the effect of the higher harmonic eddy currents in the analytical model. The skin effect may be ignored for the fundamental harmonic of the induced eddy currents.

Comparison to 3D FE and measured results confirm that the analytical model accurately calculates the performance of an eddy current coupling for low slip values, when using an accurate approximation for K_y. Therefore it is used for the optimisation of two of the eddy current coupling topologies.

Optimally designed eddy current coupling
Optimisation is done for a selection of pole numbers for the second and third proposed eddy current coupling topologies, using copper as the conductive material in the slip rotor. The analytical model allows for rapid optimisation with high accuracy, with the accuracy confirmed by 3D FE simulations.

It was found that the radial dimensions can be optimised independent of the length of the machine, but that the optimum values are dependent on the number of poles of the eddy current coupling. The optimal eddy current coupling tends to be as large in the radial direction as allowed for by the constraints. Thus the length is increased and the radial thickness is decreased if the pole number is increased.

The optimal eddy current coupling, as designed for the SS-PMG, is a 60-pole machine of the third topology. It is shown that the optimal designs of the third topology tend to be significantly lighter than the optimal designs of the second topology, for the same pole number. The lowest mass eddy current coupling of the third topology has 30% less active mass than the lowest mass eddy current coupling of the second topology.

It is shown that for the best optimally designed eddy current coupling the analytical model is reasonably accurate up to 11% slip, with good accuracy at lower slip values. The eddy current coupling satisfies the design specifications, and has remarkably high breakdown torque.

Comparison to other S-PMGs
The eddy current coupling was designed to perform the function of the S-PMG in a SS-PMG, according to the same specifications used in [**27**] for the evaluation of S-PMGs. When the optimally designed 60-pole eddy current coupling of the third topology is compared to the S-PMGs evaluated in [**27**], the eddy current coupling performs well regarding torque, but poorly regarding mass. Since the eddy current coupling has no torque ripple and the breakdown torque is high, it performs better for all the torque evaluations than the existing technologies. However, the mass of the eddy current coupling is significantly higher than that of the 3-phase overlap wound and two brushless DC machines. Those machines have the drawback of difficult construction, which is something that still requires further investigation for the eddy current coupling.

Another consideration is cost. The S-PMGs in [**27**] were optimised with different constraints on the amount of PM material with cost in mind, whereas the PM material in the optimisation of the eddy current coupling was done purely for minimum active mass. Thus the PM material used in the eddy current coupling is significantly more than that of the S-PMGs in [**27**], however high PM mass is expected for air-cored machines such as the eddy current coupling. Surprisingly the use of a solid copper ring in the slip rotor did not cause the eddy current coupling to have significantly higher copper mass than that of the existing S-PMG technologies.

Recommendations for further investigation

It would be interesting to investigate the change in accuracy of the model of including the higher harmonics of the flux density and eddy currents. Skin depth and the reactance impedance of the conductor will have to be included in the calculations.

Further investigation has to be done to determine accurate manufacturing methods for the eddy current coupling. Particular attention should be given to the construction of the third topology, and the mechanical specifications for a slip rotor of a purely conductive material. Different configurations for the conductive material should also be considered, such as solid single turn copper coils instead of a copper ring. Alternative conductive materials should also be investigated, for both construction and design purposes. It is a simple matter to adjust the properties in the analytical model for different materials.

The cost considerations of an eddy current coupling in a WTG have not been considered in this study, and it is an important consideration for commercial WTGs. It is stated in [**27**] that the selection of the S-PMG configuration will mostly be governed by cost, which is largely influenced by the material prices and construction method. Therefore the economical design and manufacture of eddy current couplings for SS-PMGs is a topic that requires further investigation.

Closing remarks

The major contribution of this study is the accurate slip frequency model for large diameter, high torque eddy current couplings. It is shown that the eddy current coupling proposed in this study is a possible solution to the problem of cogging and load torque ripple in S-PMGs, however torque quality is not the only consideration in S-PMG selection. Due to the high PM mass required, the eddy current coupling is very expensive. Thus existing S-PMG technologies are more likely to be implemented in a slip-synchronous permanent magnet wind generator.

9 Bibliography

[1] H. Li and Z. Chen, "Overview of different wind generator systems and their comparisons," *Renewable Power Generation, IET*, vol. 2, no. 2, pp. 123-138, June 2008.

[2] B. Hagenkort, T. Hartkopf, A. Binder, and S. Jockel, "Modelling a Direct Drive Permanent Magnet Induction Machine," in *International Conference on Electrical Machines (ICEM)*, Espoo (Finland), 2000, pp. 1495-1499.

[3] J. H. J. Potgieter, A. N. Lombard, R-J Wang, and M. J. Kamper, "Evaluation of permanent magnet excited induction generator for renewable energy applications," in *18th Southern African Universities Power Engineering Conference*, Stellenbosch (South Africa), 2009, pp. 299-304.

[4] E Tröster, M Sperling, and Th Hartkopf, "Finite Element Analysis of a Permanent Magnet Induction Machine," in *International Symposium on Power Electronics, Electrical Drives, Automation and Motion*, Taormina (Italy), 2006, pp. S39 17-22.

[5] T. Tsuda, T Fukami, Y. Kanamaru, and T. Miyamoto, "Effects of the Built-in Permanent-Magnet Rotor on the Equivalent Circuit Parameters of a Permanent-Magnet Induction Generator," *IEEE Transactions on Energy Conversion*, vol. 22, no. 3, pp. 798-799, 2007.

[6] G. Gail et al., "Static and Dynamic Measurements of a Permanent Magnet Induction Generator: Test Results of a New Wind Generator Concept," in *Recent Developments of Electrical Drives*. Darmstadt, Netherlands: Springer, 2006, ch. III, pp. 375-384.

[7] P. J. Tavnet, G. J. W. Van Bussel, and F. Spinato, "Machine converter and reliabilities in wind turbines," in *The 3rd IET International Conference on Power Electronics, Machines and Drives (PEMD)*, Dublin (Ireland), 2006, pp. 127-130.

[8] J. H. J. Potgieter and M. J. Kamper, "Design of a New Concept Direct Grid-Connected Slip-Synchronous Permanent Magnet Wind Generator," *IEEE Transactions on Industry Applications*, vol. 48, no. 3, pp. 913-922, May/June 2012.

[9] J. H. J. Potgieter and M. J. Kamper, "Design of new concept permanent magnet induction wind generator," in *IEEE Energy Conversion Congress and Exposition (ECCE)*, Atlanta (USA), 2010, pp. 2403-2408.

[10] P. Bouwer, J. H. J. Potgieter, and M. J. Kamper, "Modelling and Dynamic Performance of a Direct-Drive Direct-Grid Slip Permanent Magnet Wind Generator," in *IEEE International Electric Machines and Drives Conference (IEMDC)*, Niagara Falls (Canada), 2011, pp. 137-142.

[11] U. Hoffmann, P. Bouwer, and M. J. Kamper, "Direct Grid Connection of a Slip-Permanent Magnet Wind Turbine Generator," in *IEEE Energy Conversion Congress and Exposition (ECCE)*, Phoenix (USA), 2011, pp. 2373-2380.

[12] J. H. J. Potgieter and M. J. Kamper, "Cogging Torque Sensitivity in Design Optimisation of Low Cost Non-overlap Winding PM Wind Generator," in *XIX International Conference on Electrical Machines (ICEM)*, Rome (Italy), 2010, pp. 1-6.

[13] A. Wallace, A. Von Jouanne, R. Jeffryes, E. Matheson, and X. Zhou, "Comparison testing of an adjustable-speed permanent-magnet eddy-current coupling," in *Pulp and Paper Industry Technical Conference*, Atlanta (USA), 2000, pp. 73-78.

[14] AIEE Committee Report, "Bibliography of Electric Couplings," Power Apparatus and Systems, Part III. Transactions of the American Institute of Electrical Engineers doi: 10.1109/AIEEPAS.1953.4498623, 1953.

[15] E. J. Davies, "An Experimental and Theoretical Study of Eddy-Current Couplings and Brakes," *IEEE Transactions on Power Apparatus and Systems*, vol. 82, no. 67, pp. 401-419, August 1963.

[16] S.E. Gay and M. Ehsani, "Analysis and Experimental Testing of a Permanent Magnet Eddy-Current Brake," in *Vehicle Power and Propulsion, IEEE Conference*, Chicago (USA), 2005, pp. 756-765.

[17] A. B. Dietrich, I. E. Chabu, and J. R. Cardoso, "Eddy-Current Brake Analysis Using Analytic and FEM calculations - Part I: Theory," in *IEEE International Electric Machines and Drives Conference (IEMDC)*, Boston (USA), 2001, pp. 454-457.

[18] M.G. Malti and R. Ramakumar, "Three-Dimensional Theory of the Eddy-Current Coupling," *IEEE Transactions on Power Apparatus and Systems*, vol. 82, no. 68, pp. 793-800, October 1963.

[19] D. Gonen and S. Stricker, "Analysis of an Eddy-Current Brake," *IEEE Transactions on Power Apparatus and Systems*, vol. 84, no. 5, pp. 357-361, May 1965.

[20] S. Huang, M. Aydin, and T. A. Lipo, "Torque Quality Assessment and Sizing Optimization for Surface Mounted Permanent Magnet Machines," in *Thirty-Sixth Industry Applications Conference*, Illinois (USA), 2001, pp. 1163-11610.

[21] N. Bianchi and S. Bolognani, "Design techniques for reducing the cogging torque in surface-mounted PM motors," *IEEE Transacions on Industry Applications*, vol. 38, no. 5, pp. 1259-1265, Sep/Oct 2002.

[22] P. Salminen, J. Pyrhönen, F. Libert, and J. Soulard, "Torque ripple of permanent magnet machines with concentrated windings," in *XII International Symposium on Electromagnetic Fields Mechatronics, Electrical Electronic engineering (ISEF)*, Baiona (Spain), 2005.

[23] Z. Q. Zhu and D. Howe, "Influence of design parameters on cogging torque in permanent magnet machines," *IEEE Transactions on Energy Conversion*, vol. 15, no. 4, pp. 407-412, Dec 2000.

[24] J. Beerten, J. Verveckken, and J. Drieson, "Predictive direct torque control for flux and torque ripple reduction," *IEEE Transactions on Industrial Electronics*, vol. 57, no. 1, pp. 404-412, Jan 2010.

[25] Z. Jabbour, A. Riwan, S. Moreau, J. Van Rhijn, and G. Champenois, "Identification and compensation of torque ripples of a PMSM in a haptic context," in *36th Annual Conference of the IEEE Industrial Electronics Society*, Phoenix (USA), 2010, pp. 1665-1670.

[26] W. Qian, S. K. Panda, and J. X. Xu, "Torque ripple minimisation in PM synchronous motors using iterative learning control," *IEEE Transactions on Power Electronics*, vol. 19, no. 2, pp. 272-279, March 2004.

[27] J. H. J. Potgieter and M. J. Kamper, "Optimum design and technology evaluation of slip permanent magnet generators for wind energy applications," in *IEEE Energy Conversion Conference and Exposition (ECCE)*, Raleigh (USA), 2012, pp. 2342-2349.

[28] J. A. Stegmann and M. J. Kamper, "Design Aspects of Double-Sided Rotor Radial Flux Air-Cored Permanent-Magnet Wind Generator," *IEEE Transactions on Industry Applications*, vol. 47, no. 2, pp. 767-778, March/April 2011.

[29] R. L. Stoll, *The Analysis of Eddy Currents*, P. Hammond and D. Walsh, Eds. London: Clarendon Press, 1974.

[30] T. Nicol, "Study of an Air-Cored Permanent Magnet Induction Wind Generator for the SANAE IV Research Base," Stellenbosch University, Stellenbosch (South Africa), Skripsie Report 2010.

[31] S. J. Chapman, *Electric Machinery Fundamentals*, 4th ed. Australia: McGraw-Hill, 2005.

[32] R-J Wang, M. J. Kamper, K. Van der Westhuizen, and J. Gieras, "Optimal Design of a Coreless Stator Axial Flux Permanent-Magnet Generator," *IEEE Transactions on Magnetics*, vol. 41, no. 1, pp. 55-64, Jan 2005.

[33] X. Wang and D. Wang, "Calculation of Eddy Current Loss and Thermal Analysis for Adjustable Permanent Magnet Coupler," in *International conference on Electronic and Mechanical Engineering and Information Technology (EMEIT)*, Harbin (China), 2011, pp. 4405-4408.

[34] M. J. Kamper, R-J Wang, and F. G. Rossouw, "Analysis and Performance of Axial Flux Permanent-Magnet Machine With Air-Cored Nonoverlapping Concentrated Stator Windings," *IEEE Transactions on Industry Applications*, vol. 44, no. 5, pp. 1495-1505, September/October 2008.

[35] B. Guru and H. Hiziroglu, *Electromagnetic Field Theory Fundamentals*, 2nd ed. Kettering University: Cambridge University Press, 2005.

[36] R. L. Soll, *The Analysis of Eddy Currents*, P. Hammond and D. Walsh, Eds. London: Clarendon Press, 1974.

[37] G. Venter, "Review of Optimization Techniques," in *Encyclopedia of Aerospace Engineering*, R. Blockley and W. Shyy, Eds., 2010, ch. 428 (Vol 8).

[38] Vanderplaats Research & Development, Inc., *VisualDOC Theory Manual Version 7.0*. Colorado Springs, USA, 2011.

[39] Vanderplaats Research & Development, Inc., *VisualDOC User's Manual Version 7.0*. Colorado Springs, USA, 2011.